Low Energy Electron Diffraction (LEED) and Sum Frequency Generation (SFG) Vibrational Spectroscopy Studies of Solid-Vacuum, Solid-Air and Solid-Liquid Interfaces

by

Saskia Hoffer

B.S. (Colorado School of Mines) 1995

A dissertation submitted in partial satisfaction of the
requirements for the degree of

Doctor of Philosophy

in

Chemistry

in the

GRADUATE DIVISION

of the

UNIVERSITY of CALIFORNIA at BERKELEY

Committee in Charge:

Professor Gabor A. Somorjai, Chair
Professor Ron Cohen
Professor Roya Maboudian

Fall 2002

The dissertation of Saskia Hoffer is approved:

Chair Date

Date

Date

University of California, Berkeley

Fall 2002

The dissertation of Craig Tewell is approved:

Chair Date

Date

Date

University of California, Berkeley

Fall 2002

Acknowledgements

As the years have gone by in Berkeley, I have started this page countless times in my head. While the influence of individuals has fluctuated with time, I am still left with the same list in my head - family, friends, and co-workers.

It is most appropriate to thank my advisor, Prof. Gabor Somorjai who over the last five years has taken me from a shaky graduate student to a confident experimentalist and researcher. While I cannot explain the debt of gratitude I feel, I hope that in my future I can repay him with my accomplishments - accomplishments that prior to his influence would never have been possible.

As is the side effect of being in a dynamic research environment many of my colleges have come and gone in my tenure at UC Berkeley; however their knowledge, helpfulness, and their friendship will never be forgotten. Firstly I have to thank Joel Roberts for pulling me through my first years here, his mentoring, advising, inquisitive, sarcastic, sleepy ways taught me all I know about UHV and LEED and even parts of life – as a consequence he will always be dear friend.

I have worked with a lot of different graduate students and postdoctoral fellows in the Somorjai group and feel it necessary to acknowledge their contributions to my growth, both personal and researchwise. All of my SFG and electrochemistry knowledge came from Steve Baldelli, the single most impressive scientist I've met (not including my dad). Steve's guidance has been supported by the awesome quartet of Zhan Chen, Aric Opdahl, Keith McCrea, and Keng Chou. I need to also thank Craig Tewell (and Elise!!), Jessica Parker, and Ella Amitay-Sadovisky, for their constant support both in and outside of the lab….great co-workers make the best friends. I will never forget anybody I've worked with in Berkeley and while the list is not exhaustive, I also thank Yong, Kevin, Steffan, Dina, Kyle, Paul, Enrico, David, Dave, and David, Frank, Telly, Jeff, Ling, Rob, Ji, Aaron, Keith and so on and so forth….

Outside of surface science I have become a more confident, loving, caring, aware individual because of the many new people I've met since moving to California and the many friends I have kept over the years. I love them all dearly and thank them for the years of support, humor, love, and friendship…Mike-thanks for making sure I did not take myself too seriously, Edwin-thanks for all you have given me in the last year, Sharon, Shara, Elise, Peter, Nanc and especially the other three from the fabulous four – Sal, Manda and Mandy – whom without I would not be Tas.

Lastly, but not least, I thank my family for their constant unconditional love and support. While I have physically moved further and further away over the last 12 years, I have emotionally grown closer and closer to them all - my Mom, Dad and my lucky little brother Phil.

This work was supported by the Director, Office of Energy Research, Office of Basic Energy Sciences, Materials Science Division, of the U.S. Department of Energy under Contract No. DE-AC03-76SF00098 and by The Polymer Technology Group, Inc., located in Berkeley, CA.

Chapter 3 is based on and includes sections from the article as published in *Surface Science,* **473**, 1999, pp. 75-85, entitled “Tensor low-energy electron diffraction analysis of the surface structure of NaCl(100) thin films grown on Pd(100) and Pt(111)” authored by J.G. Roberts, S. Hoffer, M.A. Van Hove and G.A. Somorjai.

Chapter 6 is based on and includes sections from the article as published in *Journal of Physical Chemistry B*, 2002, **106**(25), pp. 6473-6478, entitled " CO oxidation on electrified platinum surfaces in acetonitrile/water solutions studied by sum frequency generation and cyclic voltammetry" by S. Hoffer, K. Chou, S. Baldelli, P. Ross and G.A. Somorjai.

The author would like to thank Dr. Phil Ross and Dr. Keng Chou of Lawrence Berkeley National Laboratory, and Prof. Steve Baldelli of Houston University, Dr. Yuan Tian and Dr. Bob Ward of The Polymer Technology Group in Berkeley, California for their many helpful discussions concerning the work shown in this dissertation.

Table of Contents

Section II. Sum Frequency Generation Studies (SFG) of Air/Solid and Liquid/Solid Interfaces

List of Figures and Tables

Abstract

Low Energy Electron Diffraction (LEED) and Sum Frequency Generation (SFG) Vibrational Spectroscopy Studies of Solid-Vacuum, Solid-Air and Solid-Liquid Interfaces

By

Saskia Hoffer

Doctor of Philosophy in Chemistry

University of California, Berkeley, California

Professor Gabor A. Somorjai (Chair)

Electron based surface probing techniques can provide detailed information about surface structure or chemical composition in vacuum environments. The development of new surface techniques has made possible *in situ* molecular level studies of solid-gas interfaces and more recently, solid-liquid interfaces.

The aim of this dissertation is two-fold. First, by using novel sample preparation, Low Energy Electron Diffraction (LEED) and other traditional ultra high vacuum (UHV) techniques are shown to provide new information on the insulator/vacuum interface. The surface structure of the classic insulator NaCl has been determined using these methods.

Second, using sum frequency generation (SFG) surface specific vibrational spectroscopy studies were performed on both the biopolymer/air and

electrode/electrolyte interfaces. The surface structure and composition of polyetherurethane-silicone copolymers were determined in air using SFG, atomic force microscopy (AFM), and X-ray photoelectron spectroscopy (XPS). SFG studies of the electrode (platinum, gold and copper)/electrolyte interface were performed as a function of applied potential in an electrochemical cell.

Thin films of NaCl were molecularly deposited and subsequently ordered on Pd (100) and Pt (111) single crystals. The ordered structures of the films were produced by exposing a heated substrate to a flux of NaCl vapor emanating from a Knudsen cell and investigated through the use of low-energy electron diffraction (LEED). Intensity versus electron energy (IV) data sets were collected for the NaCl (100) multilayer film on both Pd (100) and Pt (111). An analysis of the I-V curves of the multilayer NaCl (100) pattern on both substrates showed that the thin films have the same structure on both substrates to a depth sampled by the electrons. Data from both systems were used in a fully dynamical LEED calculation. The optimized structure had a Pendry R-factor (R_p) of 0.16. The largest deviation from the ideally terminated NaCl (100) structure was the movement of the surface Na^+ towards the bulk, thereby causing a 0.12±0.03 Å corrugation of the surface layer.

Polyetherurethane-silicone co-polymers, with 0% to 60% silicone (by weight), were studied using several surface specific techniques in air to confirm that increasing the silicone containing groups in the bulk increased the polymer surface biocompatibility, while leaving the bulk mechanical properties relatively unchanged. IR data suggest that the etherurethane component of the polymer dominates the bulk spectra, and therefore the bulk properties, for the samples containing less than 37% silicone. In contrast, SFG surface spectra are a clear indication that the surface has been saturated with silicone at even the lowest concentrations, i.e., 10%, in the bulk. Additional SFG studies of these co-polymers in contact with water show reorientation of the CH_2 and CH_3 group at the polymer surface to minimize the interfacial free energy.

SFG vibrational spectroscopy in combination with cyclic voltammetry (CV) was used to investigate the oxidation of CO in acetonitrile (CH_3CN)/water solutions at the Pt electrode surface. CO oxidation on Pt was studied as a function of water concentration and electrode potential. In electrolyte solutions containing small concentrations of water, a pre-oxidation wave was observed at +900 mV versus the standard calomel electrode (vs. SCE) whereby a small amount of the adsorbed CO was oxidized. This pre-oxidation wave was followed by the main oxidation of CO on Pt at approximately +1700 mV vs. SCE. Spectroscopy and voltammetry data in these essentially non-aqueous electrolytes indicate an oxidation intermediate of CO to CO_2 that was nearly parallel to the Pt electrode surface.

Finally, SFG vibrational spectroscopy and CV were also used to investigate the effect of the electrode potential on electrolyte molecules. Results suggest that there is an ordering of the electrolyte molecules caused by the applied potential.

Chapter 1

Introduction

From the surface structure of single metal crystals to understanding biocompatibility of implant materials, surface physics and chemistry have been pushed to the forefront of science. To aid in the design of microelectronic devices and biomaterials, which generally have high surface to volume ratios, a basic understanding of surface properties is necessary. However, to engineer the surface properties for more functional devices and materials, research on surface properties must be performed in relevant environmental conditions.

Over the last three decades many techniques have been developed to investigate surfaces at the molecular level. While traditional electron based surface probing techniques can provide detailed information about surface structure or chemical composition in vacuum environments, the recent development of sum frequency generation (SFG) surface specific vibrational spectroscopy has made possible *in situ* molecular level studies of interfaces.

Because of their susceptibility to electron damage, insulator and polymer surfaces have been relatively unexplored frontiers in basic surface science. As shown in the first section of this dissertation, with novel sample preparation traditional surface science techniques have been used to elucidate the surface structure of NaCl in vacuum.

Successful low energy electron diffraction (LEED) studies were carried out by depositing NaCl thin films on conducting metal single crystals to prevent significant charging of the insulating films. Subsequent studies of NaCl surfaces in contact with environmentally important gases were unsuccessful, suggesting that traditional surface science techniques prove to be limited especially when studies involve probing surfaces at pressures above 5 x 10^{-5} torr.

Recent developments in the field of experimental surface science have led to the exploitation of nonlinear spectroscopy to study interfaces under more relevant conditions. The discovery and application of sum frequency generation (SFG) vibrational spectroscopy has allowed surface studies to be performed on any interface accessible by light while providing *in situ* molecular level information. In the second portion of this dissertation SFG, in conjunction with other surface analysis techniques, has been used to probe both solid/air and solid/liquid interfaces.

First, SFG, atomic force microscopy (AFM), x-ray photoelectron spectroscopy (XPS), and contact angle goniometry were used to study the viability of using block copolymers as biomaterials. Studies focused on the surface segregation of the more biocompatible components to the polymer surface. In addition, SFG was used to monitor the surface re-construction of these biopolymers in an aqueous environment.

Second, to exemplify the importance of *in situ* studies in surface science, SFG vibrational spectroscopy in combination with cyclic voltammetry (CV) was used to investigate the oxidation of CO in acetonitrile (CH_3CN)/water solutions at the Pt electrode surface. In this study, the spectroscopic and electrochemical data provided dynamical information on the CO to CO_2 oxidation reaction occurring at the electrode/electrolyte interface.

Lastly, SFG vibrational spectroscopy and CV were also used to investigate the effect of the electrode potential on electrolyte molecules. According to CV data, no chemical or physical processes, such as oxidation/reduction reactions or adsorption/desorption processes, are occurring at the potentials where spectroscopic changes were observed. Results suggest that there is an ordering of the electrolyte molecules caused by the applied potential.

Chapter 2

Low Energy Electron Diffraction

2.1 Introduction

Under suitable preparation conditions, the surface atoms of many materials are ordered [1]. By extending traditional diffraction techniques and using low energy electrons, one can probe ordered atomic surface structures. Since the early 1960s, with the development more sophisticated electron counting equipment and the increasing availability of ultrahigh vacuum equipment, low energy electron diffraction (LEED) has been used to determine hundreds, if not thousands, of surface structures.

The de Broglie wavelength of a particle is given by

$$\lambda = \frac{h}{\sqrt{2 \cdot m_e \cdot E}} \tag{2.1}$$

where λ is the wavelength of the electron wave, h is Planck's constant, m_e is the mass of the electron and E is the electron energy. Electrons with energies of about 10 to 200 eV have λs that are on the order of inter-atomic distances in solids (angstroms) and therefore satisfy the atomic diffraction condition[1]. Surface sensitivity is maintained for low energy electrons from 5-500 eV by the fact that electrons possessing these energies interact strongly with matter [2].

2.2 LEED Theory

2.2.1 Diffraction Condition

Radiation waves from electrons scattered off of surface atoms interfere constructively and destructively depending on the geometric relationship between scatters. Diffraction spots are formed when radiation from two atoms (or scatterers) constructively interfere. As shown by the Bragg Law, equation 2.2, constructive interference occurs when the path length difference of scattered radiation from scatterers a distance (d) apart is an integral number (n) times the wavelength (λ) of the radiation.

$$2d \sin \Theta = n\lambda \qquad (2.2)$$

As shown in Figure 2.1 the conditions for constructive interference between two planes can be easily visualized geometrically.

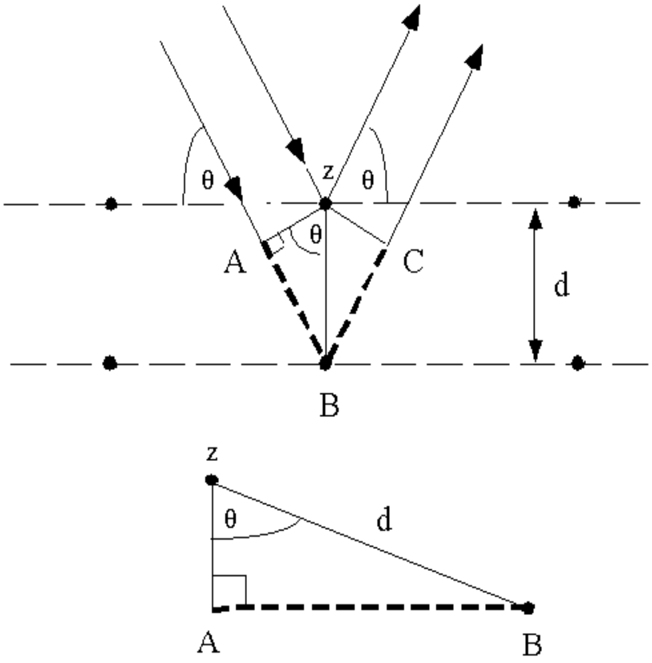

Figure 2.1 Schematic of Bragg Diffraction.

The diffraction pattern observed in LEED results from a projection of the real-space two-dimensional lattice into reciprocal space. More specifically, incident on the two scatterers is an electron plane wave with a wave vector **k**. The scattered radiation observed, wave vectors **k** and **k'**, will constructively interfere, generating a diffraction spot in reciprocal space, if the Laue equation is satisfied:

$$\mathbf{k} - \mathbf{k'} = 2\pi/d\ n \qquad (2.3)$$

where $2\pi/d$ is the reciprocal lattice vector between the two scatterers, **k** is the incident wave vector and **k'** is the scattered wave vector, and n is the number of scatterers. In a periodic solid, **d** can be replaced by **R**, the basis vectors for lattice. Under Fourier transform equation 2.3 is equivalent to:

$$\mathrm{Exp}\ i(\mathbf{k}-\mathbf{k'})\mathbf{R} = 1 \qquad (2.4)$$

By comparing equation 2.4 to the reciprocal lattice definition (equation 2.5) it can be seen that the Laue condition will be satisfied if the difference between the incident and scattered wave vectors (**k-k'**) is equal to a reciprocal lattice vector (**K**), resulting in a diffraction event.

$$\mathrm{Exp}\ (i\mathbf{K}\ \mathbf{R}) = 1 \qquad (2.5)$$

When applying this diffraction condition to a periodic array with the scatterers positioned at $d_1, d_2, \ldots d_n$ within an n-atom basis unit cell, the diffraction amplitude is dependent on the constructive interference magnitude of the radiation from these basis sites. Intensity of the diffracted beams is proportional to the square of the geometrical structure factor that is directly related to the electron density and therefore the real space structure of the solid.

From the von Laue formulation of diffraction for non-interacting radiation (e.g. x-rays) the energy is conserved in all directions. This assumption breaks down for low energy electrons, since their surface sensitivity results from their strong interaction with matter. This electron-matter interaction still requires the conservation of energy parallel to the surface, but not perpendicular to it.

For a more extensive review of diffraction techniques and LEED, the reader is directed to several good texts [3, 5, 18].

2.2.2 Nomenclature

Illustrated in Fig. 2.2(a) is a real space representation of a hexagonal surface of a face centered cubic (fcc) material (for this example, platinum). The vectors $\mathbf{a}_1$ and $\mathbf{a}_2$ represent the unit vectors of the clean surface or, for the case of clean surface reconstructions, the unreconstructed surface. These vectors define the smallest unit cell in which translations alone can recreate the clean surface, i.e. its translational symmetry. Fig. 2.2(b) shows the surface after adsorbing an overlayer. The vectors $\mathbf{b}_1$ and $\mathbf{b}_2$ define the overlayer's translational symmetry. Since the overlayer's unit cell is larger than that of the underlying substrate, the substrate can also be unambiguously created by simply copying and translating the unit cell bound by vectors $\mathbf{b}_1$ and $\mathbf{b}_2$; vectors $\mathbf{b}_1$ and $\mathbf{b}_2$ can always be expressed as a linear combination of $\mathbf{a}_1$ and $\mathbf{a}_2$.

In Wood notation [3], the overlayer unit cell size and orientation are expressed relative to the substrate's unit cell. Generally, the Wood notation has the following form.

$$\text{Substrate}(111) - w\ [(\mathbf{b}_1/\ \mathbf{a}_1) \text{ x } (\mathbf{b}_2/\ \mathbf{a}_2)]\ R_\alpha - \#\ \text{Adsorbate}$$

where w is p if the unit cell is a primitive cell and c if the unit cell described is a centered unit cell. R_α is the angle of rotation in degrees between the overlayer unit cell and the substrate's unit cell. The number (#) preceding the chemical symbol is the number of adsorbate molecules in the unit cell. The omission of w indicates that the unit cell is a primitive one, and the omission of R_α says that α is zero degrees. In the example used in Fig 2.2(b), the Wood notation would be Pt(111)-(3×3)-O.

In this work a modification of the Wood notation was needed. The overlayers grown were so thick that the underlying substrate did not contribute to the diffraction intensity, so the pattern was essentially a (1×1), but this notation does not refer to the substrate, only to the multilayer adsorbate film. For example, NaCl(100) – (1×1) on Pt(111) indicates that the pattern seen is the square (1×1) pattern associated to the (100) face of bulk NaCl and not to the hexagonal (1×1) face of Pt(111).

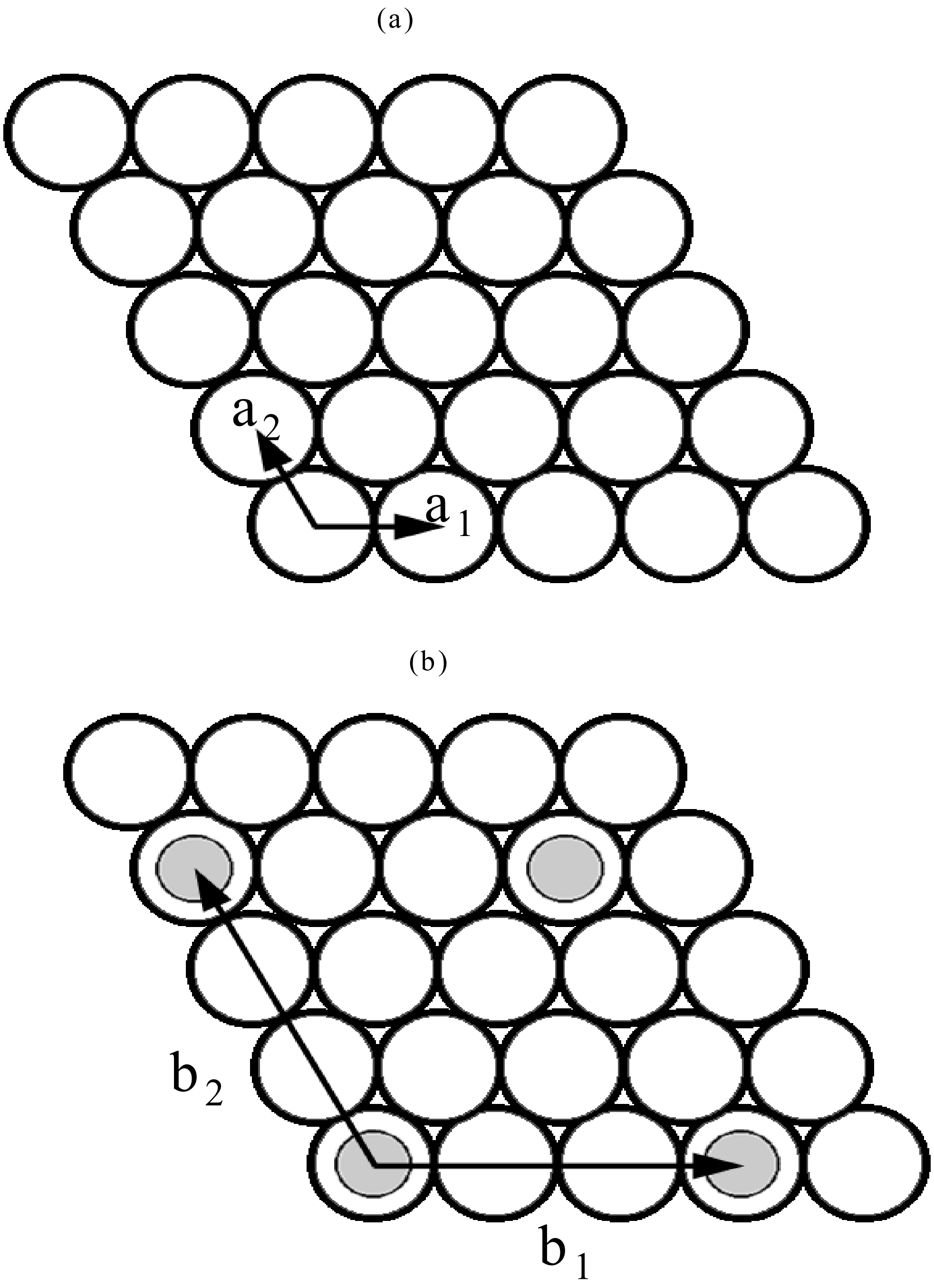

Figure 2.2   Real space diagram of a a) hexagonal surface and b) hexagonal surface with a (3x3) overlayer. The unit cell vectors are indicated by **a** and **b** for the substrate and overlayer, respectively.

2.2.3 Qualitative and Quantitative Analysis

Multiple scattering and the existence of rotational domains complicate the determination of coverage via LEED pattern analysis. Both of these effects produce a larger number of diffraction beams than is expected if the electrons are scattered by a kinematic process. Multiple scattering leads to the problem of being unable to distinguish true overlayer structures from coincidence lattices [4]. This is illustrated in figure 2.3(b) where an overlayer whose unit cell is four times larger than the substrate's produces the same LEED pattern (Fig. 2.3(a)) as an overlayer with a 4 to 3 coincidence lattice (Fig. 2.3(c))to the substrate. Extra spots are visible, since the effective unit cell is a linear combination of the surface and substrate unit cell and not just the surface unit cell alone due to multiple scattering events. For example, an incident electron can scatter off the overlayer lattice and then this scattered electron can diffract again from the substrate's surface mesh.

The effect of multiple rotated domains is the production of additional diffraction beams in the observed pattern [4]. The most common reason for the creation of multiple rotated crystalline domains is when the overlayer lattice has a lower symmetry than that of the substrate. In this situation, the higher symmetry of the substrate has to be recovered in the overall LEED pattern. This is best understood by examining Fig. 2.4. Fig. 2.4 is the real space representation of a square overlayer on a hexagonal face of an fcc substrate. In this arrangement, three domains are needed. All the overlayer atoms in these three domains interact with equivalent substrate atoms, as a result all three domains are isoenergetic to one another. This situation produces three times the number of diffraction beams due to the existence of three sets of surface unit vectors.

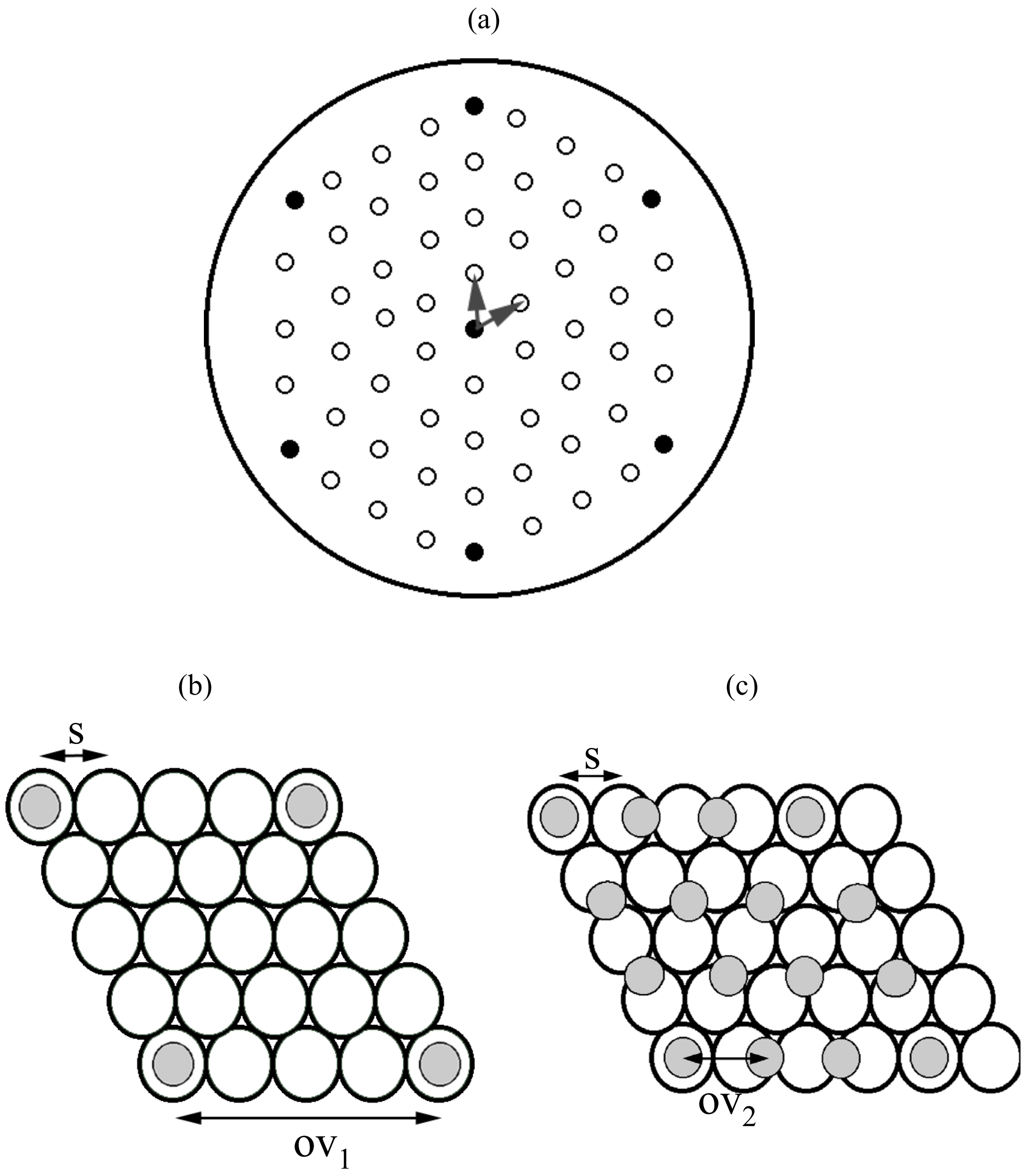

Figure 2.3 a) (4x4) LEED pattern that can arise from either b) an overlayer with a unit cell four times larger than the substrates unit cell or c) a coincidence lattice where three of the overlayers unit cells are in registry with four of the substrates unit cells.

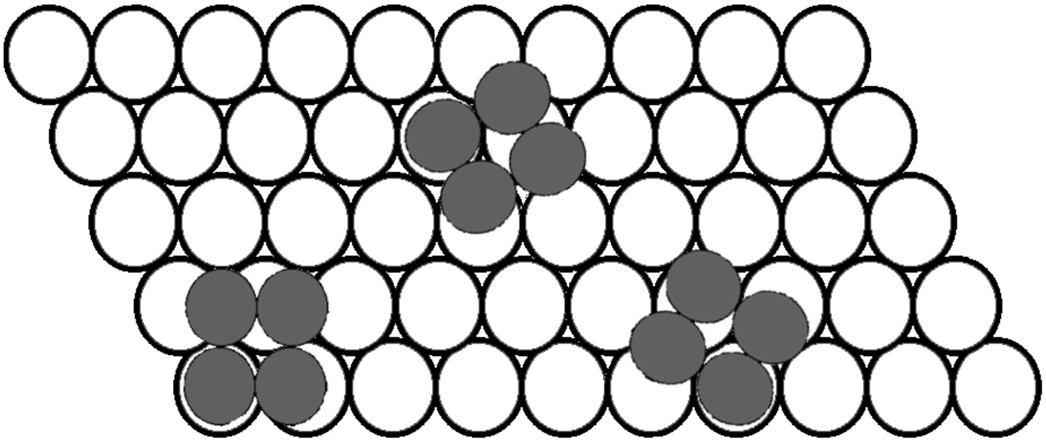

Figure 2.4 Illustration of the three domains of a square unit celled overlayer that are observed when on a hexagonal substrate. The three domains are rotated 120^o with respect to each other.

2.3 Experimental Method

Because the mean free path of an electron is on the order of microns at 1 atm, LEED has to be performed in vacuum conditions. Furthermore, to study surface properties at the atomic level we have to ensure that the surface composition remains constant during any studies. LEED studies last approximately 1 hour and by using simple kinetic theory of gases it can be shown that for a surface to remain clean for 1 hour the pressure must be approximately 10^{-9} torr, or high vacuum conditions [5].

The size of this obstacle can be seen through the application of the kinetic theory of gases, which yields a relation between molecular flux (J_M) in units of molecules per square centimeter per second, pressure (P) in torr, temperature (T) in Kelvins and molecular weight (M_w) in moles per gram [4].

$$J_M = 3.51 \times 10^{22} \frac{P}{\sqrt{T \cdot M}} \qquad (2.6)$$

The value for the number of surface sites estimated by the molecular density of Pt atoms in its unreconstructed (100) face is 1.3×10^{15}, which is representative of the metals used in this study. Through the use of ultra high vacuum technology, the length of time before the surface becomes contaminated can be extended by orders of magnitude. For example, the system, where all the experiments were performed, maintains a base pressure of 5.0×10^{-10} torr with the majority of the residual gas being carbon monoxide. With these conditions, a monolayer of gas does not adsorb for 1.45 hours. Since the preparation and the subsequent analysis of the surface occur within 40 minutes, cleanliness of the surface is assured.

2.3.1 LEED Equipment

Energy selection of diffracted electrons is performed with the use of a high pass filter constructed of four hemispherical concentric grids as illustrated in Fig. 2.5 [5]. The first grid nearest to the sample is at the ground potential, as are the electron gun drift-tube and the sample. This grid provides a field free region so that stray electrostatic fields do not deflect the backscattered electrons. The next two grids are electrically coupled and are negatively biased at a potential slightly below the electron beam energy. These grids represent the filtering section where only the quasi-elastically scattered electrons are allowed to pass. The fourth grid is also grounded to provide a field free region for post-diffraction acceleration.

In modern commercial LEED units, the diffraction pattern is visualized by post-filtering acceleration of the scattered electrons onto a fluorescent screen held at a positive potential of 2-6 kV. For a rear-view design, the screen is a Pyrex hemisphere coated on one side to allow for the viewing of the pattern from behind.

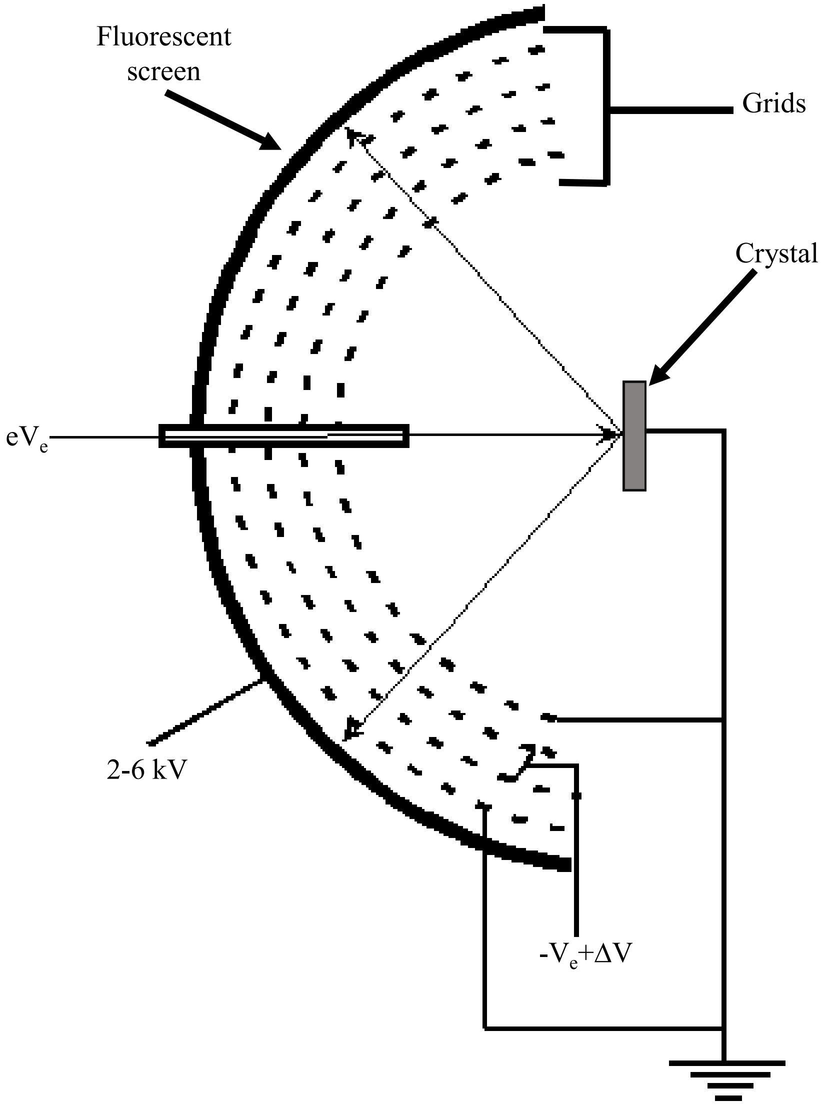

Figure 2.5 Schematic of LEED optics.

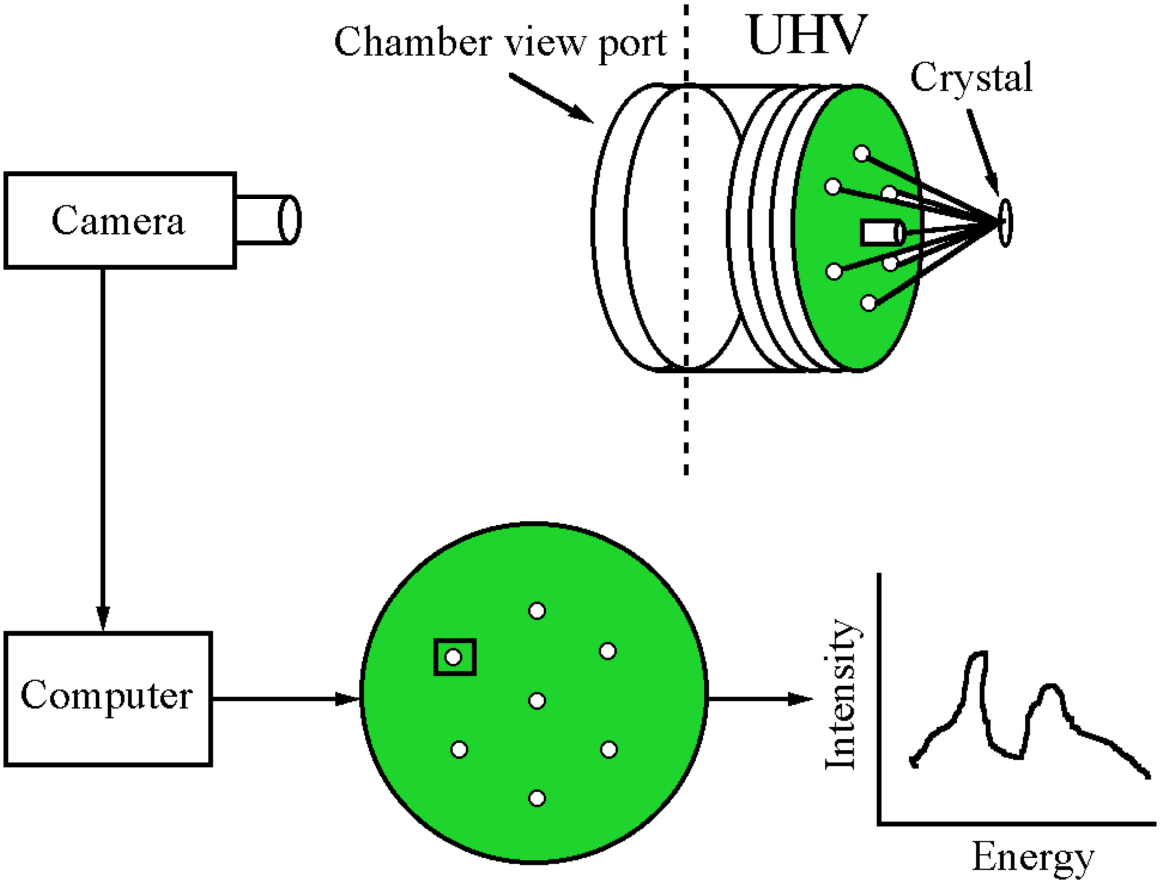

Figure 2.6 Schematic of data acquisition using a Rear-View LEED.

The source of electrons is produced by thermionic emission from a directly heated thoriated tungsten bent filament or from an indirectly heated single crystal of $LaB_6(100)$. Above 50 eV, the beam diameter is 1 mm with a coherence length of approximately 100 Å [4]. From the beam size, it can be concluded that the diffraction pattern represents an ensemble average of the multiple translation and rotational domains that is illuminated with the electron beam. The coherence length of the beam determines the minimum domain size; a smaller domain will not constructively add to the diffraction pattern.

As seen in Figure 2.6, a CCD camera records an image of the diffraction spots on the phosphorescent screen. Using a video capturing card, LEED pattern is converted to a computer readable file. Using a computer program the intensity of the diffraction beams with respect to electron voltage, an I-V curve, can be obtained.

2.3.2 UHV Chamber

All experiments were performed in a 60 liter, stainless steel UHV chamber that consisted of four 8 inch ports and four 2.75 inch ports on the side of the chamber arranged perpendicular to the chamber's vertical axis. Figure 2.7 is a schematic of the ultra high vacuum (UHV) chamber used in subsequent LEED studies. A base pressure of 5×10^{-10} torr was achieved using a turbo molecular pump and an ion pump. The chamber is equipped with a quadrupole mass spectrometer for temperature programmed desorption experiment (TPD), section 2.4.2, and to confirm the purity of the molecular vapor deposition source. Another use of the quadrupole mass spectrometer is for residual gas analysis (RGA) of the vacuum system's environment. A correction is needed to account for the differences of ionization energy between various compounds, although uncorrected pressures are published here. A final advantage of performing RGA on the system is to insure the integrity of the gas delivery system and the UHV system itself. Leaks in the gas manifold system can be seen as large amounts of N_2 and O_2 signal where there should be only pure argon, a common sputtering gas. UHV leak detection is performed with the use of helium gas flooding the possible leak area.

A cylindrical mirror analyzer is used for Auger electron spectroscopy (AES), section 2.4.3. A molecular vapor deposition source is used for chemical vapor deposition of ionic thin films onto single metal crystal substrates. Several leak valves are used to introduce gases into the chamber for gas adsorption experiments, argon ion bombardment or oxygen treatment of the surface. The UHV system contains a rear view LEED for surface diffraction studies as discussed in Section 2.3.1. Single crystal metal samples are placed on an X-Y-Z manipulator with angle and tilt capabilities. The manipulator has heating and cooling lines to control the sample temperature from -170^{o} F to $\sim 900^{o}$F.

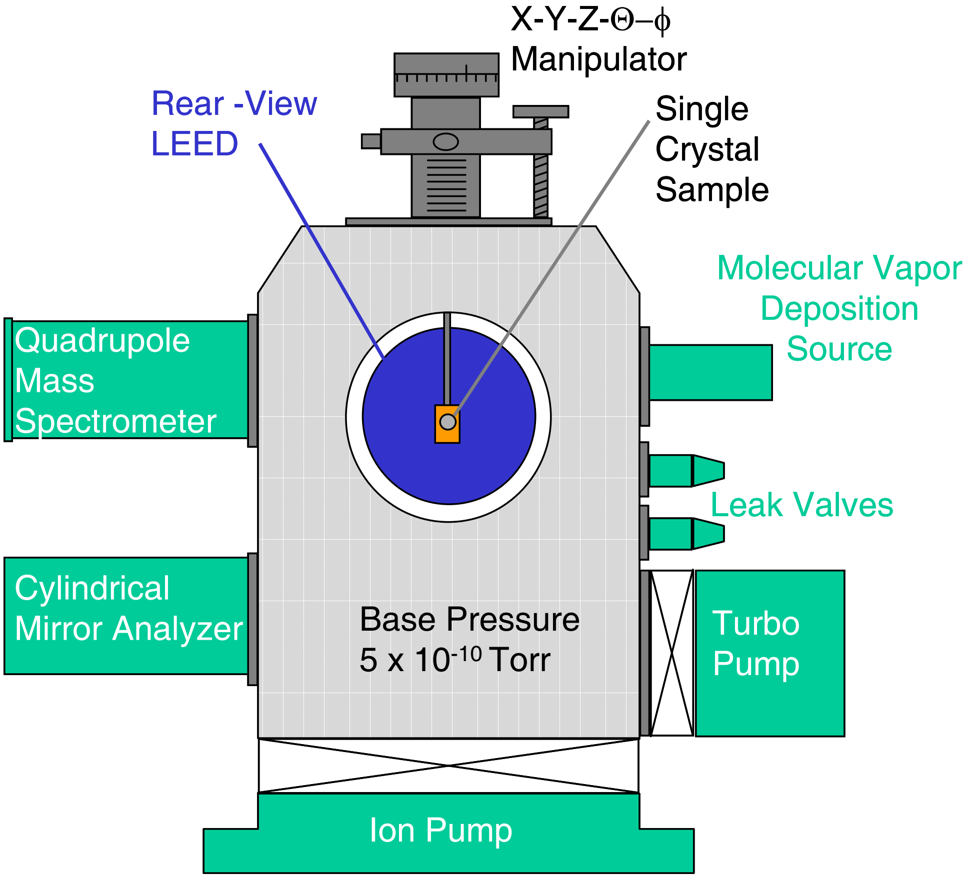

Figure 2.7 Schematic of UHV chamber.

The base pressure of $< 5.0 \times 10^{-10}$ torr is maintained through the use of a 300 L/s triode ion sputter pump. The chamber pressure is measured indirectly with a nude ionization gauge inserted into the system through one of the 2.75 in. ports located on the base well. Gases needed for cleaning the single crystal were introduced via one of the two Varian variable leak valves located on the base well of experimental chamber. The manipulator used in these experiments was an off-axis one with X-Y-Z translation and 360^{o} rotation in the plane perpendicular to the manipulator's axis and tilt.

2.3.3 Sample Holder

The sample was mounted to the manipulator by first spot welding 0.005 in. Ta foil strips to the back of the metal crystal. This assembly was then spot welded to two additional 0.030 in. Ta strips that were attached to a Mo face plate by 0-80 screws. It is important to note that in order to achieve normal incident of the Pd(111) sample to the LEED unit's electron gun, small washers were used to shim the crystal assembly by placing them below the second set of Ta strips. This faceplate was then attached the copper block that housed the heating and cooling equipment.

Heating was performed through the use of electron bombardment (e-beam). E-beam heating is accomplished by biasing a thoriated W filament located behind the crystal to ≈-1.5 kV, then the filament is slowly heated resistively by flowing 2 A of current causing thermionic emission of electrons from the filament. These energetic electrons are accelerated into the sample that is at ground. The incoming electrons induce phonon excitations within the crystal, resulting in heating of the sample.

Cooling by liquid nitrogen (LN_2) is accomplished by flowing it through the copper block where the Mo faceplate with the crystal assembly is attached. The copper block is hollowed out to allow for a continuous flow of LN_2. The LN_2 is delivered to the block by stainless steel tubes that are coiled on the vacuum side of the manipulator to allow for rotational and translational freedom. A thermocouple made from 0.005 in.

chromel and alumel wire is spot welded to the back of the crystal for monitoring the temperature.

Specialized crystal manipulators are needed for quantitative work, because of the necessity to orient the crystal at a known incidence angle to the electron gun. Another common feature, although not required, is the ability to cool the crystal below 200 K. The reason for cooling the crystal is to minimize the lattice vibrations of the solid [3]. Diffraction intensity is increased when the root mean square displacement of the atoms due to lattice vibrations is minimized. This effect is common for all diffraction techniques and has been modeled by the Debye-Waller factor. Assuming the thermal vibrations are isotropic the Debye-Waller factor takes the following form:

$$\mathrm{Exp}(2 \cdot \mathrm{M}) = \mathrm{Exp}\left[\frac{-\left(3 \cdot \hbar^2 s^2 T\right)}{m_a k_b \theta_D^2}\right] \tag{2.7}$$

Where T is the thermodynamic temperature, k_b is the Boltzman constant, θ_D is the surface Debye temperature and m_a is the atomic mass of the surface atoms. It can be seen that by decreasing the temperature this factor can be lowered, thus increasing diffraction intensity.

2.3.3.1 Sample Positioning

For quantitative work, the angle of incidence of the impinging electron beam has to be determined to within 0.5° or less. Efficient sample positioning becomes very important when working with extremely electron beam sensitive materials such as alkali halides and alkali earth halides; severe disordering of these materials results after long electron beam exposures, resulting in a finite film lifetime.

2.3.4 Substrate Preparation

For freshly polished crystals, the cleaning procedure is more time consuming, but the same steps are used for crystals that have been in vacuum before. The procedure is dependent on the material, although the common operations are sputtering with noble gas ions, chemical reduction or oxidation of contaminates and long annealings to repair the physical damage incurred by sputtering.

For Pt, the main surface impurity is carbon due to the metal's chemical activity. A majority of the carbon can be removed by annealing the crystal in 10^7 torr of O_2 to a temperature of 900°C for 2-3 min, thus oxidizing the carbon to CO and CO_2 for subsequent desorption. It is important not to anneal a Pt sample until a majority of the carbon has been oxidized, because at approximately 900°C, the carbon can form an ordered graphitic layer on the surface. This graphitic layer, which can be observed by LEED, does not react as effectively as the amorphous carbon to the oxidative treatments. To rid the surface of this graphitic contamination, multiple cycles of sputtering the surface with energetic Ar^+ ions and flashing the crystal in 10^7 torr of O_2 are performed, until the carbon is eliminated as determined by AES. Sulfur, a common bulk impurity in Pt, can be easily removed by sputtering. Long anneals in vacuum (thirty minutes to two hours) are usually required in order to have a sharp diffraction pattern.

Pd does not crack hydrocarbons as efficiently as Pt, so after the initial carbon has been oxidized, there is little need to perform multiple anneals in O_2. Since AES was the only method used in determining the cleanliness of the surface and the Pd 279 eV Auger peak overlaps with the carbon 272 eV peak, small amounts of carbon contamination could not be quantified. Sulfur is the main bulk impurity that surface segregates very readily. It can easily be sputtered away, but after annealing, a sulfur layer is always present. Since the sulfur concentration in the bulk is orders of magnitude larger than the surface area, this problem will always exist. Long anneals in vacuum and Ar^+ ions sputtering were performed repeatedly until bulk sulfur was eliminated.

2.3.5 Adsorbate Preparation

Single crystal NaCl was cleaved and crushed into a powder with a mortar and pestle. The powder was then out gassed by heating them to 350°C in vacuum for three hours.

2.3.6 LEED Data Acquisition and I-V Curve Extraction

Omicron Spectraleed electronics and optics provided the means for the visualization of the LEED patterns. A Dage-MTI silicon intensified target (SIT) camera with a Matrox real-time video capture card was used to record the LEED images for subsequent I-V extraction and signal averaging over multiple exposures. It is important to note that the automatic controls on the SIT camera were turned off while recording I-V quality diffraction information and the default setting for the frame grabber were employed. By not extracting I-V curves while obtaining the LEED data, a rapid acquisition of a full data set in less than 20 minutes of an electron beam sensitive overlayer could be accomplished. LEED intensity data collection followed a standard procedure, with the exception of a lower beam current to minimize electron beam damage to the overlayer [6]. LEED data were collected at normal incidence in 2 eV increments with a crystal temperature of ~115 K.

The benefit of the current data collection setup is the ability to perform the beam intensity extraction after the collection. Intensity extraction is performed with a computer program coded by Dr. Ulrich Starke. The user manually tracks the diffraction spots with an octagon that determines the area to be integrated. This intensity is then adjusted with respect to the background intensity. The background intensity is determined from the integration of the pixel intensity outside of the octagon. This method can be problematic if the LEED pattern is very dense, thereby causing an incorrect value for the background intensity due to the other beams being in the vicinity where the background intensity was being determined.

2.3.7 Quantitative Analysis

An in-depth description of the LEED calculations is beyond the scope of this work; the reader is referred to the references by Van Hove et al. and Pendry for a detailed discussion of the theory [7,5,8]. For an overview of the development of the dynamical scattering theory and the theoretical models used to generate surface structure models discussed in this document the reader is referred to the dissertation of Joel G. Roberts, Chapter 3.

2.4 Additional Techniques

As with many scientific studies the combination of more than one technique can provide confirmation of conclusions while also providing complimentary data to the system of study. Since LEED requires UHV conditions a number of other surface techniques are available to further study the insulating thin films. Two traditional surface techniques, temperature programmed desorption (TPD) and Auger electron spectroscopy (AES) were used extensively to probe the NaCl thin films grown in these studies.

2.4.1 Thin Film Deposition

The ionic solids are vaporized with a Knudsen cell (K-cell) of standard design (Fig. 2.8). The ionic compounds are contained in a removable crucible. The crucible material is dependent on the chemical reactivity of the adsorbate being used at the time. For NaCl, a machined molybdenum crucible was used. The increased thermal conductivity of molybdenum allowed for the deposition source to operate at a higher temperature without changing the power supply or heater design.

The crucible is housed in the removable furnace pack fabricated from high purity sintered alumina that has a double thread cut into the side to hold 0.2 in. tantalum wire. Surrounding the wire-alumina heater is a cylinder of high purity sintered alumina to electrically and thermally isolate the heater from the surrounding metal shroud. This furnace is brought up to temperature by resistively heating the tantalum wire. The temperature of the crucible is measured by a K-type thermocouple in contact with the closed end of the crucible. This assembly is then mounted in a stainless steel cylinder.

Finally, the entire assembly is surrounded by a copper shroud, which is cooled by flowing liquid nitrogen (LN_2) through the rear of it. This cooling is needed to prevent the chamber walls from heating up and to getter the desorbed gases from the whole K-cell. Manufactured into the copper shroud is a 0.19 in. orifice that can be covered with a stainless steel shutter, giving the user more accurate control over the deposition time.

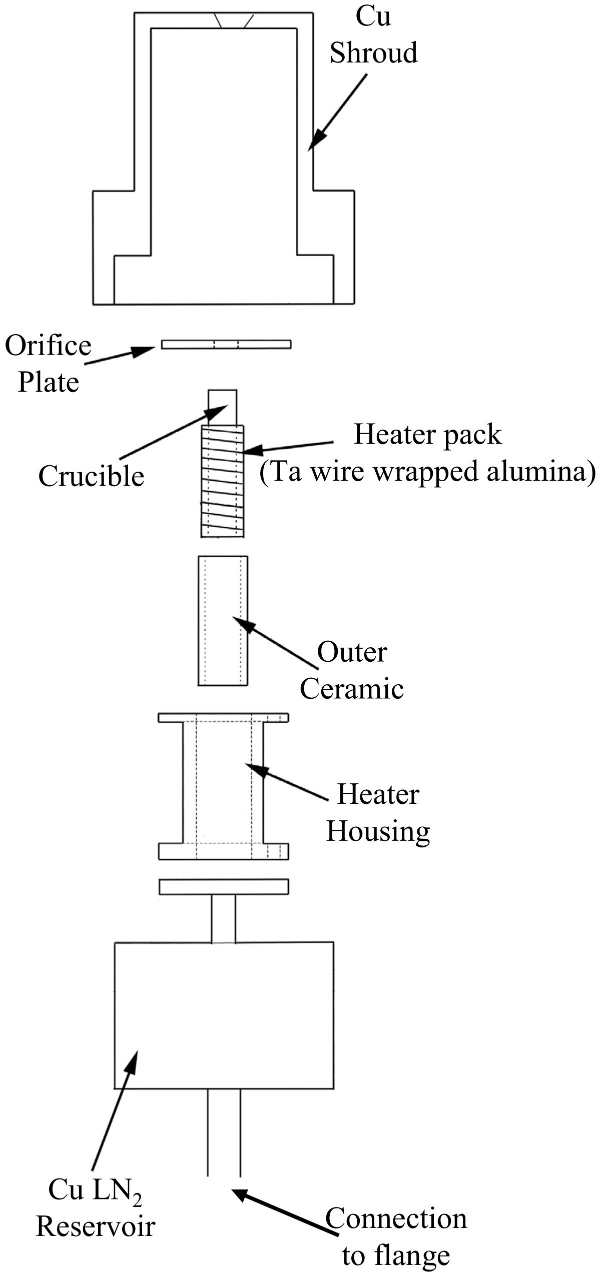

Figure 2.8 Schematic layout of Knudsen cell used for thin film deposition.

The temperature is maintained by a proportional-integral-derivative (PID) controller that feeds the required amount of current into the heater filament in response to the temperature. The controller with an on-off mode solid-state relay limits power.

Limiting the heater power is allowed through the use of a variable transformer integrated into the power supply. This adjustment is necessary, because of the PID controller's limited range.

The Knudsen cell is designed to allow no binary collisions as the molecules leave the orifice in the molecular flow regime [9]. This lack of effluent molecule interactions allows the same vibrational and rotational energy of the molecules in the low-pressure regime (in the UHV chamber) as that in the high-pressure regime (inside the Knudsen cell).

Symmetric evaporation due to the strong ionic bonding of the metal halides was witnessed in the vapor effluent. The nonsymmetrical species seen in background subtracted mass spectra are due to cracking in the electron beam [10,11,12]. Previous work documents the existence of polymeric species in the vapor composition of the thermally evaporated alkali halides. It has been published that even at temperatures well above the ones used in the experiments discussed in Chapter 3 there was no thermal cracking of the metal halides.

In the absence of a quartz crystal microbalance, the characterization of the source is done indirectly by measuring the adsorbed film thickness (d) by Auger signal attenuation (i_a) of the substrate. This reduction of Auger signal is modeled by the following equation [13, 14, 15].

$$i_a = i_0 \cdot \mathrm{Exp}\left(\frac{-d}{\lambda_0}\right) \tag{2.8}$$

where i_0 is the Auger current of the clean substrate and λ_0 is the escape depth of the electron. For Pt and Pd, their characteristic Auger transitions lie within the region of 100-800 eV, and this corresponds to film thickness maximum of 30 Å or 8-15 monolayers depending on the adsorbate's structure.

At the start of an investigation of a new adsorbate, a source temperature has to be found at which the deposition rate is large enough to grow a film before significant contamination of the substrate occurs, but also slow enough to allow an accurate measure of the deposition time. It can be seen from the Clausius-Clapeyron equation (equation 2.9) that the vapor of a material has a direct exponential dependence on temperature (T) and the enthalpy of sublimation (ΔH_{sub}), thus small changes in temperature greatly influences the vapor pressure.

$$\frac{P}{P_0} = \mathrm{Exp}\left(\frac{\Delta H_{sub}}{R \cdot T} + C\right) \tag{2.9}$$

where P is the vapor pressure of the adsorbate, P_0 is the vapor pressure at standard state, R is the gas constant and C is a constant of integration. Keeping the deposition time constant while increasing the K-cell temperature produced adsorbed films of various thicknesses. The experiments recorded herein give the response of the source with respect to the measured temperature that may differ from the actual temperature of the evaporated material because of less than perfect thermal conductivities of the source.

Once the source has been characterized, desorption behavior of the adsorbate has to be quantified and this was done with TPD. The reason for determining the substrate-adsorbate interaction is that in all the experiments a heated substrate is used to exact additional control of film thickness and to anneal the growing crystalline surface layer. In most experiments, the substrate temperature is held at the point where desorption occurs. This temperature is determined by the TPD spectra, but these spectra serve only as guide to the general temperature region. The experimental substrate temperature is usually below the one seen in TPD, because the desorption rate is inversely proportional to the adsorbate coverage. This effect is due to the formation of islands of finite size on the surface. Smaller islands of adsorbate are more easily desorbed than large islands, thus causing the desorption temperatures to shift to lower temperatures. The strong adsorbate-adsorbate interactions of the ionic solids amplify this phenomenon. A method used in finding the optimum substrate temperature includes measuring film thicknesses with the source at its predetermined temperature and varying the crystal's surface temperature. The crystal temperature that produces a film of 20 Å is chosen for subsequent experiments.

As mentioned previously, annealing of the adsorbed film occurs during deposition due to the use of an elevated substrate temperature, but additional film annealing in vacuum is also performed. These post deposition anneals have proved invaluable in working with the alkali halide films. It has been theorized that the large crystalline domains grow at the expense of the smaller ones and that the smaller domains desorb into the vacuum system during these anneals.

2.4.2 Temperature Programmed Desorption (TPD) and Residual Gas Analysis

A direct method of determining adsorbate composition is through TPD. This technique employs a mass spectrometer to monitor the desorbing species coming off the surface of the heated substrate. Usually, the surface temperature is increased linearly through the use of a PID controller, but in this experimental setup, electron bombardment heating of the sample was used, thus making automatic control difficult. The temperature ramp was performed by the experimenter and monitored by a chart recorder. The resulting temperature versus time data is then correlated to the mass signal versus time data.

Since any molecule bound to the surface is held there with some specific energy, TPD not only reveals the chemical identity of the species, but the binding energy of the desorbing molecule. Since rates come directly from experimental observations, a qualitative examination of the resulting spectra readily gives the user the order of the desorption rate and upon further analysis yields activation energies [16,17]. This can be seen by the following example for a zero desorption mechanism. Zero order desorption was the most common mechanism encountered in this work, because of the strong adsorbate-adsorbate interactions of the ionic solids. The existence of this mechanism for desorption is a product of strong adsorbate-adsorbate interaction which physically means that the adsorbate is simply condensing on the substrate from the gas phase with no regard for the composition and surface structure of the underlying substrate. Applying the Arrhenius form of the reaction constant, k, the following equation describes a zero order reaction process:

$$\frac{dN}{dT} = \frac{A}{\beta} \cdot \mathrm{Exp}\left(\frac{-E_a}{R \cdot T}\right) \qquad (2.10)$$

Where N is the number of desorbing atoms, T is the absolute temperature, , β is the heating rate, $\frac{dT}{dt}$, A is the Arrhenius pre-exponential, E_a is the activation energy for desorption and R is the ideal gas constant. Since this is a zero order process, the E_a is simply $\Delta H_{sublimation}$. Equation 2.10, a plot of $\frac{dN}{dT}$ of versus T is an exponential curve that will immediately drop to zero when the supply of adsorbate is exhausted. T_{max} is dependent upon the surface coverage of the adsorbate; the higher the coverage the larger the T_{max}. A plot of $\ln(\frac{dN}{dT})$ with respect to $\frac{1}{T}$ of the data on the exponentially rising leading edge of the spectrum gives a value for $E_{desorption}$.

2.4.3 Auger Electron Spectroscopy (AES)

AES can be used qualitatively to determine the surface species and quantitatively as a means to find surface thickness and stoichiometry of the adsorbed layer [4]. As shown in Figure 2.9, AES is a two-step process whereby an excited ion is formed when a high-energy electron ejects an electron from one of an atom's (A) inner orbitals. This excited ion A+*, then relaxes by allowing a secondary electron to fill the inner orbital vacancy, the additional energy gained by the excited atom through filling the inner orbital vacancy is used to eject another secondary electron, the Auger electron. The kinetic energy of the Auger electron is independent of the original penetrating electron beam energy.

The Auger process (Fig. 2.9) as mentioned above begins by the ionization of a core electron energy level by an incident electron. After its creation, two competing processes can annihilate the core hole:

1. An electron from a higher energy level relaxes into the core vacancy and the excess energy is given to another electron as kinetic energy through a radiationless process. (The Auger Process)
2. An electron from a higher energy level fills the core vacancy, and the resulting surplus energy is released as a photon. (X-ray Florescence)

The surface specificity of this technique, as with LEED, results from the electron's increasing probability to inelastically scatter with increased distance from the surface. The electron's attenuation length is on the order of 50 Å, since the typical Auger energies range from 10-1000 eV.

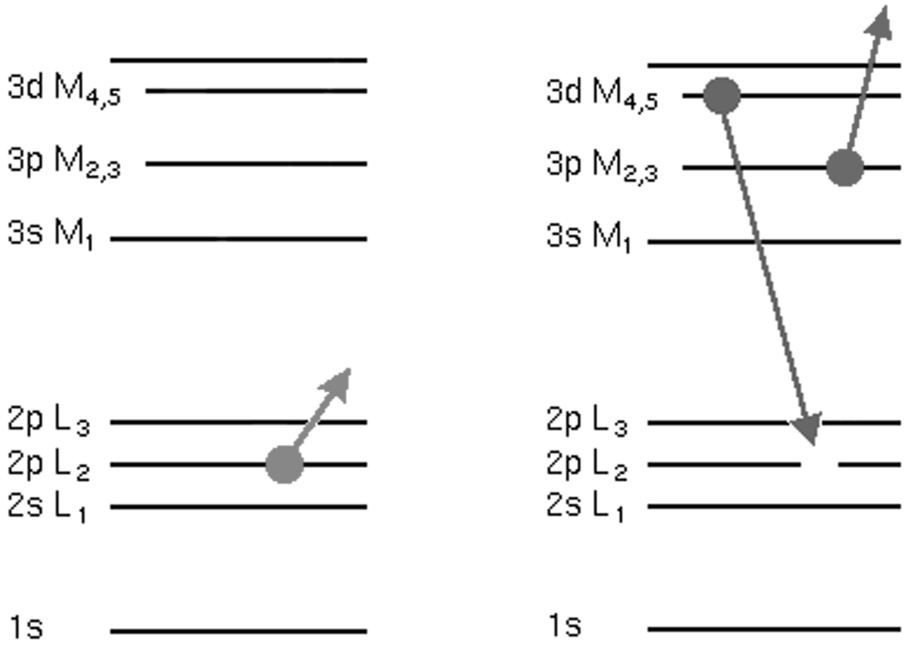

Figure 2.9 Example energy level diagram of an Auger process.

Chemical identity can be obtained from the characteristic energies of the ejected electrons. These energies can be predicted by the following equation:

$$E(L_2M_{4,5}M_{2,3}) = E(L_2) - E(M_{4,5}) - E(M_{2,3}) \qquad (2.11)$$

Where the labels L_2, $M_{4,5}$ and $M_{2,3}$ refer to the same levels as illustrated in the diagram of the Auger process, and the energies are taken from a table of the isolated atom binding energies. Equation 2.11 provides only a coarse estimate of the experimental values. Chemical sensitivity is dependent on both the ionization cross section of the material and the probability of the material to produce an Auger electron instead of an x-ray. The competition between the two relaxation processes, x-ray and Auger electron production, leads to a more complicated analysis in determining Auger electron yield.

The equipment needed to perform AES is an electron gun and an electron energy analyzer. On the PHI model 10-155 cylindrical mirror analyzer (CMA), the electron gun is integrated with the analyzer. The generated electron beam is focused to a spot of 1 mm in diameter. The ionization source produces a large slowly increasing background with the Auger peaks appearing as small peaks. This background is the result of the inelastically scattered incident electrons and their resulting secondary electrons. Differentiating the spectrum aids in the location of the individual Auger peaks. Measuring the outcoming signal at the same frequency as the reference frequency applied to the outer cylinder through the use of a lock-in amplifier gives the differential of the Auger current with respect to time.

2.5 References

1. G.A. Somorjai. *Introduction to Surface Chemistry and Catalysis,* John Wiley & Sons, Inc., New York, NY (1994).

2. R.A. Alberty and R.J. Silbey, *Physical Chemistry* (1st ed.), John Wiley & Sons, Inc., New York, NY (1992).

3. M.A. Van Hove, W.H. Weinberg and C.M. Chan, *Low Energy Electron Diffraction*, Srpinger, Berlin (1986).

4. G. Ertl and J. Kuppers, Low Energy Electrons and Surface Chemistry (2^{nd} ed.) VCH (1985).

5. D.P. Woodruff and T.A. Delchar, *Modern Techniques of Surface Science* (2^{nd} ed.), Cambridge University Press (1994).

6. J.M. Powers, A. Wander, P.J. Rous, M.A. Van Hove and G.A. Somorjai, *Phys. Rev. B*, **44** (1991), p. 11159

7. M.A. Van Hove and SY. Tong, *Surface Crystallography by LEED: Theory, Computation and Structural Results*, Springer-Verlag, Berlin (1979).

8. J.B. Pendry, *Low-Energy Electron Diffraction*, Academic Press, London (1974).

9. N.F. Ramsey, *Molecular Beams*, Clarendon Press, Oxford (1963).

10. G.M. Rothberg, M. Eisenstadt and P. Kusch. *J. Chem. Phys,.* **30** 2 (1959), p. 517.

11. R.C. Miller and P. Kusch, *J. Chem. Phys.*, **25** (1956) p. 860.

12. J. Berkowitz and W.A. Chupka, *J. Chem. Phys*., **29** (1958), p. 653.

13. T.E. Gallon, *Surface Science*, **17** (1969) p. 486.

14. D.C. Jackson, T.E. Gallon, and A. Chambers, *Surface Science*, **36** (1973) p. 381.

15. M.P. Seah, *Surface Science*, **32** (1972) p. 703.

16. P.A. Redhead. *Vacuum* **12** (1962), p. 203.

17. R.I. Masel, *Principles of Adsorption and Reactions on Solid Surfaces*, John Wiley & Sons, New York, NY (1996).

18. C. Kittel, *Introduction to Solid State Physics*, John Wiley & Sons, New York, NY (1996).

Chapter 3

LEED Analysis of NaCl(100) Thin Films on Pd(100) and Pt(111)

3. 1 Introduction

NaCl and the rest of the alkali metal halides embody the prototypical idea of an ionic crystal, which consists of charged spheres stacked in a lattice. Because the properties of NaCl can be correlated quite well, to a first approximation, to basic theories of ionic solids, the structural and electronic properties of bulk NaCl are readily found in most solid-state physics texts [1,2]. This is not the case with surface-related phenomena.

Air- and vacuum-cleaved samples of NaCl were among the first materials in which a quantitative use of low-energy electron diffraction (LEED) data was attempted to elucidate a surface structure, since NaCl was deemed to be a good candidate for the conventional single scattering theory of electron diffraction [3]. The more complicated and realistic multiple scattering theory was just starting to be developed at the time of these earlier studies, so it was not employed. Within the single scattering assumption, it was concluded that the distance between the surface and the second layer was expanded by 2.5% [3]; this result cannot be considered reliable, because such a simplistic model was employed. Since these previous studies used electron-based techniques to investigate the surface of bulk NaCl samples, the obvious problem of charge accumulation by the sample was always a factor, and it was also found that

NaCl was subject to destructive electron-stimulated desorption (ESD) of Cl anions and neutrals [4].

Charging of the NaCl was overcome by growing a thin film on a conductive substrate — a method used in our investigation of $MgCl_2$ overlayers and also by others to circumvent this common problem with large band gap materials [5, 6 , 7]. For the present work, Pd(100)and Pt(111) were used as the underlying templates for the growth of NaCl thin films. A fully dynamical tensor LEED calculation was performed on the resulting NaCl(100) thin films to determine its detailed surface structure. Beam damage was minimized during the LEED data gathering by the use of a lower than normal electron beam current (1.0 μA) and a rapid computer assisted acquisition of the data. The result of the calculation is a structure with a Pendry *R*-factor (R_P) of 0.16 where the first two interlayer spacings are reduced with respect to their bulk values by 3.5% and 1.8%. In addition to the interlayer relaxations, the position of the surface Na cations was found to be displaced deeper into the bulk than the surface Cl anions, thus creating a surface layer corrugation of 0.12 Å.

In addition to the surface structural analysis, it was found that the substrate's symmetry influences the NaCl thin film growth just as in the case of $MgCl_2$ thin films [8]. On Pd(100), the unit cell of the overlayer was rotated by 45° with respect to the substrate, so as to take advantage of the near 1:1 lattice match that presents itself when the film grows along the [010]-type surface directions. When Pt(111) was used as a substrate, the change in symmetry and the absence of the lattice constant presented by Pd(100) produced a film that grew with one of its unit cell vectors along one of the Pt(111) unit cell vectors, and the other 90° from the previous to preserve the geometry of the NaCl(100) unit cell.

3.2 Experimental Details

3.2.1 Preparation of the Pd(100) and Pt(111) substrates

All experiments were performed in a stainless steel ultrahigh vacuum (UHV) chamber, with a base pressure of $<5\times10^{-10}$ Torr, equipped with a PHI model 15-155 cylindrical mirror analyzer with an on-axis electron gun for Auger electron spectroscopy (AES), and a UTI 100C quadrupole mass analyzer for residual gas analysis and temperature programmed desorption (TPD). The Pd(100) and Pt(111) oriented crystals were prepared from commercially available boules with standard metallurgical methods, thus yielding substrates (8 mm in diameter and 1 mm thick) aligned within 0.5° of the preferred crystallographic plane. These crystals were spot welded to an off-axis manipulator with capabilities for electron bombardment heating to 1300 K from a rear mounted W filament and cooling to 110 K from an attached liquid nitrogen reservoir. The temperature was monitored with a chromel–alumel thermocouple spot welded to the substrate's back face. Major contaminants, as measured by AES, were carbon and sulfur. Carbon was removed by repeated oxidative annealings at a surface temperature of 1100 K in 5×10^{-8} Torr of O_2, and sulfur through the use of multiple cycles of 2 kV Ar^+ sputtering. Subsequent crystal annealing (2–3 h) in vacuum provided optimum LEED patterns for both substrates.

3.2.2 The LEED experiment

Omicron Spectraleed electronics and optics provided the means for the visualization of the LEED patterns. A Dage-MTI intensified camera in accompaniment with a Matrox video capture card was used to record the LEED images for subsequent *I*–*V* extraction and to signal average over multiple exposures. By not extracting *I*–*V* curves while obtaining the LEED data, a rapid acquisition of a full data set in less than 20 min of this electron-beam-sensitive overlayer could be accomplished. LEED intensity data collection followed a standard procedure [9], with the exception of a lower beam current (1.0 μA), to minimize electron beam damage to the overlayer. LEED data were collected at normal incidence with a crystal temperature of $\approx$115 K in 2 eV increments over a range of 30–350 eV for the NaCl multilayer on Pd(100) and 72–270 eV for the NaCl–Pt(111) system. To ensure normal incidence, symmetric beams were compared to confirm that the changes in the *I*–*V* curve's minima and maxima were less than or equal to 2 eV. As a check to see if the impinging electron beam caused significant damage to the ordered NaCl multilayer over the course of the data collection, data sets for both the NaCl–Pt(111) and NaCl–Pd(100) systems were taken while both increasing and decreasing the energy. It was found that peak positions deviated less than 2 eV between sets, thus providing quantitative evidence that the ordered structure largely remained intact during the data acquisition time period.

Although the electron beam damage did not compromise the long-range order of the multilayer, the detrimental effect of the beam did appear in the diffraction spot intensities, which are more sensitive to surface degradation. The result of the intensity changes is seen as a difference in relative beam intensities between a data set taken while increasing electron energy and one taken while decreasing the energy. In the *I*–*V* curves whose energy range exceeds 150 eV, the decrease of intensity with increased beam exposure caused an intensity change of 50–70% in the final maxima collected.

Symmetrically equivalent beams from both substrates were averaged, thus giving seven symmetry inequivalent beams with a total range of 1274 eV to be compared with theory.

3.2.3 Deposition of NaCl single crystal thin films

The NaCl overlayer was grown by exposing a metal crystal with a surface temperature ~600 K to a flux of NaCl vapor emitted from a heated effusion cell, using a tungsten crucible, for 20 min. The same source was used in the investigation of $MgCl_2$ thin films, and a full description can be found in a previous publication [6]. The ability of this source to produce a pure molecular flux of NaCl can be seen in the mass spectrum of the vapor flux, Figure 3.1. This spectrum is the result of subtracting out the residual gas spectrum of the chamber when the source is off from the mass spectrum taken while the source is at its operating temperature of 803 K. The features from this spectrum can be identified as $Na_2{}^{35}Cl$ and $Na_2{}^{37}Cl$ at 81–83 amu, $Na^{35}Cl$ and $Na^{37}Cl$ at 58–60 amu, ^{35}Cl and ^{37}Cl at 35–37 amu, Na at 23 amu and some residual CO at 28 amu. Based on the thermodynamic stability of the gas-phase NaCl molecule, it was determined that the Na^+ and Cl^+ peaks are the result of fragmentation of the molecules and dimers in the ionizer and not products from the deposition source [10].

3.3 Results and Discussion

3.3.1 Condensation, ordering and desorption characteristics of NaCl films

A similar method to that employed in the growth of $MgCl_2$ thin films was utilized in the ordering of NaCl on Pd(100) and Pt(111) [8]. The important element of this method is the use of a heated substrate, because at low substrate temperatures (298 K and below) NaCl resisted ordering on either substrate. The result of such an exposure, as seen by LEED, was the disappearance of the (1×1) pattern of the metal substrate because of the adsorption of a thick disordered layer of NaCl. It was found that to counteract the rapid condensation of the adsorbate, it was convenient to heat the substrate to a temperature at which there is significant desorption. This method serves three purposes:

1. Limiting the film thickness by empirically finding the balance between the NaCl adsorption and desorption rates;
2. Annealing the film at the elevated surface temperature
3. Desorbing CO, a background gas, to maintain surface cleanliness.

With the application of this procedure, NaCl was successfully ordered on Pd(100) and Pt(111) by exposing the substrate, held at a temperature on the edge of the multilayer desorption peak, to the NaCl vapor. Additional annealing to higher temperatures was then performed to induce further ordering of the film and to prepare lower coverage structures.

The first step in finding the optimum substrate temperature for deposition was to collect TPD spectra for both the NaCl–Pt(111) and NaCl–Pd(100) systems. Figure 3.2 shows the desorption profile of the Na^{35}Cl and Na^{37}Cl parent peak, *m*/*e*=58–60, adsorbed on Pt(111) and Pd(100) (Figure 3.2). The lone feature exhibits an exponentially rising initial rate with a sharp falling edge. Such a profile is indicative of multilayer desorption. A leading edge analysis of the data (Figure 3.2 inset) was performed for the NaCl–Pd(100) system with the assumption of zero-order kinetics [11]. This results in an estimate for the activation energy for desorption of 211 kJ/mol, which compares quite favorably to the heat of sublimation for NaCl of 200 kJ/mol [12]. Additional features were not observed even at lower coverages of the adsorbate.

3.3.2 LEED observations of NaCl overlayers on Pd(100) and Pt(111)

3.3.2.1 NaCl–Pd(100)

Exposing the Pd(100) crystal, which provides a complementary lattice match with the NaCl(100) surface, with a temperature of 675 K for 20 min to the effusion cell operating at 807 K produces a multilayer NaCl LEED pattern, which is represented along with the clean substrate pattern in Figures 3.3a and b, respectively. The square diffraction pattern of the multilayer film in conjunction with the lattice constant of 4.0 Å, determined from the pattern, confirm the identity of the adlayer — NaCl with the (100) orientation. Closer examination of the multilayer NaCl pattern and the clean substrate pattern, which resulted by desorbing the NaCl while maintaining the same crystal position in front of the LEED, reveals that the unit cell vectors of the multilayer are rotated by 45° with respect to the underlying Pd(100) unit cell vectors.

This orientation of the adsorbed layer with respect to the substrate is driven by the near 1:1 lattice match (within 2.5%) when the NaCl film grows along the [010]-type surface directions, i.e. along the diagonal of the Pd(100) primitive surface unit cell. Such a match does not present itself if the film grows along [011]-type surface directions, i.e. along the Pd(100) primitive surface unit cell vectors. The film thickness was estimated to be >15 Å, as indicated by the absence of the substrate spots from the LEED pattern in the energy range, 30–350 eV, used for data collection.

3.3.2.2 NaCl–Pt(111)

To determine how the chemical identity of the substrate will affect the ordering of the NaCl films, Pt was chosen as the next substrate, since there was a minimal change in the lattice constant with respect to Pd(100). Since the clean Pt(100) surface reconstructs and would create complications, we chose to use Pt(111) as the second substrate.

Two substrate preparations provided different LEED results for the adsorption of NaCl on Pt(111). For all the NaCl films on Pt(111), the NaCl source temperature was held at 807 K for a 20 min exposure. The first pattern, Figure 3.4, was produced by keeping the substrate temperature at a constant 630 K during the deposition. The pattern consists of two rings of 12 spots that result from the existence of three domains of NaCl(100) rotated by 120° relative to one another, where the first ring of spots is formed from the (1 ,0) and (0, 1) beams of their respective domains, and the outer ring from the (1, 1) beams. These isoenergetic domains result from the difference in symmetry of the hexagonal substrate and the square overlayer. A similar pattern has been seen previously for NaCl on Ge(111), but at an annealing temperature 130 K lower and with more rotational disorder than comparable patterns of NaCl on Pt(111) [5].

The second pattern, Figure 3.5a, was obtained by first maintaining a constant substrate temperature of 703 K. This diffraction pattern can be described as a ring of nonuniform intensity interspersed with discrete LEED spots, but, as documented in Figure 3.5a-c, subsequent heating to 750 K in vacuum orders the pattern to a single domain of NaCl(100). The relative orientation of the overlayer to the substrate can be witnessed through the desorption of the multilayer film, thus producing the underlying Pt(111) (1×1) pattern. Figure 3.6 shows that one unit cell vector of the overlayer (Figure 3.6a) lies parallel to one of the substrate's (Figure 3.6b) unit cell vectors. The resulting ordering of the film to one domain through desorption and/or diffusion clearly shows the very dynamic environment that the film experiences at temperatures close to the adsorbate's desorption temperature.

The lattice constant and/or the chemical identity appear to affect the ordering characteristics of the adsorbed NaCl film, since on Ge(111) no ordering of the NaCl overlayer was observed at substrate temperatures above 150 K. Instead, results indicated that a faceted NaCl(111) film grows on Ge(111) at these temperatures [5]. As with the multilayer film on Pd(100), film thicknesses of >15 Å were estimated from the absence of substrate spots from the LEED data in the measured energy range, 72–270 eV.

3.3.2.3 Comparison of LEED data from NaCl(100) grown on Pt(111) and Pd(100)

The inspection of the LEED patterns provided the initial proof that the structures of the multilayer NaCl films on Pt(111) and Pd(100) were the same within the measured energy range. Estimates for the unit cell dimensions, 4.2 Å for the film on Pt(111) and 4.0 Å for the film on Pd(100), and the fourfold symmetry of both patterns provided the needed evidence. Additional proof can be seen in the direct comparison of the LEED intensity versus electron energy (*I*–*V*) data. Figure 3.7 shows a subset of *I*–*V* curves from the films grown on Pd(100) and Pt(111). These multilayer NaCl *I*–*V* curves possess the same maxima and minima, within the experimental increment of 2 eV, with some experimental variations, thus corroborating the proposition that the NaCl film has the same structure on both substrates to a depth sampled by the low energy electrons. The most compelling and quantitative evidence for the similarity of the two multilayer films will be found in the optimized structures that result from the quantitative LEED analysis of the individual data sets.

3.3.3 LEED calculations

The analysis of the *I*–*V* curves was begun by the generation of a set of phase shifts up to $l_{\max}=9$ for neutral Na and Cl using a potential derived under the muffin-tin approximation for the unreconstructed bulk NaCl(100) lattice with the Barbieri–Van Hove phase shift package. Ionic phase shifts were not considered, based on previous work with iron oxides [7] that indicated they introduced no significant changes in either the final structure or the *R*-factor at our energies. Inelastic scattering effects that limit the penetration depth of the incoming electrons were modeled by the imaginary part of the inner potential, here being 5.35 eV. Thermal effects were represented by augmenting the phase shifts by a Debye–Waller factor.

The LEED calculations were performed with the Barbieri–Van Hove symmetrized automated tensor LEED (TLEED) package [13, 14, 15, 16]. Each layer in the (100) face of bulk-like NaCl consists of a coplanar array of alternating Cl anions and Na cations. Each Cl---Na layer was defined as a composite layer. Multiple scattering within these composite layers was treated exactly via the Beeby inversion scheme. To describe the structure, five of these composite layers were used: two defining the surface region where relaxations were allowed, and three defining the unrefined bulk. Scattering between pairs of composite layers was modeled with the renormalized forward scattering approximation [17].

For structural refinement, the TLEED approximation in combination with the Powell optimization scheme was applied. For all optimized structures, the final structure was defined as a new reference structure and the calculation was repeated, as a check on the approximation. The *R*-factor comparing theory and experiment and the error bars corresponding to the coordinates perpendicular to the surface were calculated with Pendry's formula [18].

3.3.4 Surface structural analysis

The square symmetry of the LEED pattern eliminated the other possible orientations of NaCl, such as NaCl(110), which has rectangular symmetry, and NaCl(111), which has hexagonal symmetry. The estimate for the unit cell dimension further narrowed the choice of the initial trial structures to the NaCl(100) face and modifications thereof.

The first trial structure was the ideally terminated, stoichiometric NaCl(100) surface whose lattice parameter was defined as the X-ray determined bulk value, 3.99 Å [19]. In the TLEED calculation, the only structural parameters refined were the atomic positions of the Na and Cl in the topmost two layers, while assuming the preservation of the symmetry of the original structure in the revised structure. The muffin tin zero was the only nonstructural parameter refined. The automated TLEED calculation was directed by the optimization of the Pendry *R*-factor R_P, which also represents the figure of merit for the refined models. This trial structure refined down to an R_P=0.17. Additional optimization of this model included varying the Debye temperature of the surface layer to investigate possible deviations from the bulk Debye temperature of 321 K used in the initial calculation [1]. It was found that a Θ_{Na}=270 K and Θ_{Na}=300 K improved R_P by 0.004 with no effect on the structural parameters. Figure 3.8 compares the theoretical *I–V* curves, which resulted from this last stage of refinement, to the experimental curves. The final structure with an R_P=0.16 described in Table 3.1 and illustrated in Figure 3.9 represents the structure solution for the NaCl(100) on Pd(100) and Pt(111).

The largest deviations from the bulk structure occurred in the surface layer, where the Na cations, which in the bulk would be coplanar with the Cl anions, relaxed towards the bulk and introduced a surface layer corrugation of 0.12±0.03 Å, increasing the exposure of the Cl anions at the surface. This movement of the surface Na cations was not followed by a concomitant relaxation of the Cl anions in the second layer to preserve a bulk-like interlayer spacing between the surface and second layer. The $d(Cl_2–Na_1)$ distance, where the indices number the layers, was actually reduced to 2.72±0.03 Å from the bulk value of 2.82 Å. The separation between these two ions is now less than the touching distance, 2.76 Å, between adjacent Na^+ and Cl^- in the bulk, but since there is also a loss of coordination at the surface termination, a decrease of the ionic radii is to be expected.

No detectable buckling of the anions and cations was found in the second layer where the intralayer spacing was Δ_2=0.01±0.03 Å. As with $d(Cl_2–Na_1)$, the second interlayer spacing $d(Na_3–Cl_2)$ was compressed from the bulk value, 2.82 Å, to 2.77±0.03 Å;

unlike $d(Cl_2–Na_1)$, however, this spacing can accommodate the close packing of bulk-like ions.

Since the bulk value of the lattice constant is not consistent with a close packing of the ions with the published values of their ionic radii [20], it was decided that another reasonable trial structure can be made by shrinking the unit cell from a lattice constant of 3.99 Å to 3.90 Å. The same structural and nonstructural parameters were refined in this model as in the previous one. This model refined down to a chemically reasonable structure, albeit with a higher R_P of 0.19. Similar shifts found in the structural solution described above were also present here, such as the displacement of the Na towards the bulk and the lack of any significant shifts below the surface layer. The main difference between this structure and the previous one was found in the first interlayer spacing, more specifically $d(Cl_2–Na_1)$. In the compressed lattice model the $d(Cl_2–Na_1)$ was found to be 2.67 Å; this implies there has to be a 3.3% contraction of the ionic radii, which is over twice as large as is needed in our first model.

By splitting up the combined data set used in the previous calculations and performing a fully dynamical TLEED analysis on the NaCl–Pd(100) and NaCl–Pt(111) data sets individually, the similarity of the multilayer film structure can be fully quantified. This separation reduces the cumulative energy range to 1100 eV for Pd(100) and 1004 eV for Pt(111), but these ranges provide adequate information for analysis. The initial trial structure for both calculations was the ideally terminated stoichiometric NaCl(100) surface with the bulk unit cell dimension of 3.99 Å — the same initial structure that resulted in the structural solution for the combined data set. As with the previous analyses, the same structural and nonstructural parameters were refined with the exception of the Debye temperatures. Both data sets converged on optimized structures with *R*-factors of 0.16 for the Pd(100) data and 0.21 for the Pt(111) data. Although possessing different *R*-factors, all the resulting structures from the Pd(100), Pt(111) and the combined data set TLEED calculations have the same value for the two intralayer spacings (Δ_1 and Δ_2) and first interlayer spacing, $d(Cl_2-Na_1)$, within the statistical error bars (Table 3.2) The largest structural difference between the data sets was seen in the value for the second interlayer spacing, $d(Na_3-Cl_2)$, but these values are within one standard deviation of one another. The difference in *R*-factor between the Pd(100) and Pt(111) data sets is primarily due to experimental variations that resulted from obtaining these data from two separate experiments.

3.4 Summary and Conclusions

NaCl has been successfully ordered in its (100) orientation on Pt(111) and Pd(100). The chemical identity of the substrate did not affect the film growth characteristics, but the underlying substrate symmetry had an influence on the azimuthal film orientation: in the case of Pt(111), the overlayer grew along one of the unit cell vectors of the substrate, but for Pd(100), which has a lattice constant within 1% of Pt(111), the film's unit cell vectors were rotated by 45° from the substrate's. Although there was an observable difference in the film growth between the different substrates, the comparison of the optimized structures that resulted from the LEED *I–V* analysis of the data taken from both substrates confirms that the multilayer films have the same surface structure to the depth sampled by the low energy electrons. Desorption characteristics are also shared by the two substrates, evidenced by the TPD curves whose only feature was a zero-order multilayer desorption peak.

Complete LEED data sets were acquired from both substrates, and a fully dynamical LEED calculation was performed to determine the structure. Deviations from the bulk NaCl(100) atomic positions were a 3.5% and 1.8% compressions of the first and second interlayer spacings, $d(Cl_2\text{–}Na_1)$ and $d(Na_3\text{–}Cl_2)$, respectively, and the movement of the surface Na cations into the bulk thereby causing a buckling of 0.12 Å at the surface termination. This buckling of the surface has been theoretically predicted due to the different electron polarizabilities of the ions at the (100) surface [21]. This difference would lead to an unequal relaxation of the surface layer so as to leave the anions above the cations. Although buckling of the (100) surface of a rocksalt structure has been seen previously, e.g. in MgO(100) [22 , 23], this work represents the first evidence for this effect in alkali metal halides, the compounds for which this phenomenon was originally predicted. Future experiments on other alkali metal halides will look for changes in surface corrugation as a function of ion polarizability as well as ordering characteristics of these compounds on various transition metal substrates.

3.5 References

1. N.W. Ashcroft and N.D. Mermin. *Solid State Physics* Saunders College Publishing, Fort Worth, TX (1976).

2. C. Kittel. *Introduction to Solid State Physics* (7th ed. ed.), Wiley, New York (1996).

3. I. Marklund and S. Andersson. *Surf. Sci.* **5** (1966), p. 197.

4. H. Tokutaka, M. Prutton, I.G. Higginbotham and T.E. Galloy. *Surf. Sci.* **21** (1970), p. 233.

5. S. Fölsch, U. Barjenbruch and M. Henzler. *Thin Solid Films* **172** (1984), p. 123.

6. D.H. Fairbrother, J.G. Roberts, S. Rizzi and G.A. Somorjai. *Langmuir* **13** (1997), p. 2090.

7. A. Barbieri, W. Weiss, M.A. Van Hove and G.A. Somorjai. *Surf. Sci.* **302** (1994), p. 259.

8. D.H. Fairbrother, J.G. Roberts and G.A. Somorjai. *Surf. Sci.* **399** (1998), p. 109.

9. J.M. Powers, A. Wander, P.J. Rous, M.A. Van Hove and G.A. Somorjai. *Phys. Rev. B* **44** (1991), p. 11159.

10. G.M. Rothberg, M. Eisenstadt and P. Kusch. *J. Chem. Phys.* **30** 2 (1959), p. 517.

11. P.A. Redhead. *Vacuum* **12** (1962), p. 203.

12. L.B. Pankratz. *Thermodynamic Properties of Halides* Unites States Department of the Interior, Bureau of Mines, Washington, DC (1984).

13. M.A. Van Hove, W. Moritz, H. Over, P.J. Rous, A. Wander, A. Barbieri, N. Materer, U. Starke, D. Jentz, J.M. Powers, G. Held and G.A. Somorjai. *Surf. Sci.* **287–288** (1993), p. 432.

14. M.A. Van Hove, W. Moritz, H. Over, P.J. Rous, A. Wander, A. Barbieri, N. Materer, U. Starke and G.A. Somorjai. *Surf. Sci. Rep.* **19** (1993), p. 191

15. (http://electron.lbl.gov/software/).

16. P.J. Rous. *Prog. Surf. Sci.* **39** (1992), p. 3.

17. M.A. Van Hove, W.H. Weinberg and C.-M. Chan. *Low-Energy Electron Diffraction* Springer, Berlin (1986).

18. J.B. Pendry. *J. Phys. C* **13** (1980), p. 937.

19. S.C. Abrahams and J.L. Bernstein. *Acta Crystallogr.* **18** (1965), p. 926.

20. A. Kelly and G.W. Groves. *Crystallography and Crystal Defects* Addison-Wesley, Reading, MA (1970).

21. G.C. Benson and T.A. Claxton. *J. Chem. Phys.* **8** (1968), p. 1356.

22. M.R. Welton-Cook and W. Berndt. *J. Phys C* **15** (1982), p. 5691.

23. D. Ferry, J. Suzanne, V. Panella, A. Barbieri, M.A. Van Hove and J.-P. Biberian. *J. Vac. Sci. Technol. A* **16** 4 (1998), p. 2261.

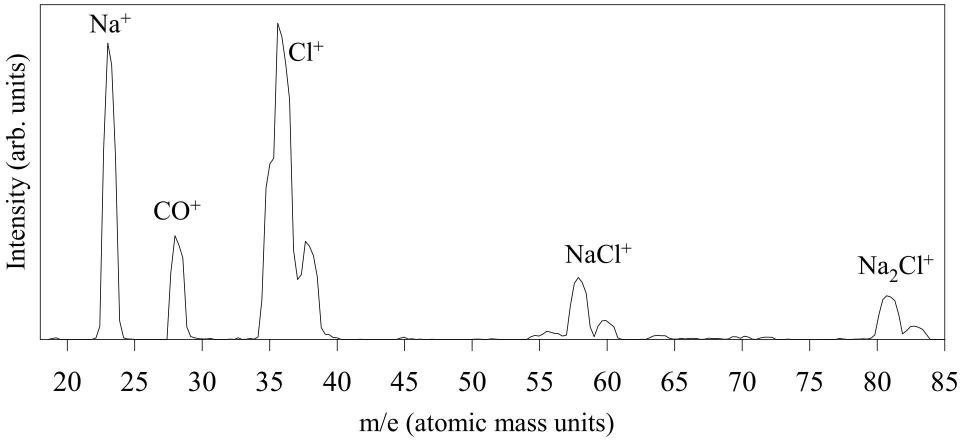

Fig. 3.1. Background-subtracted mass spectrum of the source effluent with the source operating at 803 K.

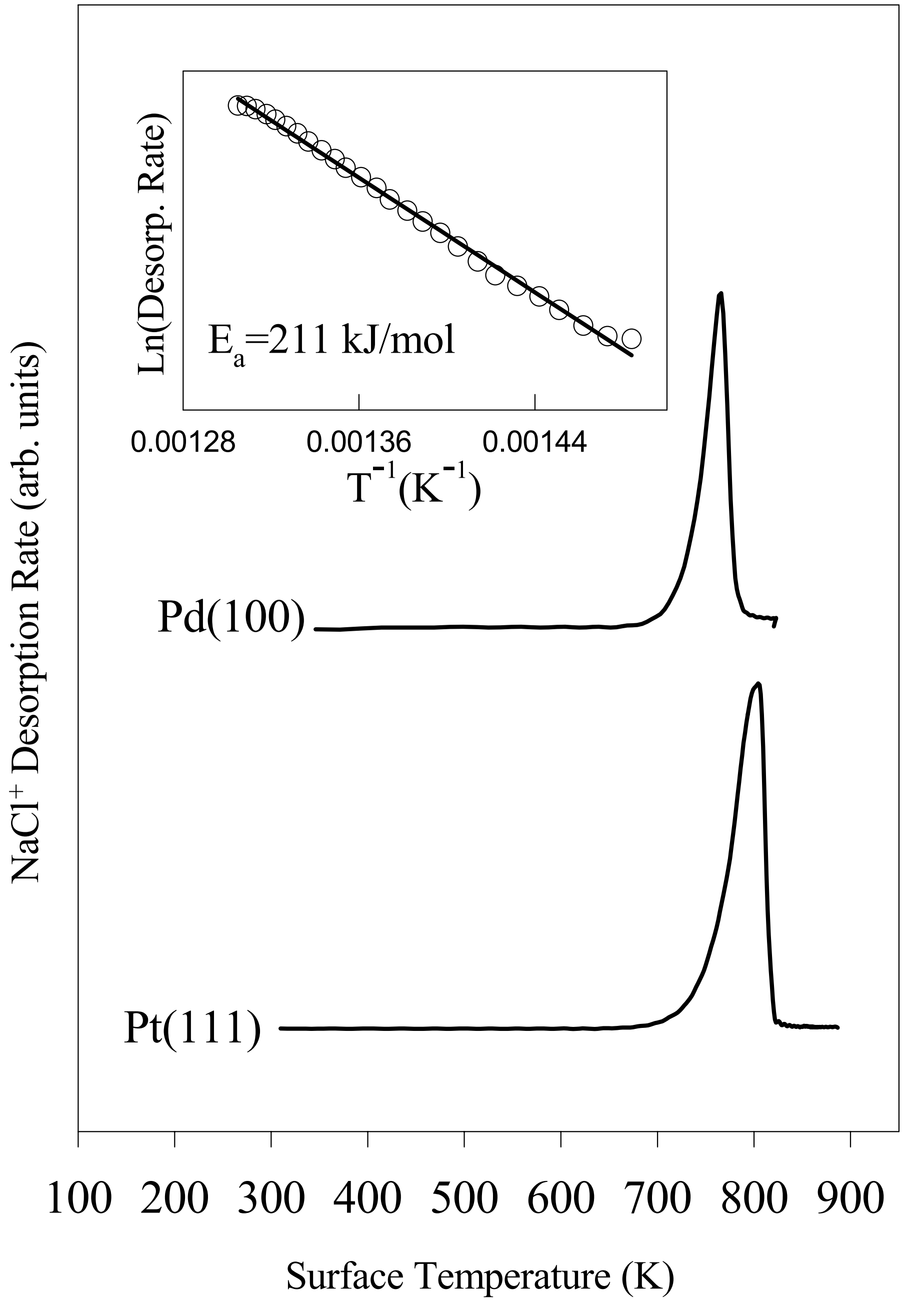

Fig. 3.2. TPD profiles of multilayer NaCl films adsorbed on Pt(111) and Pd(100). The additional graph inset in the top left illustrates the results of the leading edge analysis of the feature seen in the Pd(100) TPD, which yields an activation energy for desorption of 211 kJ/mol. The open circles represent the data and the solid line is the linear regression. It should be noted that a smoothing of the data was performed to filter out an oscillation that resulted from scanning over the *m*/*e* range of 58–60.

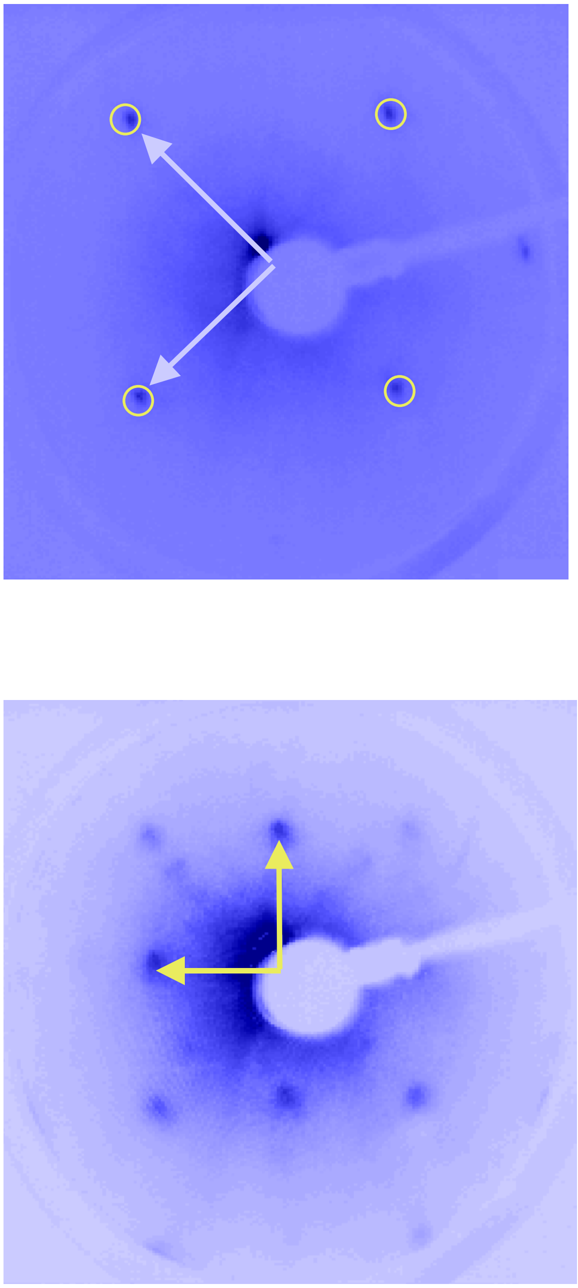

Fig. 3.3. LEED patterns for (a) NaCl(100)-(1×1) on Pd(100) and (b) a clean Pd(100)-(1×1) surface after desorbing the NaCl overlayer, showing that the overlayer grows along the diagonal of the Pd(100) unit cell. Both images were recorded at the same sample position and incident energy of 65 eV and are plotted with negative contrast for clarity.

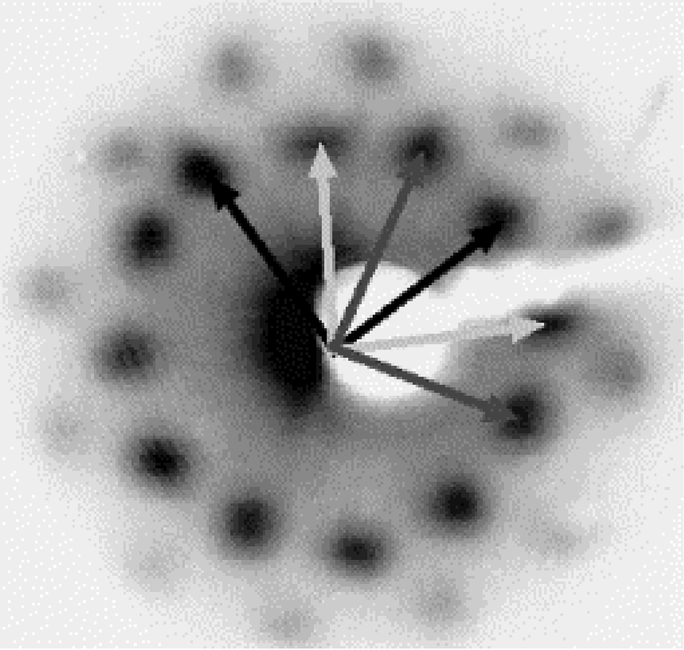

Fig. 3.4. LEED pattern of a multilayer NaCl film grown on Pt(111), recorded at an incident electron energy of 63 eV, illustrating the three rotational crystalline domains.

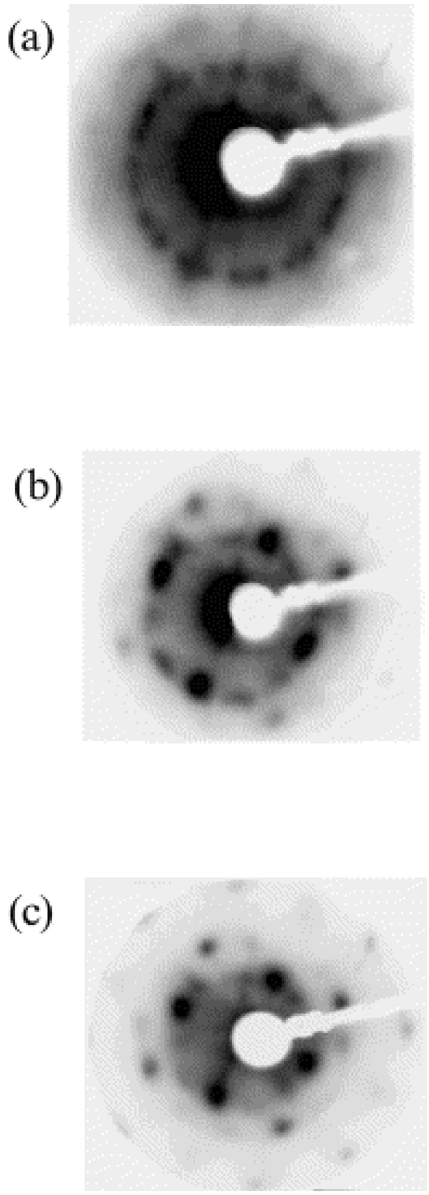

Fig. 3.5. (a) LEED pattern resulting from the adsorption of a multilayer NaCl film on a substrate heated to 703 K during deposition. The pattern was recorded at an incident electron energy of 60 eV. (b) LEED pattern of the film seen in (a) after a 1 min anneal at a surface temperature of 708 K at an incident energy of 60 eV ,showing how heating drives the film to become less rotationally disordered. (c) LEED image of the same film after annealing it at a surface temperature of 748 K where only one domain exists. An incident energy of 80 eV was used.

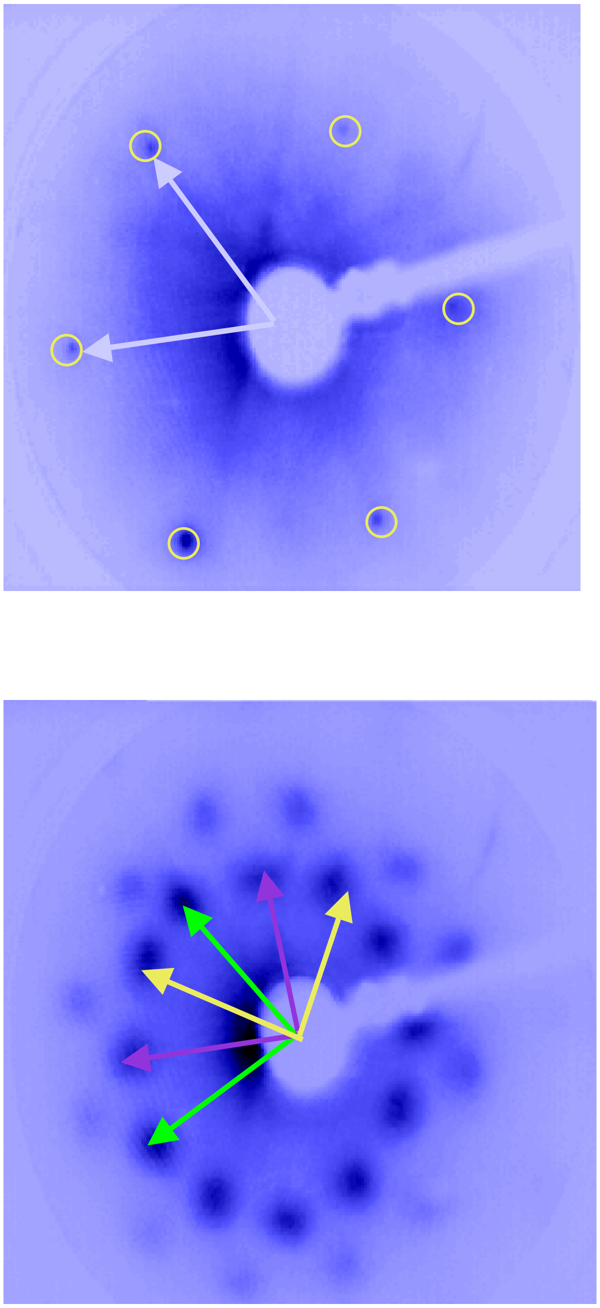

Fig. 3.6. Comparison of the LEED pattern of (a) an NaCl multilayer on Pt(111) recorded at an incident energy of 84 eV and (b) a clean Pt(111) recorded at an incident energy of 85 eV to show the relative orientation of the overlayer to the substrate.

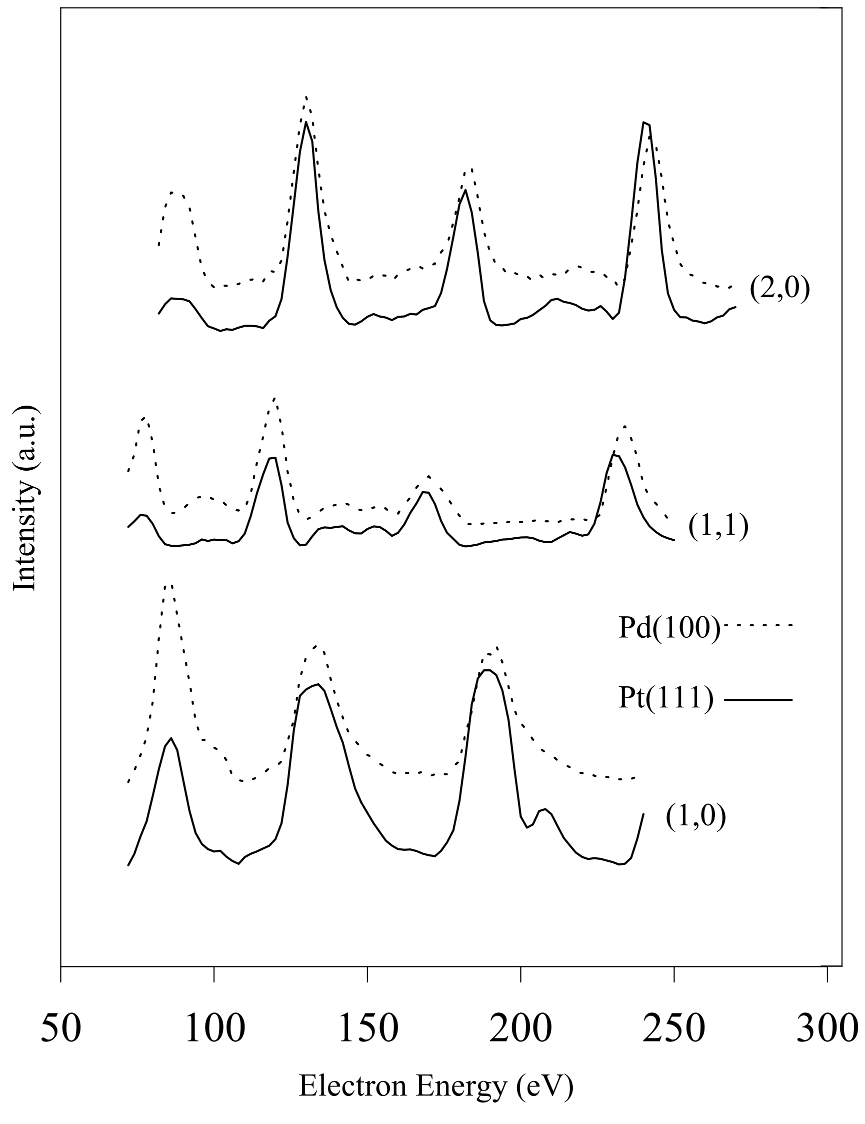

Fig. 3.7 Comparison of selected *I*–*V* curves from multilayer NaCl films on Pt(111), solid lines, and Pd(100), dashed lines. The curves' intensities were approximately normalized to ease comparison.

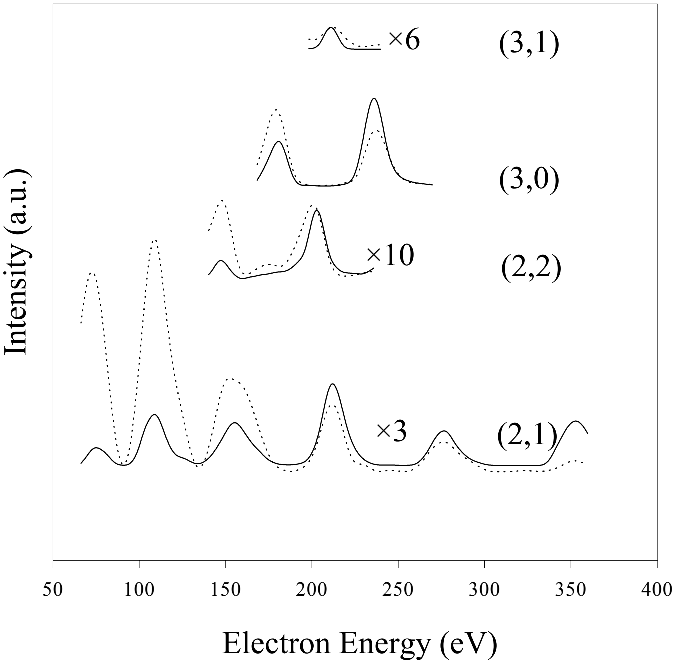

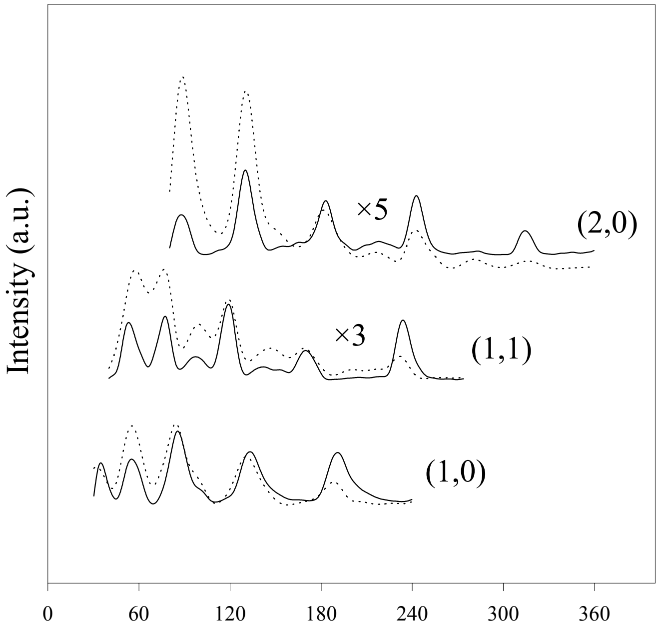

Fig. 3.8. Comparison of the theoretical (dashed lines) and the experimental (solid lines) *I–V* curves of the fully optimized NaCl(100) structure. All the beams used in the calculations are presented here.

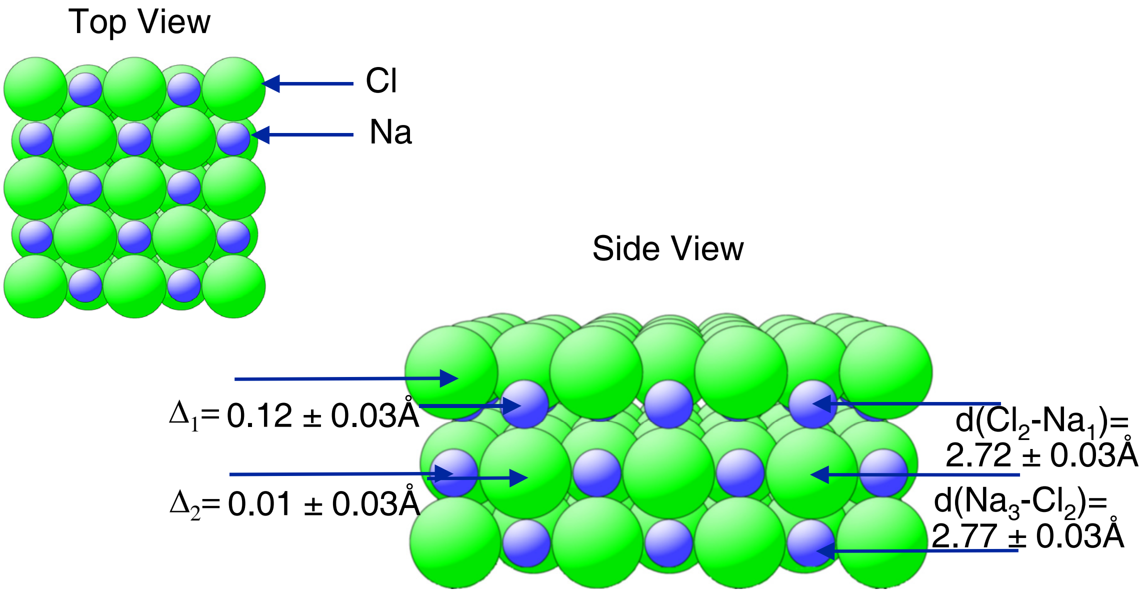

Fig. 3.9. Top view (at left) and side view (at right) of the optimized NaCl(100) surface grown on Pd(100) and Pt(111) (the surface termination is on top); the ionic radii were drawn reduced by 20% for clarity. The values of the interlayer and intralayer spacings in the refined region are shown. The bulk spacings are $\Delta_1=\Delta_2=0.00$ Å and $d(\mathrm{Cl}_2\text{–}\mathrm{Na}_1)=d(\mathrm{Na}_3\text{–}\mathrm{Cl}_2)=2.82$ Å.

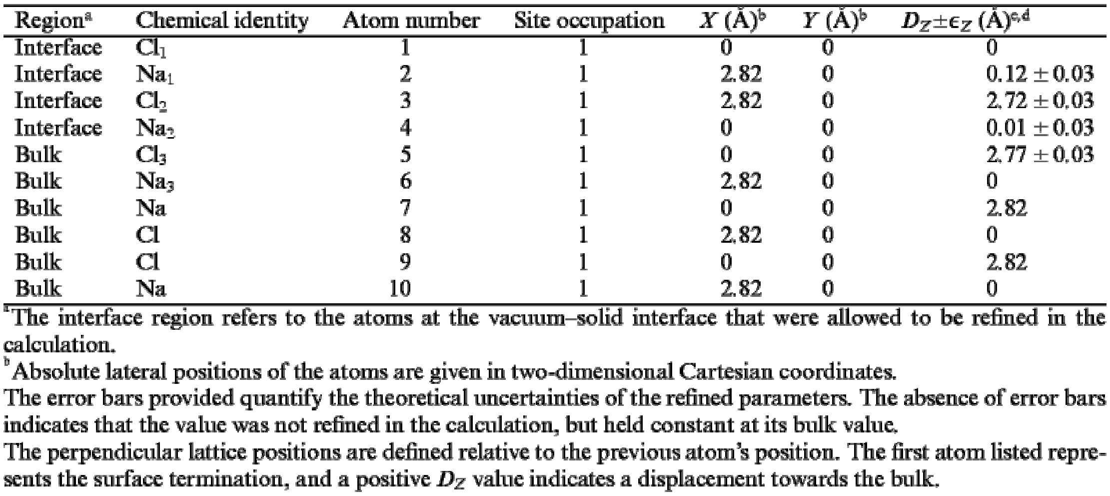

Region[a]	Chemical identity	Atom number	Site occupation	X (Å)[b]	Y (Å)[b]	$D_Z \pm \epsilon_Z$ (Å)[c,d]
Interface	Cl_1	1	1	0	0	0
Interface	Na_1	2	1	2.82	0	0.12 ± 0.03
Interface	Cl_2	3	1	2.82	0	2.72 ± 0.03
Interface	Na_2	4	1	0	0	0.01 ± 0.03
Bulk	Cl_3	5	1	0	0	2.77 ± 0.03
Bulk	Na_3	6	1	2.82	0	0
Bulk	Na	7	1	0	0	2.82
Bulk	Cl	8	1	2.82	0	0
Bulk	Cl	9	1	0	0	2.82
Bulk	Na	10	1	2.82	0	0

[a] The interface region refers to the atoms at the vacuum–solid interface that were allowed to be refined in the calculation.

[b] Absolute lateral positions of the atoms are given in two-dimensional Cartesian coordinates.

The error bars provided quantify the theoretical uncertainties of the refined parameters. The absence of error bars indicates that the value was not refined in the calculation, but held constant at its bulk value.

The perpendicular lattice positions are defined relative to the previous atom's position. The first atom listed represents the surface termination, and a positive D_Z value indicates a displacement towards the bulk.

Table 3.1. Full description of the refined NaCl(100) structure. The subscripts on the atom labels correspond to the subscripts used in the text and Figure 3.9.

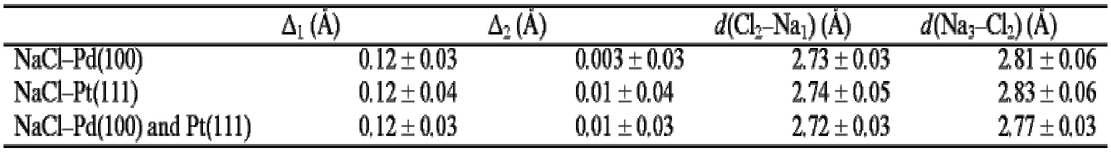

	Δ_1 (Å)	Δ_2 (Å)	$d(Cl_2–Na_1)$ (Å)	$d(Na_3–Cl_2)$ (Å)
NaCl–Pd(100)	0.12 ± 0.03	0.003 ± 0.03	2.73 ± 0.03	2.81 ± 0.06
NaCl–Pt(111)	0.12 ± 0.04	0.01 ± 0.04	2.74 ± 0.05	2.83 ± 0.06
NaCl–Pd(100) and Pt(111)	0.12 ± 0.03	0.01 ± 0.03	2.72 ± 0.03	2.77 ± 0.03

Table 3.2. Comparison of the values for the refined intralayer and interlayer spacings determined for all three data sets: NaCl on Pd(100), NaCl on Pt(111) and the combined Pd(100) and Pt(111) data set. The labels correspond the regions discussed in the text and illustrated in Figure 3.9.

Chapter 4

Sum Frequency Generation Surface Specific Vibrational Spectroscopy

4.1 Introduction

Infrared (IR)-visible (VIS) Sum Frequency Generation (SFG) vibrational spectroscopy is a novel spectroscopic technique that provides surface specific vibrational information. Simply, a tunable IR laser beam excites a molecule at an interface into a vibrationally excited state, while a second photon in the visible frequency range excites the molecule into a virtual state. When the molecule relaxes it releases a photon at the sum of the IR and visible frequencies. Therefore, for a given molecule at an interface to be SFG active it must have both a strong dipole moment (IR active) and a large polarizibility (Raman cross-section).

SFG spectroscopy probes the second order nonlinear susceptibility, $\chi^{(2)}$ of a material. Under the electric dipole approximation, even-ordered nonlinear processes (i.e., $\chi^{(2)}$ and $\chi^{(4)}$, etc.) are necessarily zero in centrosymmetric media. Therefore sum-frequency signal can be obtained from an interface where the symmetry is broken, while no signal is observed from the centrosymmetric bulk. Due to these symmetry arguments SFG spectroscopy has sub-monolayer sensitivity.

As seen in Figure 4.1, SFG offers an advantage over traditional surface science and spectroscopy techniques. Traditional surface techniques use electrons as probes. Since the mean free path of an electron depends on density of molecules, many traditional surface techniques, while highly surface specific, can only be used to probe surfaces in UHV conditions.

Linear vibration spectroscopy requires a reference spectrum to normalize out any bulk contribution to the signal. In contrast, SFG vibrational spectroscopy can be performed at any interface accessible by light, including buried interfaces such as the electrode/electrolyte interface [1-5], while no reference spectra is required for data interpretation.

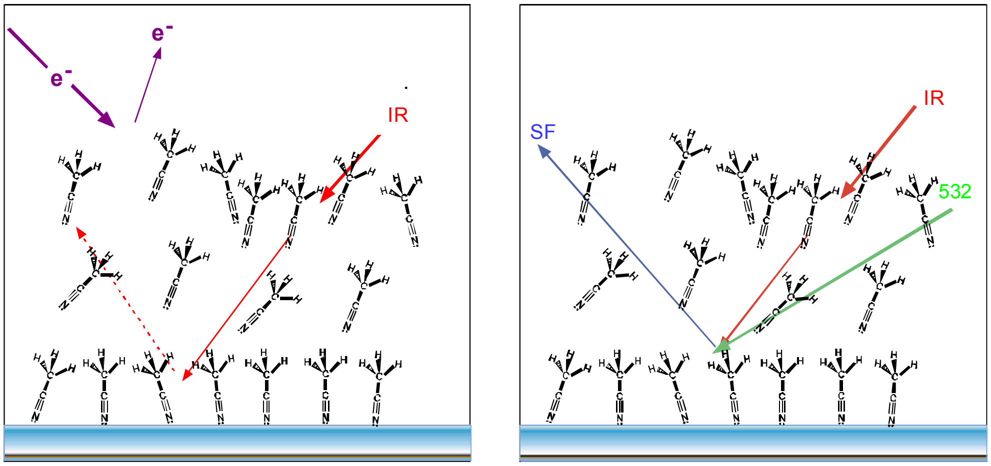

Figure 4.1 – a) High molecular density limits surface sensitivity for linear spectroscopy while b) SFG vibrational spectroscopy is not severely affected by molecules in the bulk phase.

4.2 Sum Frequency Generation Theory

The theory of SFG as used in surface studies has been described in great detail in several review and feature articles [4-6]. The basic of this non-linear spectroscopic technique are outlined here to help the reader better understand the experimental considerations and the data analysis for the SFG experiments performed and described in the following chapters.

In linear spectroscopy, the probe light is also collected as signal light. For example, in FTIR IR light is either passed thru or reflected of a sample and then the remaining IR light is measured. The percent absorption or transmission of this light is then related to the type and number of molecular groups present at a surface. In contrast, in nonlinear spectroscopy the probe light and the light used in detection have different frequencies.

When mixing two high-energy electric fields the polarization induced in a material is no longer uniquely linear. As seen in equation 4.1, the induced polarization P(E) includes second and higher order terms:

$$P(E) = P^{(1)} + P^{(2)} + P^{(3)} = \varepsilon^{o} (\chi^{(1)}E + \chi^{(2)}E{:}E + \chi^{(3)}EEE + \ldots\ldots\ldots) \qquad (4.1)$$

where P is the induced polarization, ε^{o} is the permittivity of free space, E is an electric field and $\chi^{(1)}$ is the first order susceptibility and $\chi^{(2)}$ is the second order nonlinear susceptibility.

In an SFG experiment the electric fields are mixed, one with mid IR frequency, E_{IR} and one with visible frequency, E_{VIS}. A closer look at $P^{(2)}$, the polarization induced when mixing two field, and by inserting the correct waveform of the two electric fields, $E(r)\cos(\omega t)$, we obtain:

$$P_i^{(2)} = 1/2\varepsilon^o \Sigma_{jk} \chi_{ijk}^{(2)} E_{j,\,VIS}(r) E_{k,\,IR}(r) [\cos(\omega_{VIS} + \omega_{IR})t + \cos(\omega_{VIS} - \omega_{IR})t] \qquad (4.2)$$

Here it can be seen that light is generated at the sum, $\omega_{SF} = \omega_{VIS} + \omega_{IR}$ and at the difference, $\omega_{DF} = \omega_{VIS} - \omega_{IR}$, of the two input frequencies.

As shown in Figure 4.2, at a given interface or in any non-centrosymmetric media both the sum frequency, SF, and difference frequency, DF, are generated by mixing tunable IR and 532 laser beams. In SFG, as previously mentioned, the IR photon excites a molecule into a vibrationally excited state, and the visible photon excites the molecule into a virtual state. When the molecule relaxes it releases a photon at the sum of the IR and visible frequencies. In DFG, the visible photon excites the molecule into a virtual state. The excited molecule then relaxes to a vibrationally excited state releasing a photon at the difference frequency. Both DFG and SFG principles are used in generating the tunable IR laser used in SFG studies; however after mixing the IR and visible beams on an interface, only the SF signal is collected. This is due to the fact that the SF beam has been optimized by the particular geometric arrangement of the optics layout used and in general is the easier one to collect and analyze using conventional photon counting equipment.

$$P(E) = \varepsilon_o(\chi^{(1)}E + \chi^{(2)}EE + \chi^{(3)}EEE + ...)$$

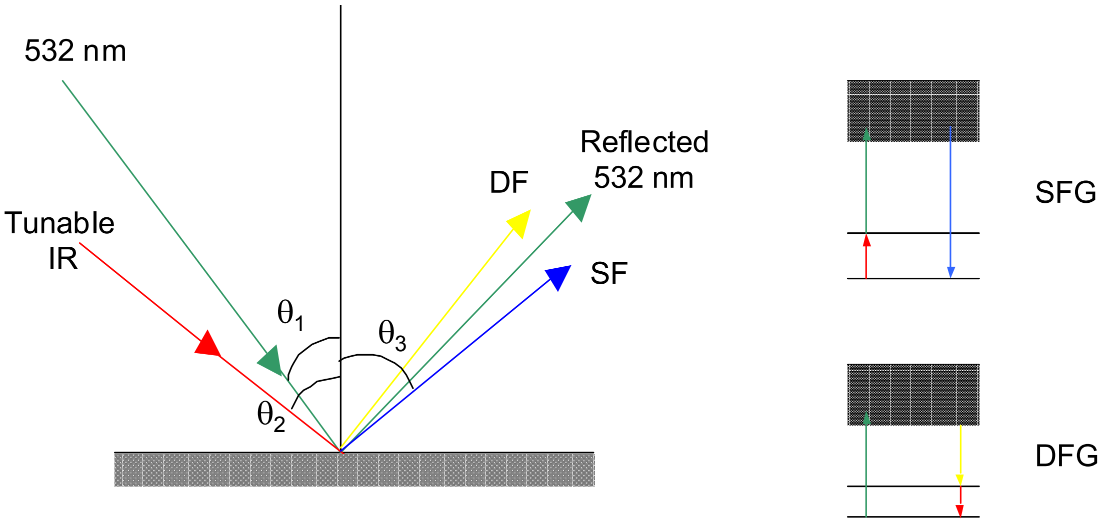

Figure 4.2 – Schematic of SFG and DFM, both of which occur at a given interface or in a noncentrosymmetric media.

As can be seen by equations 4.1 and 4.2, SFG probes the second order nonlinear susceptibility, $\chi^{(2)}$, of a material. The magnitude of the SF signal is proportional to the square of $P^{(2)}$, and therefore proportional to $|\chi^{(2)}|^2$, or the square of the second order nonlinear susceptibility. $\chi^{(2)}$ has both resonant, $\chi^{(2)}_R$, and nonresonant, $\chi^{(2)}_{NR}$, terms; therefore:

$$|\chi^{(2)}|^2 = |\chi^{(2)}_R + \chi^{(2)}_{NR}|^2 = \chi^{(2)}_R{}^2 + \chi^{(2)}_{NR}{}^2 + (\chi^{(2)}_R)(\chi^{(2)}_{NR}) \qquad (4.3)$$

$\chi^{(2)}_{NR}$ is material dependant and typically invariant to the IR electric field. However, it has been shown $\chi^{(2)}_{NR}$ can be affected by other fields, like the ones created in a material by applying an external potential [7] . While polymers have a very low $\chi^{(2)}_{NR}$, many metals have an electronic transition near the visible beam output that contributes significantly to the nonresonant signal, often referred to as the nonresonant background, seen in SFG spectra. It has been observed by this laboratory that the magnitude of the nonresonant background signal for a material follows as: polymers, fused quarts, CaF_2 < Pt, Rd < Cu, C <Au.

As a nonlinear susceptibility, $\chi^{(2)}$ is expected to be enhanced when either ω_{SF}, ω_{VIS}, or ω_{IR} approaches a molecular resonance. Typically, $\chi^{(2)}_R$ is defined as the IR resonant term:

$$\chi_R^{(2)} = \left| \sum_n \frac{A_R}{(\omega_{IR} - \omega_n - i\gamma_n)} \right| \qquad (4.4)$$

where A_R, ω_n, and γ_n are the strength, frequency and the damping constant of the nth resonance. By scanning the IR frequency, $\chi^{(2)}_R$ is enhanced when the IR frequency is in resonance with a vibrational mode of a molecule. A_R can be further described by,

$$A_R = \frac{1}{2\omega_n} \frac{\partial \mu}{\partial n} \frac{\partial \alpha}{\partial n} \qquad (4.5)$$

where μ is the dipole moment and α is the polarizibility of the molecule. Here one can be seen that for $\chi^{(2)}_R$ to be non-zero molecules must obey both IR and Raman selection rules. Although not discussed here, A_R is also proportional to the number and orientation average of the molecules at the interface.

By equation 4.3, depending on the size and sign of both the resonant and nonresonant terms, the SFG signal can appear as either a positive or negative going peak [8].

The surface specificity of SFG arises from the fact that under the electric dipole approximation, even-ordered nonlinear processes (i.e., $\chi^{(2)}$ and $\chi^{(4)}$, etc.) are necessarily zero in centrosymmetric media.

At any interface, where symmetry is necessarily broken and in non-centrosymmetic media (such as the crystals used to generate the tunable IR source discussed in section 4.3) $\chi^{(2)}$ is non-zero. To avoid any bulk $\chi^{(2)}$ contributions in SFG vibrational spectroscopy studies, systems contain samples and/or sample substrates that are centrosymmetric in the bulk.

$\chi^{(2)}$ is a third ranked tensor with 27 elements whose values are material dependant. When considering an isotropic surface, x = y, only four unique elements, of the 27, are non-vanishing; $\chi^{(2)}_{xxz}$ (or $\chi^{(2)}_{yyz}$), $\chi^{(2)}_{xzx}$, $\chi^{(2)}_{zzz}$, and $\chi^{(2)}_{zxx}$. By changing the polarization combination of the SF, IR and visible beams, all four of these individual tensor elements can be probed and orientation of the molecule with respect to surface normal can be determined. Two combinations of parallel (p) and perpendicular (s) polarized light, with respect to the surface, were used in the following studies: ssp and ppp where the polarizations represent the SF beam, the 532 beam and the IR beam, respectively. Because of the metal selection rule s-polarized light is canceled out by an image field from the electrons at the metal surface. Therefore, only the ppp polarization combination is used in SFG studies on metal surfaces.

4.3 Experimental Method

4.3.1 SFG Vibrational Spectroscopy Systems

Two different SFG systems have been used to collect data for studies presented in later chapters. Before getting into significant detail of each particular setup, the four basic components of a typical SFG system can be outlined.

As mentioned in the previous section, without strong electric fields, only linear processes will occur in a media. From the symmetry arguments mentioned above, the experimentalist gains surface specificity by probing the second-order nonlinear processes induced by two lasers. Therefore, the first necessary component to an SFG system is a pulsed laser for generating high power pulses of light that can be used to mix at an interface of interest.

In standard infrared-visible sum frequency generation (IR-VIS SFG), the two lasers used to mix on the surface are a 532nm visible beam and a tunable IR beam. To generated high power pulses of tunable IR light nonlinear optics are used. The second component in an IR-VIS SFG systems is a series of most often angle tuned nonlinear crystals that are used to both generate and amplify a 532 nm and a tunable IR lasers. This collection of optics, known more commonly as an optic parametric generation and amplification stage (OPG/OPA), varies slightly from system to system and will be discussed in more detail in future sections.

Thirdly, each SFG system has a series of optics used to guide the two laser beams onto a surface of interest and to insure overlap of the two beams in both time and space. Optics layouts vary widely from system to system depending on the types of surface studies to be carried out, for example, vacuum/solid, air/solid or liquid/solid interfaces. In general the path of the IR beam is minimized to prevent extensive absorption of photon by environmentally prevalent gasses such as H_2O and CO_2. The timing of the two lasers arriving at the interface of interest is controlled by delay stages, and the special overlapping of the two beams is control by highly reflective mirrors. In most SFG optics setups, the two lasers are brought to the surface at angles that maximize the total internal reflection coefficients, thereby optimizing collectible SF signal generated.

The final component of a standard SFG system is a detection system that involves collecting and amplifying the sum frequency signal generated at a studied surface/interface. Most often SFG signal is spatially separated from unconverted input photons, and guided with a few optics to a photon collection/amplification device such as a photomultiplier tube (PMT).

In the following studies, a pulsed Nd:YAG laser was used as a high powered photon source for both SFG systems. The YAG laser delivers about 20 picosecond wide pulses at 20 hertz. The power output of the fundamental 1064 nm laser beam was approximately 35 watts or about 50 mJ per pulse. It is not the focus of this work to give a detailed description of a pulsed Nd:YAG; however, a very detailed and informative description of how a pulsed YAG laser works can be found in literature [9].

In both SFG systems the 1064 nm beam is split in two, whereby one portion is immediately doubled to 532nm (visible light) and the other portion is time delayed for future mixing to obtain the tunable IR laser beam. Figures 4.3 shows one of the two different OPG/OPA setup used in the studies discussed in Chapters 5, 6 and 7.

The first setup is a commercially designed system by LaserVision, Figure 4.3. IR light can be generated from 1000cm^{-1} to 4000cm^{-1} and ranges from 100μJ to 400μJ per pulse. 532 nm light has been measured at 1mJ per pulse. Briefly, the 1064nm fundamental from the YAG laser is split in two. The first portion is passed thru a KTP crystal and doubled to 532 nm. The 532 nm beam is split into two portions with one being sent to the sample for the SFG experiment and the second being sent to two counter-rotating KTP crystals. The 532 nm beam is passed both forwards and backwards thru the angle tuned crystals to generate and amplify both a near IR beam from 720 to 870nm and a 1.25 to 2.12 μm beam. The 1.25 to 2.12 μm beam is then sent to two counter rotating KTA crystals where it is mixed with the second portion of the 1064nm fundamental. By DFM of the 1064nm and 1.25 to 2.12 μm light in the angle tuned KTA crystals, mid IR light from 5 to 2 μm, or 2000 to 4000cm^{-1}, is generated. With the insertion of the $AsGaSe_2$ crystal IR light from 10 to 5 μm, or 1000 to 2000 cm^{-1}, can be generated via DFM with the pump (1.25 to 2.12 μm) and seed (2.12 to 5 μm) beams coming out of the KTA stage.

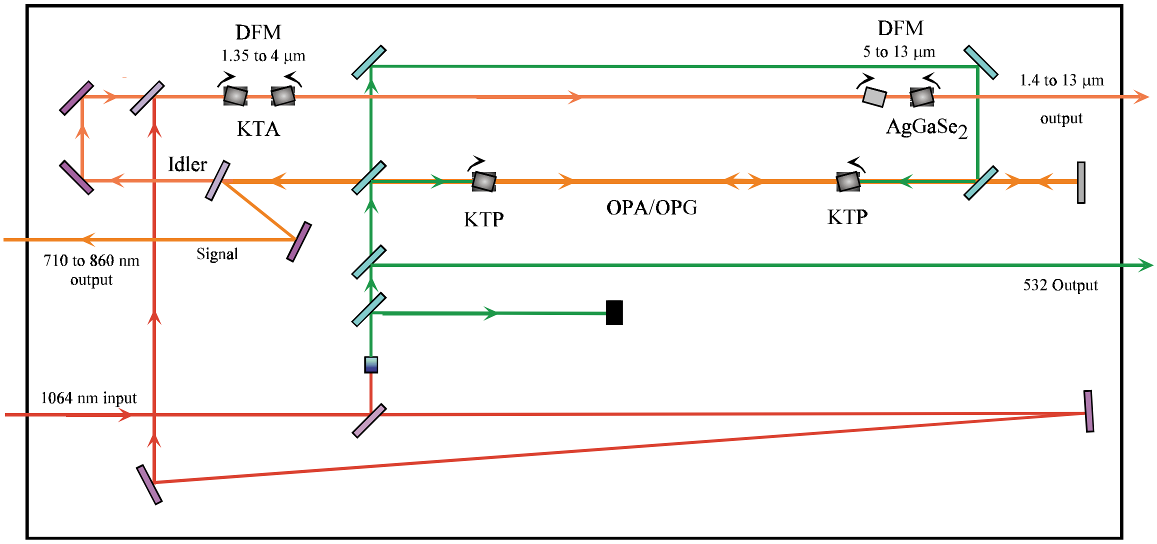

Figure 4.3 – LaserVision OPG/OPA Optical Layout

In the second SFG set-up, tunable mid-infrared light from 1300-4000 cm $^{-1}$ is generated using a similar optical arrangement. The 532nm beam is split into two portions with one being sent to the sample for the SFG experiment and the second being sent to two counter-rotating barium borate (BBO) crystals which serve as an OPG/OPA stage. The 532 nm beam is passed both forwards and backwards thru the angle tuned crystals to generate and amplify both a near IR beam from 720 to 870nm and a far IR (less than 2μm) beam. The far IR beam is then directed to a grating to narrow the bandwidth. By DFM of the 1064nm and far IR light in the angle tuned BBO crystals, mid IR light from 4.5 to 2 μm, or 2200 to 4000cm^{-1}, is generated. By removing the $LiNbO_3$ crystal and inserting the $AsGaS_2$ crystal IR light from 7 to 4 μm or 1300 to 2300 cm^{-1}, can be generated via DFM from mixing the 1064nm fundamental beam and the seed beam coming out of the BBO stage.

Regardless of the OPG/OPA optics setup the resolution of the SFG systems is ~7 cm^{-1}. This resolution is limited by the angle tuning of the nonlinear crystals used in the OPG/OPA.

The optics layouts guiding the two lasers to the samples are very similar. Considering geometric constraints of the experiment, as few mirrors as possible are used to guide the IR and 532 nm light to the sample.

Briefly, the IR beam is passed thru a $\lambda/2$ waveplate that serves as a power control. To change the polarization of the p-polarized IR beam a CaF waveplate and Si polarizer can be inserted into the IR beam path. Just before the sample stage the IR light is sent thru a lens to focus the beam onto the sample. The 532 beam is also passed thru a $\lambda/2$ waveplate that serves as a power control, and then through a polarizer so that the desired polarization can be selected. To aid in the temporal overlap of the two lasers, the 532 nm beam is then sent to a delay stage with a few centimeters of translational movement. In some cases a telescope has been used to change the overall size of the 532 nm beam before it is directed to sample surface. In both SFG systems the 532 nm beam is approximately 4 times larger than the IR beam to aid in the spatial overlap.

The collected SF signal, in both of the mentioned systems, is spatially separated from the un-converted 532nm light using a dielectric mirror. The SF signal is then passed through a polarizer so that the desired SF polarization can be selected. The SF is then passed through two slit filters to ensure no scattered 532nm light is collected. Finally, the SF signal is focused unto the slit of a monochrometer set to allow only the correct calculable SF signal to pass. SF photon are then collected and amplified in a photomutliplier tube connected to a gated integrator and photon counting system.

4.3.2 SFG Signal Collection and Analysis

Experiments discussed in following section were performed in either the ppp polarization combination (p-polarized SF, p-polarized visible, and p-polarized infrared) or the ssp combination.

SFG spectra presented are an average of 3 to 10 scans with 5 cm^{-1} resolution. SFG signal was collected for 1 to 10 seconds at every 5 cm^{-1} interval.

To obtain proper resonance peak position, the normalized sum frequency signal, I_{SFG}, was fitted to equation 2 [5].

$$I_{SFG} = \left| A_{NR} + \sum_{n} \frac{A_R}{(\omega - \omega_n - i\gamma)} \right|^2 \qquad (4.6)$$

where A_{NR} is the non-resonant contribution, ω_n is the n-th resonant vibrational frequency, γ is the linewidth and A_R is the resonant strength. The resonant strength is proportional to the number and orientation average of the molecules at the interface of interest as well as their infrared and Raman transition moments.

4.3.2.1 Sum Frequency Signal Normalization

SFG signal collected from the liquid/solid interface is normalized with respect to the reflected IR beam, equation 4.7, from the electrode to ensure that no false SFG peaks were observed due to strong IR absorption by the thin film of electrolyte above the electrode surface. The normalization procedure is as follows:

$$SFG_{norm} = \frac{SFG_{ave}}{IR_{ave} / IR_{max}} \tag{4.7}$$

where SFG_{norm} is the normalized SFG intensity, SFG_{ave} is the average SFG intensity from 3 to 5 scans, IR_{ave} is the average of the reflected IR intensity and IR_{max} is the maximum IR intensity reflected from the electrode surface.

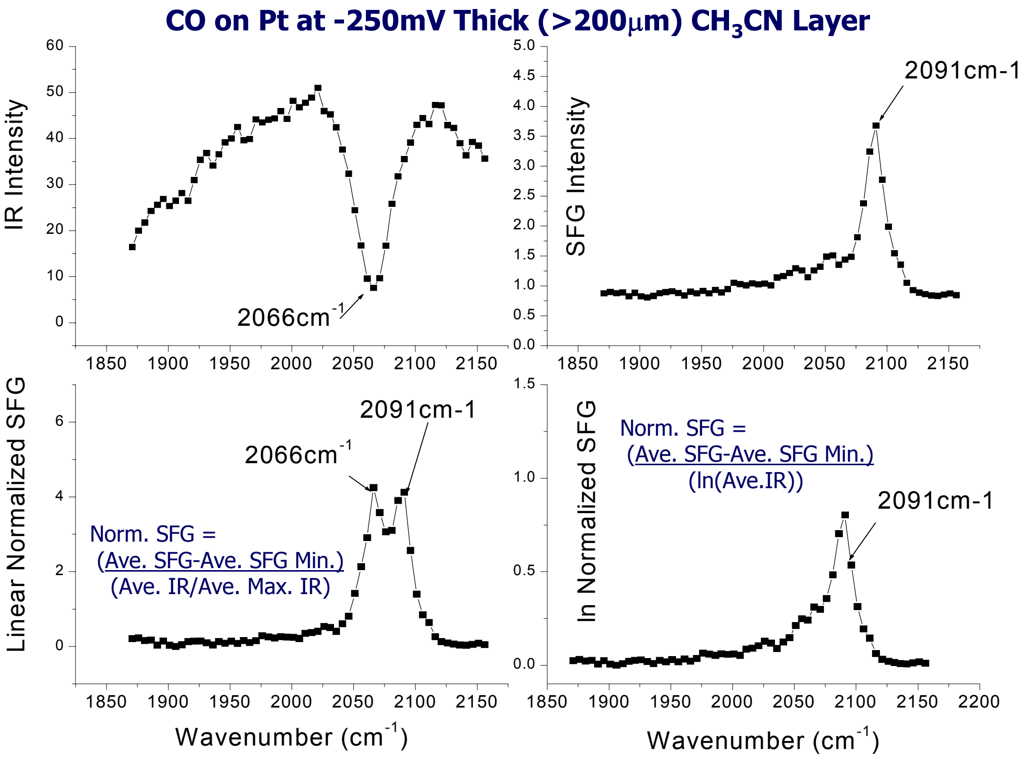

Figure 4.4 – Examples two normalization methods: lower left) for strong IR absorption linear normalization gives false looking peaks in spectra while, lower right) ln normalization does not.

SFG signal collected from the solid/air interface is normalized with respect to the intensity of the input IR beam to compensate for any SF signal difference arising from power fluctuations in the laser and intensity difference in the IR beam dependant on the non-linear crystal efficiency.

4.3.3 Sample preparation

Sample preparation techniques are discussed separately in the following chapters.

4.4 Complimentary Techniques

As with any scientific study, performing complimentary studies on the same system using other appropriate techniques validates the results obtained. For the SFG studies described in Chapter 5-7, several other surface and bulk studies were performed to compliment surface vibrational spectra collected using SFG. These additional data provide supporting evidence for experimental conclusions.

4.4.1 Cyclic Voltammetry (CV)

Cyclic voltammetry is one of the most simple, versatile techniques used by electrochemists today [11,12,13]. In tandem with surface spectroscopy studies, CV can provide information on electro-active species at an electrode interface. The main application of CV is to quickly observe the redox behavior of a system over a large potential range.

While the art of CV has many applications and a great deal of information can be gleamed for a simple voltammogram, the author used CV for three relatively simple purposes 1) to determine the cleanliness of working electrodes, 2) to estimate the potential at which chemical reactions occur at the electrode surface and 3) to fingerprint certain chemical changes occurring at the electrode/electrolyte interface. A typical CV experimental set-up is shown in Figure 4.5. Basically CV involves linearly ramping the voltage of a working electrode with respect to a reference electrode and measuring the current generated at the working electrode interface. In the following experiments a bi-potentiostat was used to generated the voltage ramp and convert the generated current into a voltage reading. The voltage ramp and the converted current were easily recorded using an X-Y chart recorder.

In this particular set-up a three-electrode electrochemical cell is being used. The working electrode voltage is applied with respect to a reference electrode, either Pd, which mimics the normal hydrogen electrode, or a saturated calomel electrode (SCE). A third electrode, known as the counter electrode is held at the same voltage as the reference electrode, but because of its lower resistance any current generated in the electrochemical cell is drained away. This allows the ref/working electrode voltage difference to remain unchanged by any current flow in the cell. To clarify data in the following chapters, for positive going scans, or the top half of any voltammograms, current shown is generated from oxidation reactions occurring at the working electrode interface. Negative going scans, or the bottom half of any voltammograms, show features from any reduction reactions occurring at the working electrode surface.

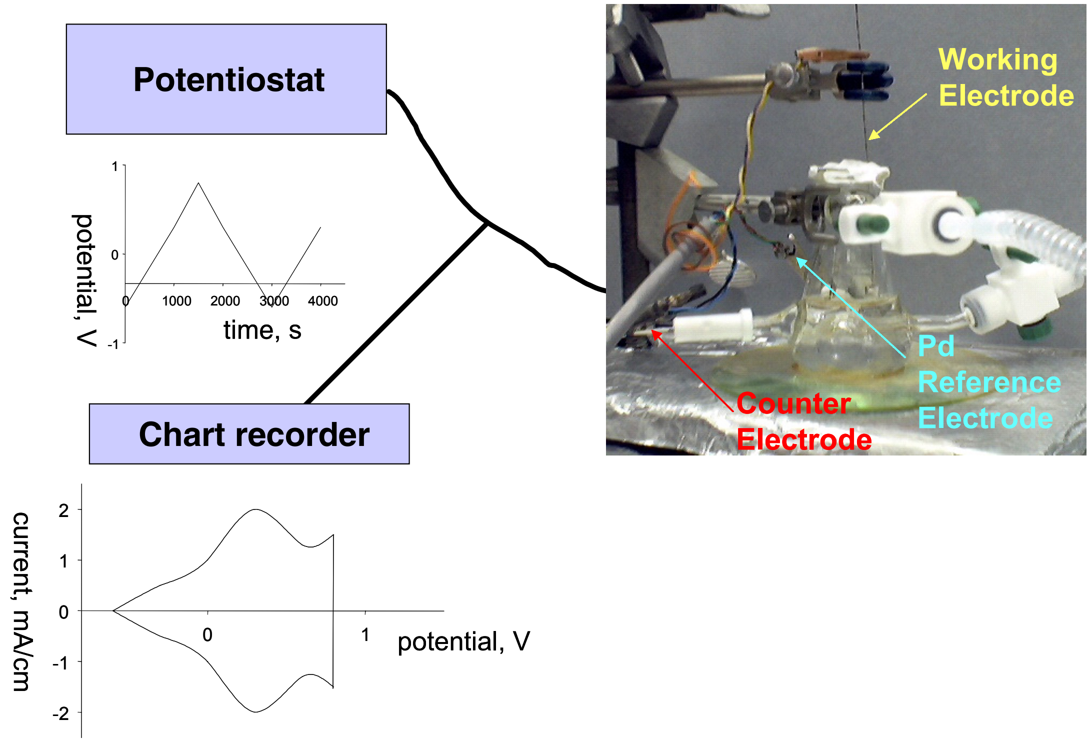

Figure 4.5 – Schematic of Cyclic Voltammetry System.

As shown by equation 4.8, the voltammetry features are dependent on the voltage scan rate, the size of the electrode, the analyte concentration and the diffusion coefficient. As is common practice in CV, the analyte is not stirred during voltammetry. Thorough research has been done on CV in identifying Pt crystallinity [14], and the distinct voltammogram features of poly crystalline Pt can be used to determine the cleanliness of the electrode before performing any spectroscopic studies.

$$\underset{\text{current}}{i_p} \propto \overset{\text{\# of electrons}}{n^{3/2}}\underset{\text{electrode area, analyte concentration, diffusion coefficient}}{ACD^{1/2}}\overset{\text{scan rate}}{v^{1/2}} \qquad (4.8)$$

In order to perform SFG experiments where an electrode and electrolyte could be under potential control, a spectro-electrochemical cell had to be designed. As shown in Figure 4.6, a glass cell with an IR transparent window, CaF or fused quartz, is equipped with the previously discussed three electrode setup. The working electrode is encased in a Kelaf shaft that can be manually pushed towards (or away from) the IR transparent window creating a thin film of electrolyte of ~10 μm thick between the window and working electrode. Experiments performed with these thin electrolyte films absorbed less that 20% of the incoming IR light used in mixing for SFG.

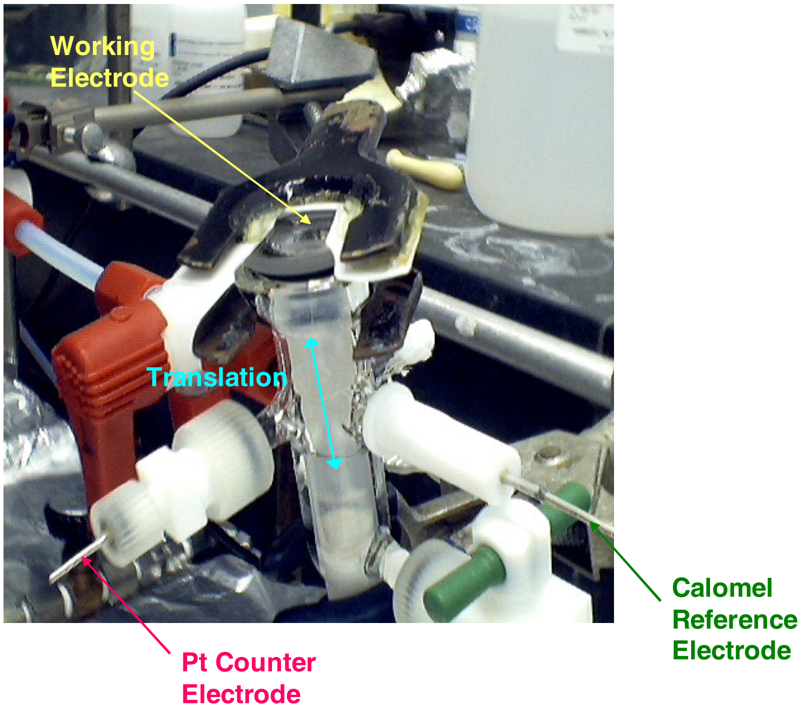

Figure 4.6 – Spectroelectrochemical Cell used in Electrochemical SFG experiments.

4.4.2 X-ray Photoelectron Spectroscopy (XPS)

XPS is a core level electron spectroscopy generally used for surface elemental analysis and the determination of the surface atom oxidation state. Because XPS is an electron based technique it can only be performed in UHV conditions, i.e. $<10^{-9}$ torr. Unlike SFG, XPS is insensitive to the molecular orientation of the surface atoms/molecule and therefore can be used to determine if SFG signal intensity changes can be attributed to concentration changes alone. While SFG has submonolayer sensitivity, the electron escape depth and the x-ray penetration depth make XPS a less surface sensitive technique (SFG <10% of a monolayer, XPS ~ 10 μm is define as the surface).

In XPS, a sample is irradiated with nearly monochromatic soft X-rays and the kinetic energy of the emitted core electrons is measured. A simplified depiction of the XPS process is shown in Figure 4.7. An X-ray of energy $h\nu$ ejects a carbon 1s electron. The emitted electron has a kinetic energy, KE_1, which can be measured by an electron energy analyzer. XPS spectra are given as plots of intensity versus binding energy (BE). The binding energy of the photoelectrons is characteristic of the atomic orbital from which the electron originated. Therefore, the BE will provide the identity of the atoms present in the analysis volume.

In Koopman’s approximation, the binding energy (BE) of the photoelectron is related to the measured kinetic energy as follows:

$$BE = h\nu - KE_{meas} - \Phi_s \tag{4.9}$$

where $h\nu$ is the energy of the soft x-ray, KE_{meas} is the kinetic energy of the emitted photoelectron as measured by the spectrometer, and Φ_s is the work function of the spectrometer.

Quantitative determination of the surface atomic concentration is accomplished by correcting the calculated peak area by a sensitivity factor specific to each element as follows [15]:

$$C_i = \frac{\frac{A_i}{S_i}}{\sum_{j=1}^{i} \frac{A_j}{S_j}} \tag{4.10}$$

where C_i is the concentration of species i, S_i is the sensitivity factor of species i, and the summation is over all species present in the XPS spectrum. For further details about XPS the reader is guided to several good reviews [15, 16].

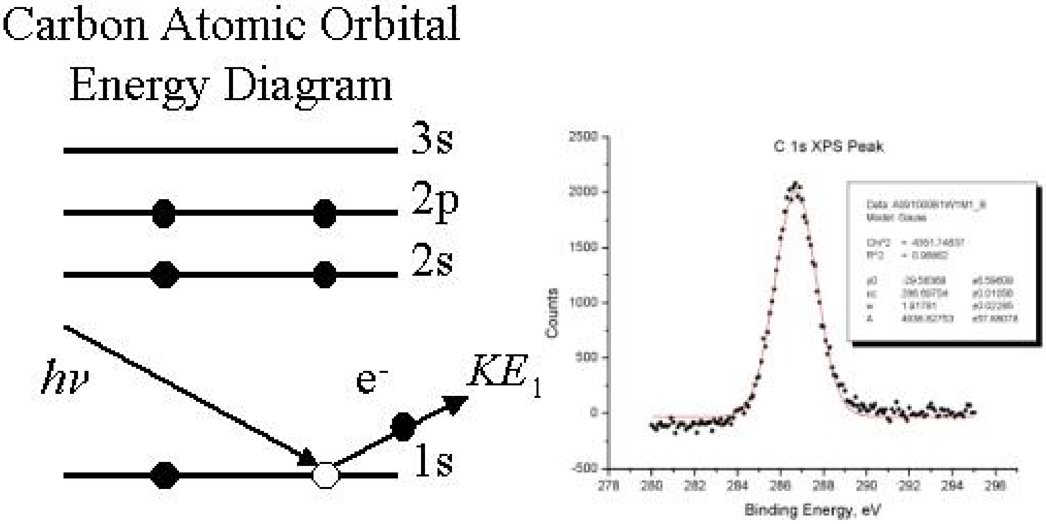

Figure 4.7 – Schematic of XPS process.

4.4.3 Atomic Force Microscopy (AFM)

Atomic Force Microscopy (AFM) involves the interaction of a small probe with a surface and is used in our lab to image the microscopic features of surfaces. AFM provides real space images of a material surface and shows contrast for areas with different morphology. A commercial Park Scientific M5 AFM with a large range scanner was used to collect topographic and friction images of ~900 square micron areas of samples in contact mode. Commercial silicon cantilevers with tungsten carbide coated tips from NT-MDT were used with this instrument. Further details about the AFM technique can be found in review articles about surface microscopy techniques [17].

4.4.4 Fourier Transform Infrared Spectroscopy (FTIR)

In contrast to SFG, FTIR spectroscopy provides information about bulk, not surface, molecular vibrations. By absorbing photons in the mid-infrared frequency region ($100cm^{-1}$ to $4000cm^{-1}$) molecular vibrations from metal-hydrogen to oxygen-hydrogen bond can be excited. By providing information on the types of bonds present in a material, IR spectroscopy gives detailed structural data about molecules.

The relative distance between atoms in molecules is constantly fluctuating around an ideal length via vibrations. By considering a diatomic molecule as two vibrating masses connected by a spring, one can describe the vibration between the two masses as a simple harmonic oscillator. The energy of the vibration is continually and periodically changing from potential to kinetic energy. The total amount of energy, E, is proportional to the frequency, ν, of the vibration:

$$E \sim h\,\nu \qquad (4.11)$$

where h is Plank's constant. The natural frequency, ν, of the diatomic molecule's vibration is determined by the force constant (or bond strength), K, and is inversely proportional to the mass of the two bonded atoms:

$$\nu = 1/(2\pi c)\,(K/\mu)^{1/2} \qquad (4.12)$$

where c is the speed of light and μ is the reduced mass which is given by:

$$\mu = m_1m_2/m_1+m_2 \qquad (4.13)$$

where m_1 and m_2 are the masses of the two atoms, respectively.

IR spectroscopy involves an adsorption process. In an adsorption process, IR radiation with the matching frequency to a natural vibration of a molecule is absorbed. This absorbed energy is used to increase the amplitude of that particular vibrational mode for a given molecular bond. However, only molecular bonds with a dipole moment can be excited by IR radiation. Consequently, traditional IR spectroscopy provides a large amount of information about the non-symmetric bonds present, and therefore the structure of a given material. By using polarization techniques, surface sensitivity and molecular orientation can also be gained in linear IR spectroscopy studies. However, to attain surface sensitivity comparable to SFG spectroscopy, a reference spectrum is necessary for signal normalization.

In addition to providing contrasting bulk vibrational data to SFG surface vibrational data, IR spectroscopy studies are an ideal way to determine whether or not the dipole moment of a particular molecular bond is large enough to generate a strong signal in SFG surface spectroscopy studies. Unlike IR spectroscopy, for a molecule to be SFG active both a strong dipole moment and a large polarization cross section are required. IR spectroscopy therefore probes more molecular bonds in any given IR frequency range than SFG.

4.5 References

1. Baldelli, S., Markovic, N., Ross, P.N., Shen, Y.R., Somorjai. G.A., *J. Phys. Chem. B*, **103**, (1999), p. 8920.

2. Baldelli, S., Schnitzer C., Campbell, D.J., Shultz, M.J., *J. Phys. Chem. B.*, **101**, (1997), p. 10435.

3. Bain, C.D. *J. Chem Soc., Faraday Trans.*, **91**, (1995), p. 1281.

4. Du, Q., Superfine, R., Freysz, E., Shen, Y.R., *Phys. Rev. Lett.*, **70**, (1993), p. 2313.

5. Y. R. Shen, *Nature*, **337**, (1989), p. 519.

6. J.Y. Huang and Y.R. Shen, *Laser Spectroscopy and Photochemistry on Metal Surfaces*, World Scientific, Singapore, (1995), p.5.

7. A. Tadjeddine and A. LeRille, *Interfacial Electrochemistry,* Marcel Dekker, Inc., New York, NY, (1999), pp. 317-343.

8. P.B. Miranda and Y.R. Shen, *J. Phys. Chem. B.*, **103**, (1999), pp. 3292-3307.

9. C.C. Davis, *Laser and Electro-Optics*, Cambridge University Press, 1996.

10. Huang, J., Korzeniewski, C., *J. Electroanal. Chem.,* **471**, (1999), p. 146.

11. Bard, A.J., Faulkner, L.R., *Electrochemical Methods*, Wiley & Sons, New York (2001).

12. P.T. Kissinger and W.R. Heineman, J. of Chem. Ed., 60 (9), (1983), pp. 702-706.

13. D.H. Evans, K. M. O'Connell, R.A. Petersen, M.J. Kelly, J. of Chem. Ed., 60 (4), (1983), pp. 290-293.

14. Clavilier, J., *Interfacial Electrochemistry,* Marcel Dekker, Inc., New York, NY, (1999), pp., pp231-248

15. J.F. Moulder, W.F. Stickle, P.E. Sobol and K.D. Bomben, *Handbook of X-ray Photoelectron Spectroscopy*, Physical Electronics, Inc., Eden Prairie, MN, (1995).

16. D.P. Woodruff and T.A. Delchar, *Modern Techniques of Surface Science* (2nd ed.), Cambridge University Press (1994).

17. R.J. Hamers, *J. Phys. Chem*, **100** (31), (1996), pp. 13103-13120.

18. P. W. Atkins, *Physical Chemistry*, W H Freeman & Co., New York, NY, (1997)

Chapter 5

Sum Frequency Generation Spectroscopy Studies of Polyetherurathane-Silicone Block Co-polymers

5.1 Introduction

Tailoring bulk properties of polymers such as glass transition temperature and elastic modulus is important in designing biocompatible materials. As opposed to polymer blends, co-polymer bulk properties can be specifically modified while minimizing phase separation. In general, the bulk composition of a polymer governs its mechanical properties, while the surface composition dominates its interaction with biological systems. Polyetherurathanes have the desirable mechanical properties; however, the addition of polydimethylsiloxane (PDMS) creates softer and more flexible materials that also show improved biocompatibility over non-silicone containing materials. However, PDMS itself is too viscous and also too adherent to be the major component in a biopolymer. Polyetherurethanes-silicone co-polymers, with 0% to 60% silicone (PDMS by weight), were studied using several surface specific techniques to confirm that increasing the PDMS groups enhanced the polymer surface biocompatibility, while leaving the bulk mechanical properties relatively unchanged.

5.2 Experimental Details

5.2.1 Preparation of Polymer Samples

Polyetherurethanes-silicone co-polymers containing 10 to 60% silicone by weight were designed and synthesized by The Polymer Technology Group of Berkeley, California. Figure 5.1 shows the molecular structures of Elastane®, a polyetherurethane without silicone, and Purasil®, an Elastane®- PDMS co-polymer.

Co-polymers were received in pellet form. Co-polymer solutions of 2 to 10% by weight were made with *N*-dimethylacetamide (DMAC), an effective solvent for these co-polymers. Co-polymers were allowed to dissolve for up to 3 days, sometimes at 65°C, to ensure a consistent polymer solution. Visible signs of co-polymer oxidation, such as a yellowing of the polymer solution, were noted and fresh polymer solutions were made for surface studies.

Polymer films for spectroscopy and microscopy studies were made either by solvent casting or spin casting techniques. In solvent casting, polymer solutions were deposited on a clean 1" fused quartz or CaF windows. The substrates were then transferred to an oven and the DMAC solvent was evaporated away at 65°C for 24 hours. In spin casting, co-polymer solutions were deposited onto clean 1" fused quartz or CaF windows and then spun for 300 seconds on a P-6000 Specialty Coating Systems Spin Coater. In most cases, spin-coated samples were also placed in an oven for 24 hours at 65°C to ensure all solvent was removed.

5.2.2 Sum Frequency Generation Studies

Details of the optical setup for the SFG experiment have been described previously [1]. Tunable mid-infrared light (2000-4000 cm $^{-1}$) was generated by difference frequency mixing tunable near-infrared light with the fundamental beam of the

Nd:YAG pump laser in angle tuned KTA stage crystal. The infrared and visible beams were incident on the liquid/solid interface at 55^o and 50^o and have energy of 50 to 400 μJ and 1 mJ, respectively. All experiments were done with the ssp-polarization combination (s-polarized SF, s-polarized visible, and p-polarized infrared). SFG spectra presented herein are an average of 3 to 5 scans. SFG signal was collected for 1 to 5 seconds, i.e. 20 to 100 shots, at every 5 cm^{-1} interval.

5.3 Results and Discussion

5.3.1 FTIR Data and Analysis

IR spectra were obtained using a standard FTIR spectrometer located at the Polymer Technology Group in Berkeley, California. Spectra presented are an average of three scans with 0.5 cm^{-1} resolution. Since FTIR is not a surface sensitive technique and therefore provides vibrational information about the bulk co-polymers, these data provide information on the bulk mechanical properties only[2].

FTIR spectra of biopolymers containing 0 to 60% by weight PDMS are shown in Figure 5.2. Spectra from co-polymer samples containing less than 37% PDMS have two distinct vibrational bands at 2875 and 2950cm^{-1} which are attributed to CH_2 symmetric and anti-symmetric vibrational bands from the more hydrophobic component Elastane®. Collected FTIR data indicates that the co-polymer sample with less than 37% PDMS have bulk mechanical properties more like Elastane®, the polyetherurethane component, than the PDMS component. As mentioned before, while silicone makes a polymer more biocompatible, PDMS itself is too viscous to be the major component in a biopolymer. It is therefore desirable to have as little PDMS in the bulk polymer as possible while maximizing its surface concentration.

The 37% PDMS sample shows the Si-CH_3 stretches at 2920cm^{-1} and 2975cm^{-1} beginning to increase in size and at 60% on PDMS in the bulk, the IR spectra is dominated by the Si-CH_3 vibrational features. FTIR results for co-polymer samples containing greater than 37% silicone suggest that the bulk mechanical properties are dominated by those of PDMS and therefore such co-polymers would not be ideal for implant use.

5.3.2 Sum Frequency Generation Data and Analysis

5.3.2.1 Co-polymers Exposed to Air

In contrast to FTIR, SFG data is surface specific. As shown in Figure 5.3, surface vibrational spectra obtained by SFG are identical for the co-polymers containing 10 to 60% PDMS. These data are a clear indication that the surface has been saturated with the more surface active, i.e. lower surface free energy, silicone component at even the lowest concentrations of PDMS in the bulk. Similar to the FTIR data, SFG spectra show three distinct peaks at 2875, 2920, and 2950cm^{-1}. As indicated in Figure 5.3 these spectral features are attributed to the CH_2 symmetric vibration from the Elastane® component, the symmetric vibration from the CH_3 of the PDMS group, and finally the overlapping CH_2 - CH_3 antisymmetric vibrational bands and fermi resonances, respectively. In contrast to previous studies done by this laboratory [2, 3, 4], both the hydrophobic and hydrophilic components are seen in the SFG spectra. As seen in Figure 5.4, when PDMS is added to the biopolymer as a surface modifying end group, the SFG spectra contain only the PDMS vibrational bands. This further segregation of the surface is most likely due to the larger freedom of motion of the PDMS end group in comparison to that of the PDMS present in the backbone of the polymer.

For the Elastane®/Purasil® polymers, a comparison of the ratio of the PDMS symmetric CH_3 vibrational band to the CH_2 symmetric vibrational band from the polyetherurethane component is shown in Figure 5.5. This data suggest that the surface of the polymers is saturated with silicone containing groups after only 10% PDMS has been added to the backbone of the co-polymer.

5.3.2.2 Co-polymers Exposed to Water

Since Purasil® contains both hydrophobic (PDMS) and hydrophilic (ether and urethane segments) components, its surface structures may be expected to differ in water from in air. SFG spectra of the co-polymer blends after exposure to water show that the surfaces of the blends are indeed environmentally sensitive. The degree of restructuring, however, depends on the relative surface energies of the two components and their freedom of motion.

As shown in Figure 5.6, SFG spectra of polyetherurethanes-silicone co-polymers in contact with water for 4 days differ from those spectra taken from their drycounterparts. The decrease in the anti-symmetric CH_2 and CH_3 stretches at 2975cm^{-1} indicates that the CH groups are aligned more perpendicular to the polymer surface normal. The effect is most likely due to a reorientation of the CH groups to lower surface free energy by maximizing hydrogen bonding at the polymer/water interface.

The surface restructuring observed for these co-polymers is significantly less than that previously observed for polymer blends and polymer with surface modifying end groups [2, 3, 4]. However, this difference can be explained by the fewer degrees of freedom in motion for the individual polymer components in these co-polymers.

5.3.3 X-Ray Photoelectron Spectroscopy (XPS) and Contact Angle Studies

XPS measurements were taken on a Perkin-Elmer PHI 5300 XPS spectrometer with a position sensitive detector and a hemispherical energy analyzer. As shown in Figure 5.7a, the ratio of the Si to C peaks observed in XPS spectra agrees with the SFG results, which suggests the polymer surface was saturated with silicone after only 10% PDMS by weight was added.

5.3.4 Atomic Force Microscopy (AFM) Studies

A commercial Park Scientific M5 AFM with a large range scanner was used to collect topographic and friction (not shown) images of ~900 square micron areas of co-polymers in ambient conditions. Commercial silicone cantilevers with tungsten carbide coated tips from NT-MDT were used with this instrument. AFM provides real space images of a polymer surfaces and shows contrast for areas with different morphology or composition/elasticity.

AFM images of the polyetherurethane-silicone co-polymers, Figure 5.4, indicate that the surfaces are relatively flat for samples containing less than 60% silicone by weight. For co-polymer samples containing 60% silicone, AFM images indicate a surface dominated by large 2-5 micron wide hills. Finally, AFM images show that polymer surfaces with silicone containing end groups exhibit 1 to 5 micron sized holes, making these materials non-ideal for bioapplications.

5.4 Summary and Conclusions

Previous SFG studies of biopolymers show that low concentrations (~ 2%) of silicone end groups can completely cover the polymer surface [4, 5]. However, AFM images show that polymer surfaces with silicone end groups exhibit 1 to 5 micron holes, making these materials non-ideal for bioapplications.

SFG studies on the polyetherurethane-silicone co-polymer/air interface indicate that the surface concentration of silicone does not increase linearly with the bulk silicone concentration. Rather, surface spectroscopy results from both SFG and XPS suggest that surfaces of the co-polymers containing greater than 10% PDMS by weight were all silicone saturated.

FTIR spectra indicate that the bulk spectra, and therefore bulk mechanical properties, change significantly after silicone is more than 37 % of the total polymer weight. Finally, AFM images of the polyetherurethane-silicone co-polymers indicate that surfaces are relatively flat for samples containing less than 60% silicone by weight.

Further SFG studies of these co-polymers in aqueous environments were performed to monitor the polymer surfaces in more relevant conditions. Co-polymer exposed to water for four days showed minor reconstruction as compared to polymer blends and polymer with surface modifying endgroups. All surface studies performed indicate that silicone-containing co-polymers are well suited for bioimplant materials and warrant further study.

5.5 References

1. A. Opdahl, R.A. Phillips, and G.A. Somorjai, *Macromolecules*, **35**, (2002), pp. 4387-4396.

2. D. Zhang, D.H. Gracias, R. Ward, M. Gauckler, Y.R. Shen, G.A. Somorjai, *J. Phys. Chem. B*, **101**, (1998), pp. 6225-6230.

3. Z. Chen, R. Ward, Y. Tian, S. Baldelli, A. Opdahl, Y.R. Shen and G.A. Somorjai, *J. Am. Chem. Soc.*, **122**, (2000), pp. 10615-10620.

4. A. Ophahl, S. Hoffer, B. Mailhot and G.A. Somorjai, *The Chemical Record*, **1**(no. 2), (2001), pp. 101-122.

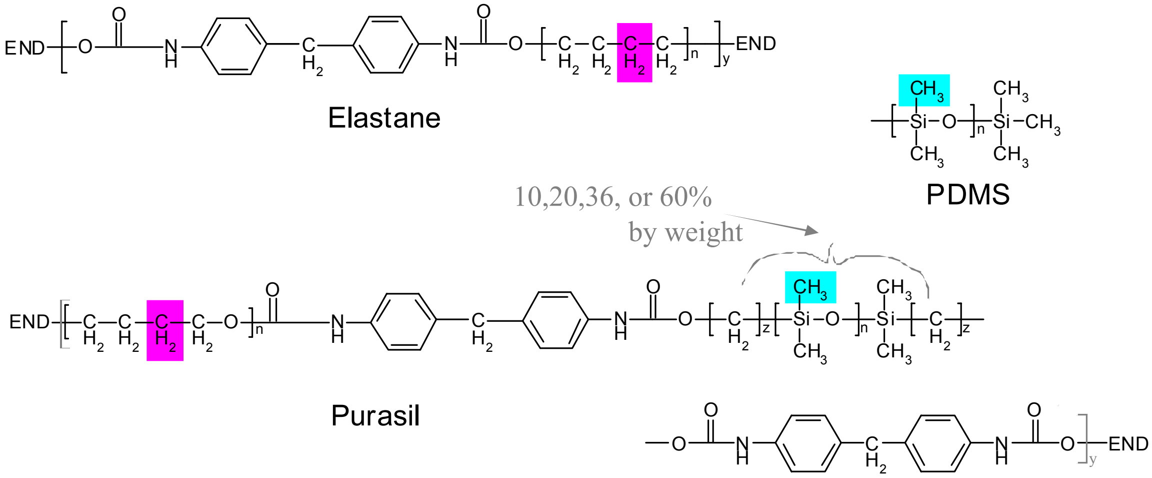

Figure 5.1 – Molecular Structure of Polyetherurathane-Silicone Co-polymer. CH_2 groups from polyetherurethane backbone observed in SFG spectra are highlighted in blue and from silicone CH_3 groups in pink.

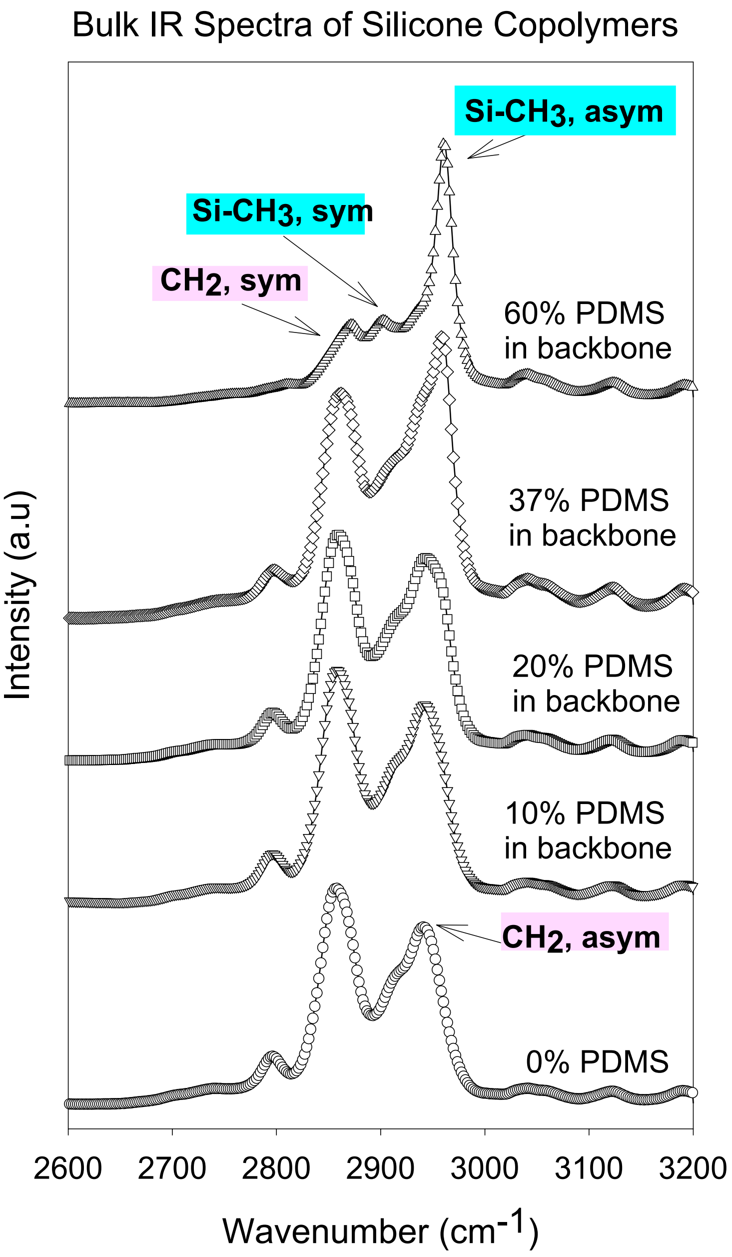

Figure 5.2 – Bulk IR spectra of Polyetherurathane-Silicone Co-polymers. CH_2 vibrational bands from polyetherurethane backbone are highlighted in blue and silicone CH_3 vibrational bands in pink.

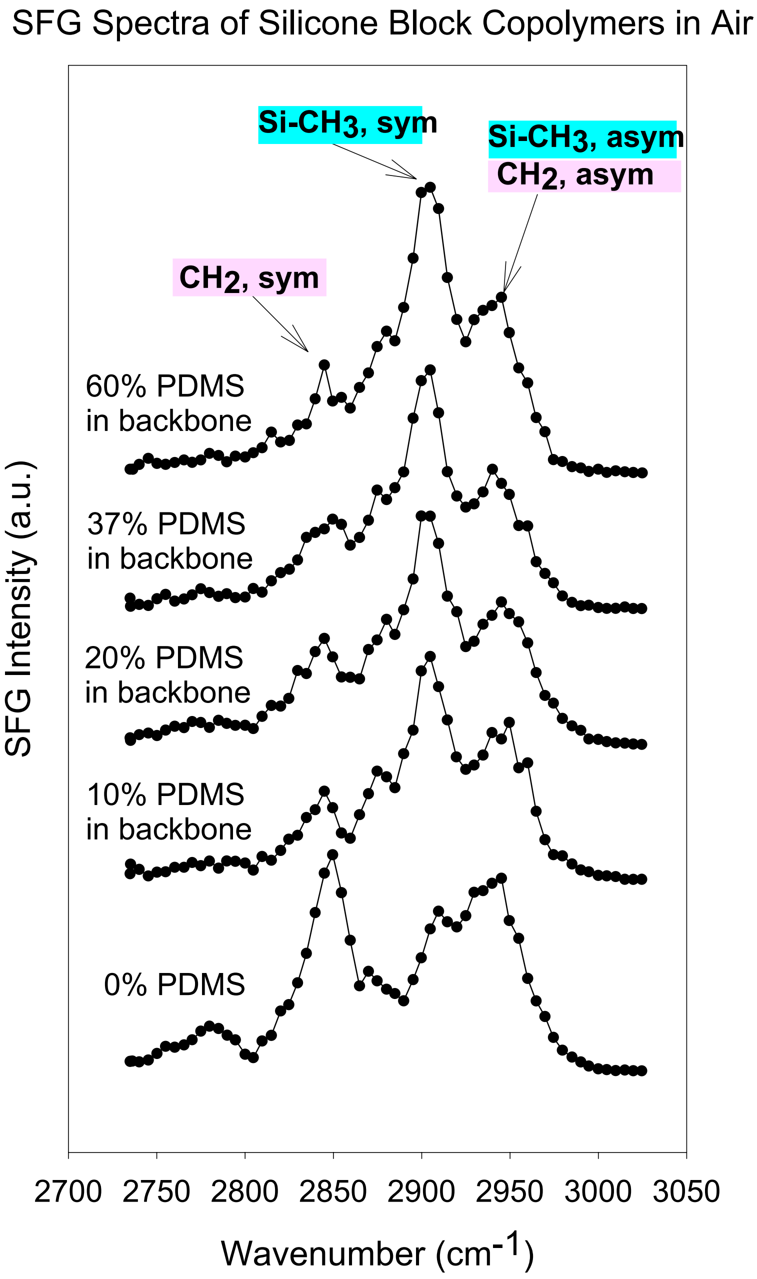

Figure 5.3 – SFG spectra of Polyetherurathane-Silicone co-polymers in air. CH_2 vibrational bands from polyetherurethane backbone are highlighted in blue and silicone CH_3 vibrational bands in pink.

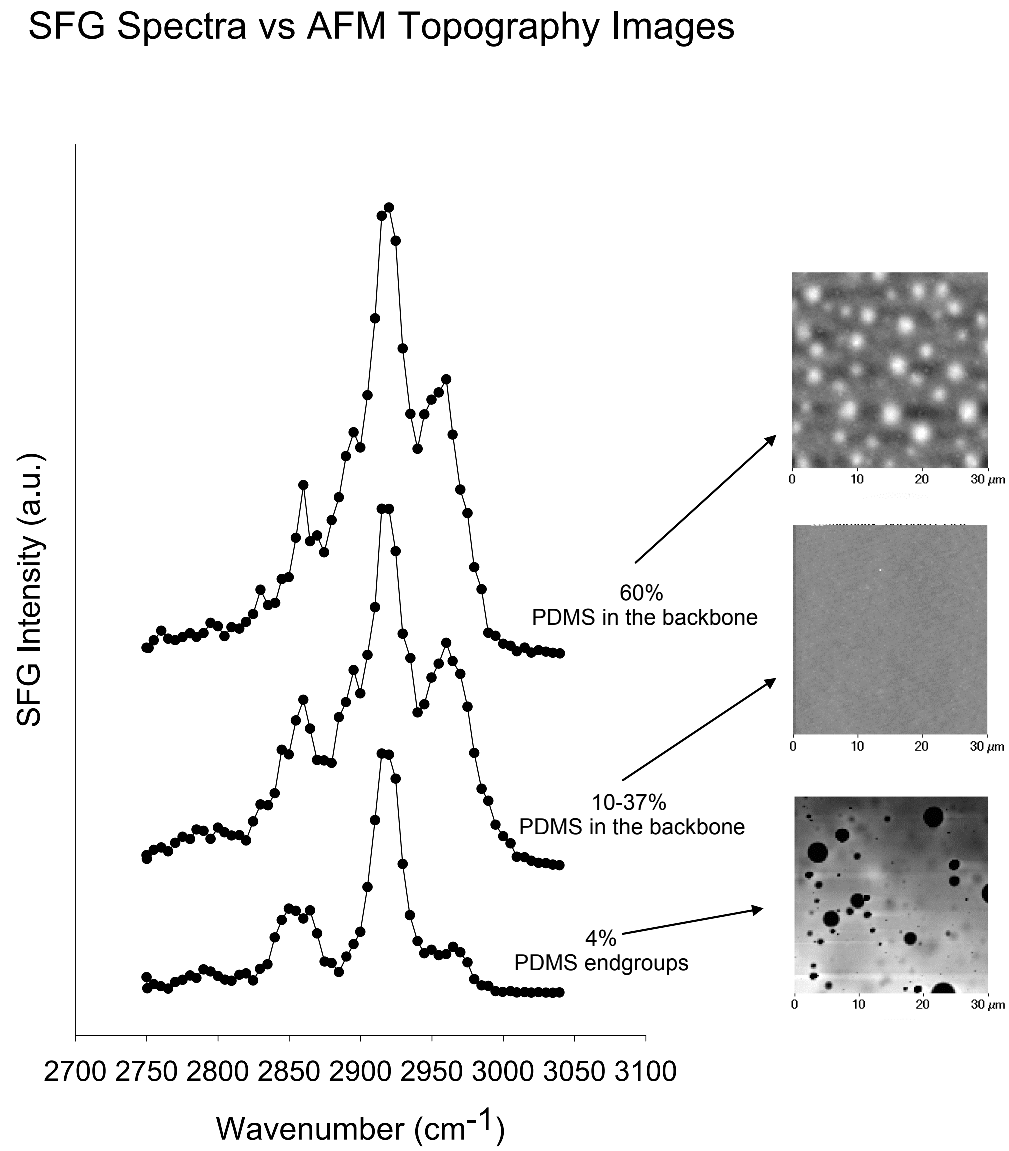

Figure 5.4 – SFG spectra of co-polymers containing silicone vs. polymers with silicone surface modifying end groups. AFM imagines indicate that surface morphology does not affect SFG spectra.

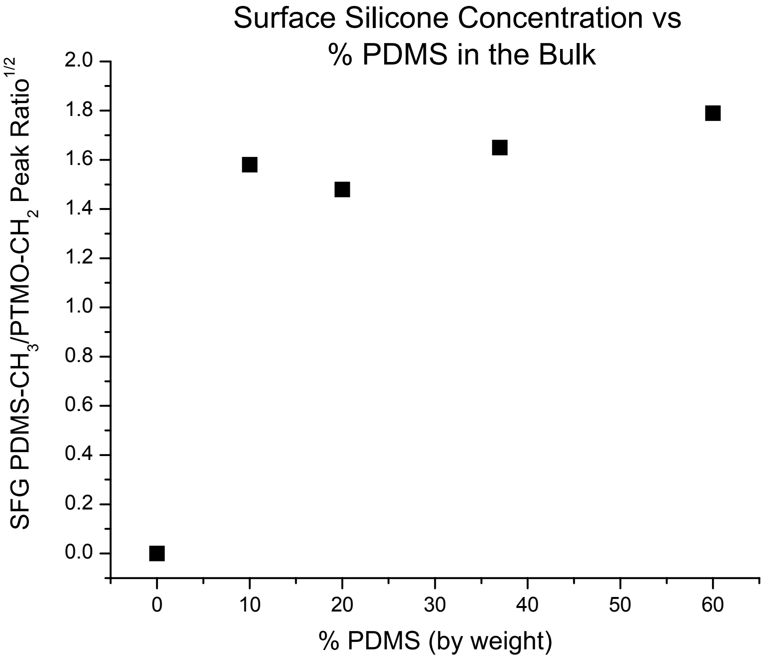

Figure 5.5 – Ratio of SFG CH_2 peaks from polyetherurethane (PTMO) backbone to PDMS CH_3 groups suggests that the concentration range where the bulk PDMS linearly correlated to surface PDMS was from 0% to 10% PDMS in the bulk co-polymer.

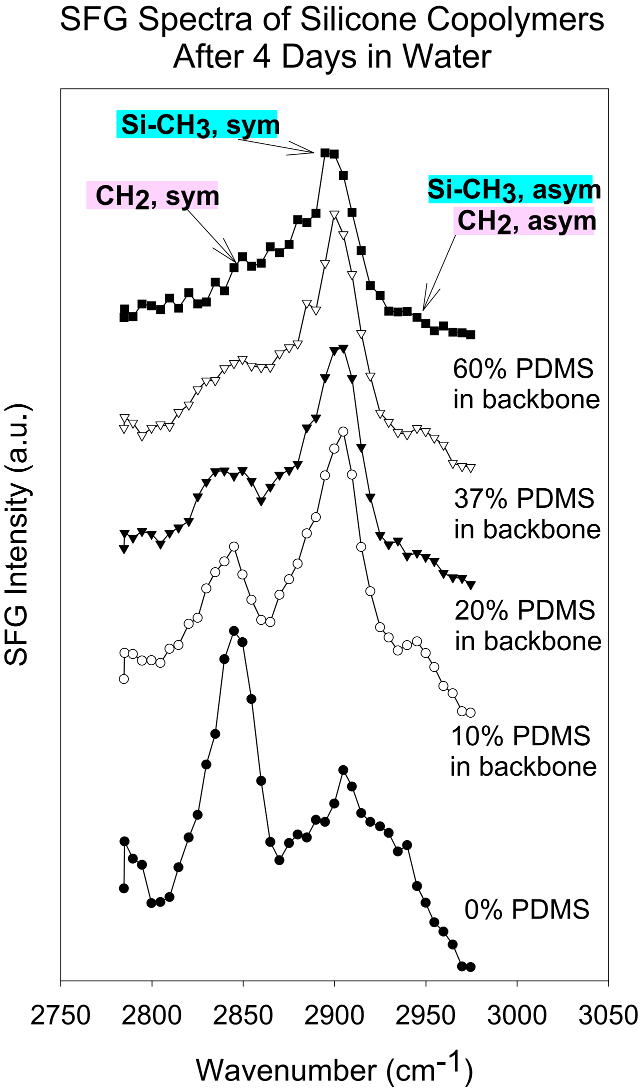

Figure 5.6 – SFG spectra of Polyetherurathane-Silicone co-polymers after exposure to water. CH_2 vibrational bands from polyetherurethane backbone are highlighted in blue and silicone CH_3 vibrational bands in pink.

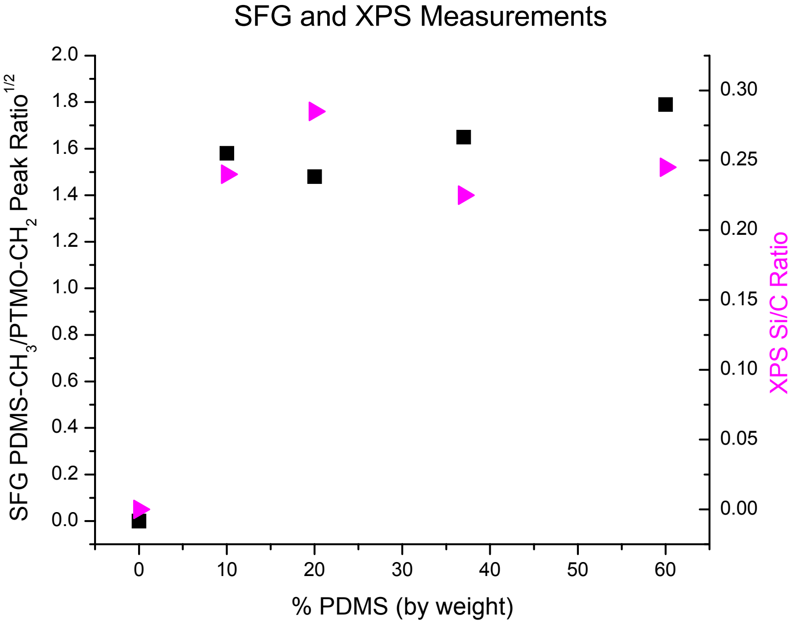

Figure 5.7 - SFG comparison to XPS measurements taken from polyetherurathane-silicone co-polymer series.

Chapter 6

CO Oxidation on Electrified Platinum Surfaces in Acetonitrile/Water Solutions Studied by Sum Frequency Generation and Cyclic Voltammetry

6.1 Introduction

The useful lifetime of an electrochemical cell is dominated by chemical reactions that occur at the electrode/ electrolyte interface [1]. One specific example of such a reaction is the adsorption and oxidation of CO, a well-known poison in electrochemical cells. CO adsorption on platinum has been extensively studied in aqueous and non-aqueous solutions using several *in-situ* spectroscopy techniques [2-10]. However, previous studies of CO electro-oxidation on platinum have been performed solely in aqueous solutions [11-14].

In this laboratory, adsorbed CO and its oxidation have been previously monitored by sum frequency generation (SFG) – surface vibrational spectroscopy in aqueous electrolytes [13]. An intermediate CO species, that was invisible to SFG, was reported 200 mV before the main oxidation peak of the CO layer. The use of SFG in these studies has the advantage that SFG is sensitive to only the electrode/electrolyte interface and therefore no reference spectrum is necessary to achieve surface sensitivity.

In this study, SFG has been used successfully to monitor the oxidation of adsorbed CO at the Pt / acetonitrile interface as a function of external potential and water concentration. By using acetonitrile as an electrolyte, the oxidation potential of CO can be increased, making a larger potential range where an SFG invisible species is observed before oxidation occurs.

In acetonitrile/water electrolytes the vibrational band of adsorbed CO is not observed at potentials above +900mV, while CV data suggest that the CO remains on the surface and is oxidized at +1700 mV. We attribute the CO peak disappearance in SFG spectra to a reversible re-orientation of the CO molecules at the electrode interface and not to an artifact of the thin film arrangement used in this experimental setup [14].

Studies described herein confirm that the intermediate oxidation steps of CO in acetonitrile were similar to those intermediates observed in previous studies using aqueous electrolytes [13].

SFG vibrational spectroscopy is a unique surface probe with which molecular level studies of an electrified surface can be performed [13,15]. In contrast to many other surface techniques, SFG vibrational spectroscopy can be performed at any interface accessible by light, including buried interfaces such as the electrode/electrolyte interface [13,15-18]. SFG provides vibrational spectra of adsorbed surface species, while cyclic voltammetry (CV) studies provide information about oxidation/reduction reactions occurring at the electrode surface. Combined SFG and CV studies provide valuable insight into the effects of applied electric fields on interfacial chemistry.

In this chapter the potential dependent CO behavior on Pt electrodes in neat acetonitrile and acetonitrile solutions containing 0.05 and 0.10 mole fractions of water is described. All experiments were carried out with pre-adsorbed CO monolayers with and without CO also present in the bulk electrolyte.

6.2 Experimental Details

A clean polycrystalline Pt electrode was prepared by flame annealing to 1300 °C in a H_2/air flame and cooling to room temperature in a flow of argon. The electrode cleaning preparation procedure was confirmed by cyclic voltammetry of Pt in 0.05 M H_2SO_4 and observing the characteristic hydrogen adsorption/desorption features [19].

Upon removal from the argon stream, the electrode is immediately covered with a drop of pure acetonitrile and transferred into the spectroscopy cell. The cell is then filled with Ar purged and CO saturated neat acetonitrile or acetonitrile/water solutions. Because acetonitrile is an aprotic solvent, 0.1 M $LiCF_3SO_3$ was added as a supporting electrolyte. CO was adsorbed onto the surface at a slightly negative potential, -250 mV (SCE), for approximately 30 minutes to insure monolayer coverage [5, 9, 13, 20].

Because of the significantly higher solubility of CO in non-aqueous electrolytes, i.e. approximately 10 times higher than that in aqueous solutions [5], particular care was taken to remove excess CO from the bulk electrolyte. While maintaining a slightly negative potential, fresh Ar purged electrolyte was flowed through the cell to ensure no CO was present in the bulk electrolyte. In several instances, CO saturated electrolytes were also used to serve as control experiments.

Spectroscopy is performed in a thin layer electrochemical cell, described elsewhere [13], with ~ 10 μm layer of electrolyte trapped between the CaF_2 window and the polycrystalline Pt electrode. The infrared is attenuated <10% in this geometry in the CO stretching region. The thin layer cell is equipped with the polycrystalline Pt working electrode and a Pt wire counter electrode. Several experiments were performed using Ag/AgCl , KCl saturated (0.197V vs. NHE [21]) as a reference electrode while other described experiments were performed using a standard calomel electrode (SCE) (0.241V vs. NHE [21]); however, all potentials are reported relative to the SCE.

Acetonitrile/water electrolytes were made volumetrically using standard dilution procedures. The acetonitrile, ACS or HPLC grade (<0.001x, mole fraction water), and the $LiCF_3SO_3$ electrolyte were both obtained from the Sigma-Aldrich Chemical Company. Deionized water, triple distilled with resistivity greater than 18.2 Mohms cm^{-1}, was used for these experiments. Ultra high purity Ar, 99.9995 %, used for electrolyte purging was obtained from Bay Airgas. CO, 99.5% purity, was obtained from Scott Specialty Gases and used in conjunction with a cold trap to minimize metal carbonyl contamination.

The spectroscopic cell is transferred under potential control to the SFG optics setup where spectroscopy can be performed. The potential range investigated in this study is -400 to +2000 mV vs. SCE. Voltammetry studies indicate the oxidation of acetonitrile at potentials above +1800 mV. With the addition of water, the positive potential is limited to +1600 mV due to the formation of a Pt oxide [22].

Details of the optical setup for the SFG experiment have been described previously [13,22]. Tunable mid-infrared light (1300-4000 cm $^{-1}$) is generated by difference frequency mixing tunable near-infrared light with the fundamental beam of the Nd:YAG pump laser in a $LiNbO_3$ or $AgGaS_2$ crystal. The near-infrared light is produced through optical parametric generation and amplification of 532 nm light in angle tuned barium borate crystals. The infrared and visible beams are incident on the liquid/solid interface at 40° and 35° and have energy densities of 4 mJ/cm^2 and 15 mJ/cm^2, respectively. All experiments are done with the ppp polarization combination (p-polarized SF, p-polarized visible, and p-polarized infrared).

6.2.1 Data Collection and Analysis

SFG spectra presented herein are an average of 3 to 5 scans. SFG signal was collected for 1 to 5 seconds, i.e. 20 to 100 shots, at every 5 cm^{-1} interval.

Collected SFG signal is normalized with respect to the reflected IR beam from the electrode to ensure that no false SFG peaks were observed due to IR absorption by the thin film of electrolyte above the electrode surface.

6.3 Results and Discussion

6.3.1 Sum Frequency Generation Studies of CO on Pt in Neat Acetonitrile

Figure 6.1 presents SFG spectra obtained from a CO monolayer adsorbed at –250mV on Pt in neat acetonitrile electrolyte. The peak at 2065cm^{-1} is assigned to the vibration of CO adsorbed to one Pt atom, an atop site [7,23].

On the positive potential sweep the CO peak is no longer detected by SFG above +1600 mV, Figure 6.1d. However, by immediately scanning to a potential below +1600 mV, the CO vibrational peak is observed again, and once the potential is returned to –250 mV (Figure 6.1f), the initial intensity of the CO peak is re-obtained. As seen in Figure 6.2a, data indicate a complete recovery of the initial CO vibrational band in neat acetonitrile electrolyte when no CO is present in the bulk electrolyte.

It is suggested that the disappearance of the CO peak in SFG at the electrode at high positive applied potentials is the re-orientation of the C-O bond to a nearly parallel position relative to the electrode surface - an SFG invisible species. If the electro-oxidized CO were simply desorbed from the electrode surface it is expected that a feature would appear in the voltammogram corresponding to desorption of a chemisorbed CO species. No corresponding voltammetry peak was observed. These data indicate CO oxidation does not occur in the absence of water and that the disappearance of the CO peak is due to a reorientation of the CO molecule at the electrode interface.

6.3.2 Sum Frequency Generation Studies of CO on Pt in Acetonitrile/Water Solutions

With the addition of 0.05 mole fraction of water to the acetonitrile electrolyte solution a different CO peak behavior is observed. Figure 6.2b shows, that unlike the pure acetonitrile system, when water is present in small concentrations the original CO peak that was detected by SFG does not return upon cycling back to lower potentials. After oxidation a low intensity, very broad peak is observed at 2025 cm^{-1}, see Figure 6.3f. This vibrational feature is likely due to small amounts of CO present in solution during the positive potential sweep and subsequently adsorbing on the surface upon a negative potential sweep (forming a submonolayer CO layer).

The CO vibrational band is observed until the applied potential is raised to +1000mV, Figure 6.3d. When no CO is present in the bulk electrolyte, the initial CO vibrational intensity, Figure 6.3a, is not regained upon returning to negative potentials, Figure 6.3f. Experiments performed with CO in the bulk electrolyte show that full monolayer coverage is obtained after oxidizing the initial CO monolayer and then returning to negative potentials, Figure 6.2b-triangles.

By increasing the concentration of water in the electrolyte to 0.10 mole fraction, the CO vibrational band shows similar behavior to SFG studies with less water. When CO is not present in the bulk, the CO vibrational feature disappears above +1000 mV and is not regained by returning to lower potentials.

The SFG peak associated with CO does not reappear in the acetonitrile/water solutions (circles in Figure 6.2b) indicating oxidation of CO to CO_2, not simply desorption of CO. These data also indicate that the adsorbed CO layer is not visible by SFG on the electrode surface above +1000 mV in acetonitrile/water solutions and confirm the necessity of surface oxygen containing species [24], most likely a hydroxyl species, for the oxidation of CO on the electrified Pt surface.

Previous studies of the Pt – acetonitrile/water electrified interface indicated that at slightly negative potentials, i.e. less than 0 mV NHE, H_2O molecules were adsorbed at the surface while at low and high positive potentials water molecules were displaced by acetonitrile molecules [22]. In these studies, SFG spectra indicate that with the addition of CO the Pt surface is covered with a chemisorbed CO species at all potentials below the CO oxidation potential.

6.3.3 CO Vibrational Band Behavior versus Applied Potential and Water Concentration

As indicated in Figures 6.1 and 6.3 a 20 cm^{-1} blue shift of the CO vibrational peak is observed (2085cm^{-1} vs. 2065 cm^{-1}, Figure 6.1) with applied potential. This typical blue shift is primarily caused by the Stark effect, whereby the applied potential increases the electric field felt by the adsorbed CO molecules and essentially further separates the vibrational energy levels [4,25,26].

Figure 6.4 displays the CO vibrational band shift as a function of scanned potential and water concentration. By increasing the water concentration in electrolyte solutions, a red shift was observed in the CO vibrational band frequency. The observed vibrational frequency of adsorbed CO at –250mV is slightly lower, 2055 cm^{-1} vs. 2085cm^{-1}, when the bulk electrolyte contains 0.05 mole fraction of water as compared to neat acetonitrile. The red shift in the CO vibrational peak with increased water concentration is attributed to a change in the dielectric screening of the incident infrared radiation caused by additional water molecules in the double layer region [7].

By increasing the concentration of water in the electrolyte to 0.10 mole fraction, the vibrational band of the adsorbed CO layer exhibits a larger red shift to 2030 cm^{-1}. In addition, as the electrode potential is increased, the CO vibrational band blue shifts similar to that observed in the 0.05 mole fraction water in acetonitrile and neat acetonitrile electrolyte studies.

6.3.4 Cyclic Voltammetry Studies - Confirmation of Spectroscopy Results

Voltammetry data for Pt in water/acetonitrile solutions are shown in Figure 6.5. CV studies indicate that in the potential range of interest, acetonitrile undergoes no chemical reaction with the Pt electrode surface, Figure 6.5a. With the addition of water to the electrolyte solution a feature attributed to the oxidation of Pt is observed to begin around +900mV, and the reduction of this oxide is seen on the negative potential sweep at +400 mV, Figure 6.3b. Figure 6.3c shows that with an adsorbed

CO monolayer, the observed CV features are significantly altered due to the adsorbed CO layer. A pre-oxidation wave of CO is observed at the onset of the Pt oxide formation peak, +900 mV, as seen in 6.5b. The second feature at +1600 mV in Figure 6.5c is the main oxidation peak of CO. Lastly, the third peak at approximately +2000 mV is the oxidation of the acetonitrile in the electrolyte. These results have been confirmed by earlier studies performed by this laboratory [22]. These CV data confirm that by using acetonitrile as an electrolyte the oxidation of CO can be delayed, enlarging the potential region where CO is invisible to SFG.

Finally, Figure 6.6 shows that the disappearance of the SFG CO vibrational feature in water/acetonitrile solutions coincides with the observed pre-oxidation wave in voltammetry around +900 mV. As suggested by Lucas *et al* [12], the pre-oxidation wave removes a small number of weakly bonded CO from the surface thereby allowing the rest of the CO layer to relax. The disappearance of a CO SFG signal before the main oxidation wave and the subsequent regaining of the signal by decreasing the potential, as shown in Figure 6.4, suggest the re-orientation of the CO molecules at the surface before oxidation. Desorption and readsorption of CO prior to oxidation would be indicated by additional CV peaks not observed in this study. Voltammetry and spectroscopy studies combined suggest an intermediate CO species, parallel or nearly parallel to the Pt surface, and therefore SFG invisible, is formed after the pre-oxidation wave before the main oxidation of CO to CO_2.

6.4 Summary and Conclusions

Combined CV and SFG studies on Pt electrodes confirm an SFG invisible species is the intermediate in the electro-oxidation of CO to CO_2 in acetonitrile/water electrolytes. Data obtained in both CV and SFG experiments indicate that even small amounts of water, i.e., 0.05 mole fraction, are capable of oxidizing a monolayer of CO on the platinum electrode surface. CV data also indicate the pre-oxidation wave coincides with the decrease in the intensity of the SFG CO vibrational band associated with the intermediate CO surface species. The pre-oxidation wave removal of a small number of weakly bonded CO from the surface [12] allows the remaining, more strongly adsorbed CO molecules re-orient with the CO bond parallel to the surface.

Observed spectroscopic and voltammetry data suggest that the oxidation pathway of CO on Pt in acetonitrile/water solutions is very similar to the oxidation of these monolayers in completely aqueous environments [13]. Previous SFG studies using acetonitrile as an electrolyte have shown this to be an ideal electrolyte system for monitoring surface OH species at the Pt – electrolyte interface [22]. By using acetonitrile as an electrolyte, IR absorption by the bulk solution can be minimized in the vibrational ranges of interest and therefore the formation and consequent reduction of surface OH species can be more easily monitored in future studies.

6.5 References

1. Bard, A.J., Faulkner, L.R., *Electrochemical Methods*, Wiley & Sons, New York (2001).

2. Kim, C.S., Tornquist, W.J., Korzeniewski, C., *J. Phys. Chem.,* **97**, (1993), p. 6484.

3. Kim, C.S., Korzeniewski, C., Tornquist, W.J., *J. Chem. Phys.,* **100**, (1994), p. 628.

4. Weaver, M.J., *Applied Surface Science*, **67**, (1993), p.147.

5. Cuesta, A., Gutierrez, C., *J. Electroanal. Chem.*, **395**, (1995), p. 331.

6. Peremans, A., Tadjeddine A., Zheng, W.Q., Le Rille, A., Guyot-Sionnest, P., Thiry, P.A., *Surface Science*, **368**, (1996), p. 384.

7. Korzeniewski, C., Huang, J., *Analytica Chimica ACTA*, **397**, (1999), p. 53.

8. Tang, C., Zou, S., Weaver, M.J., *Surface Science*, **412/413**, (1998), p. 344.

9. Huang, J., Korzeniewski, C., *J. Electroanal. Chem.,* **471**, (1999), p. 146.

10. Curulla, D., Clotet, A., Ricart, J.M., *Surface Science*, **460**, (2000), p. 101.

11. Xia, X.H., Vielstich, W., *Electrochimica Acta*, **39 no.1**, (1994), p. 13.

12. Lucas, C.A., Markovic, N.M., P.N. Ross, *Surface Science*, **425**, (1999), p. L381.

13. Baldelli, S., Markovic, N., Ross, P.N., Shen, Y.R., Somorjai. G.A., *J. Phys. Chem. B*, **103**, (1999), p. 8920.

14. Dederichs, F.M., Friederich, K.A., Daum, W., *J. Phys. Chem. B*, **104**, (2000), p. 6626.

15. Baldelli, S., Schnitzer C., Campbell, D.J., Shultz, M.J., *J. Phys. Chem. B.*, **101**, (1997), p. 10435.

16. Bain, C.D. *J. Chem Soc., Faraday Trans.*, **91**, (1995), p. 1281.

17. Du, Q., Superfine, R., Freysz, E., Shen, Y.R., *Phys. Rev. Lett.*, **70**, (1993), p. 2313.

18. Y. R. Shen, *Nature*, **337**, (1989), p. 519.

19. Clavilier, J., *Interfacial Electrochemistry*, (1999), pp231-248.

20. Anderson, M.R., Huang, J., *J. Electroanal. Chem.* **318**, (1991), p. 335.

21. Ives, D.J.G., Janz, G.J., *Reference Electrodes*, Academic, New York, (1961).

22. Baldelli S., Mailhot, G., Ross, P.N., Shen, Y.R., Somorjai, G.A., *J. Phys. Chem. B,* (2000).

23. Anderson, M.R., Huang, J., *J. Electroanal. Chem.*, **318**, (1991), p. 335.

24. Gilman, S., *J. Phys. Chem.*, **68**, (1964), p. 70.

25. Lambert, D.K., *J. Chem. Phys.*, **89** (6), (1988), p. 3847.

26. Koper, M.T.M, van Santen, R.A., Wasileski, S.A, Weaver, M.J., *J. Chem. Phys.*, **113 no.10**, 2000, p. 4392.

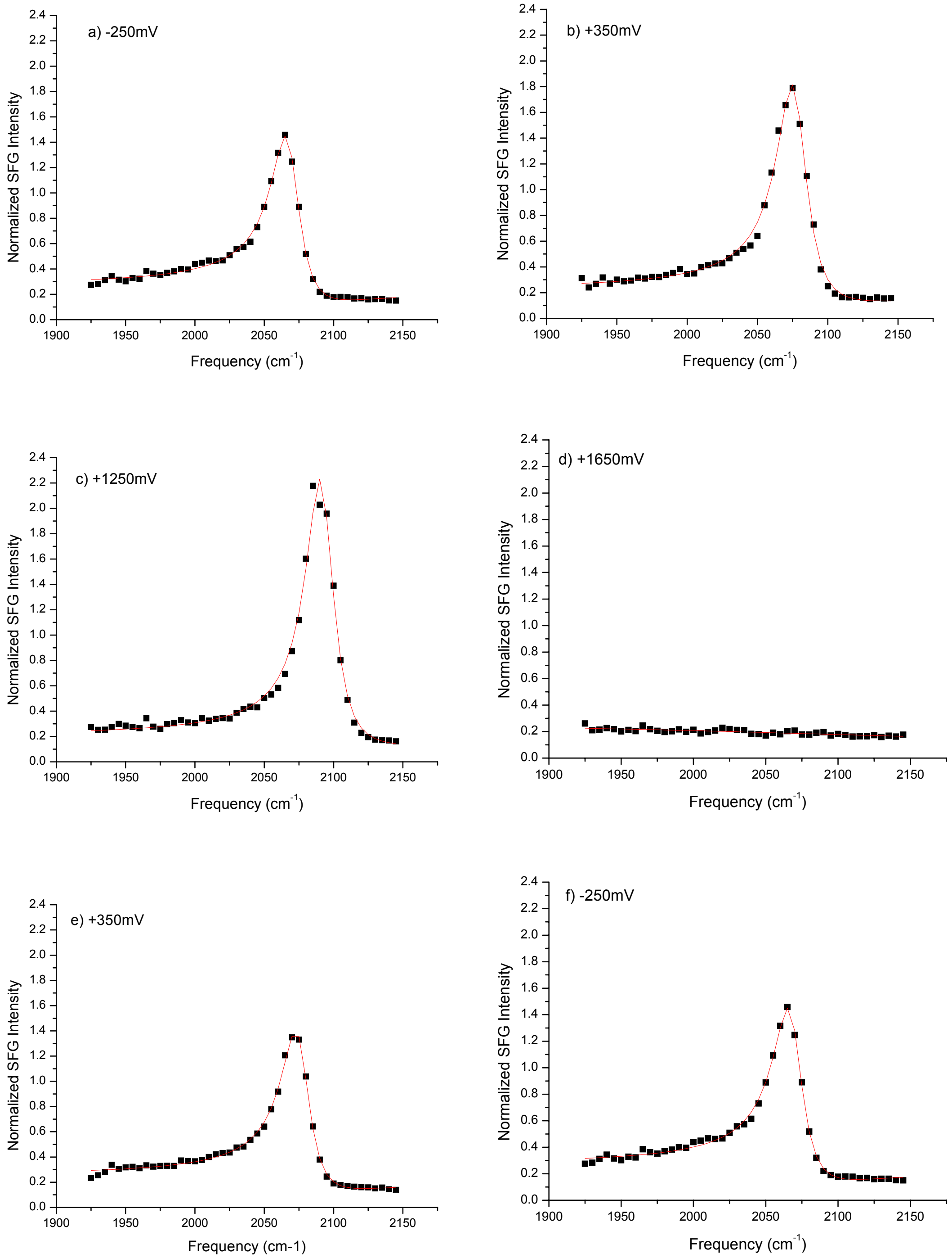

Figure 6.1. SFG spectra, ppp polarization combination, of CO on Pt in Neat Acetonitrile with applied potential a)-250mV, b)+350mV, c)+1250mV, d)+1650mV, and returning to e)+350mV, and f) -250mV (■ - data points, lines - fitted data using equation 1).

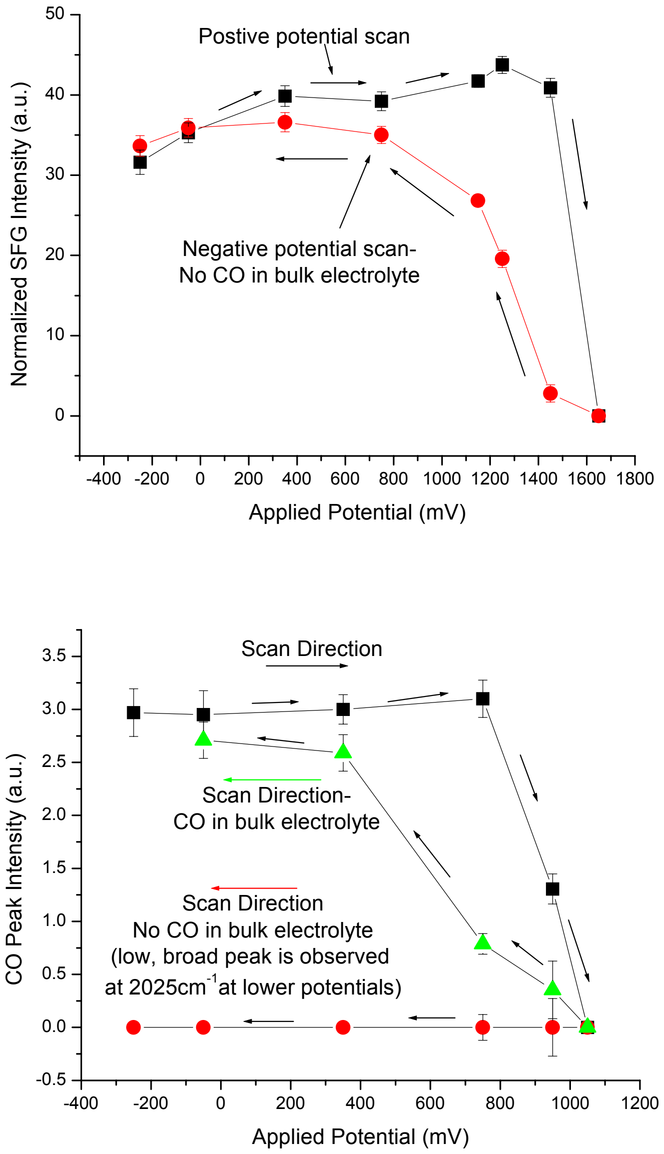

Figure 6.2. CO peak intensity as a function of potential for CO on Pt in CH_3CN and CH_3CN/H_2O solutions.
a) Neat CH_3CN ■- positive potential sweep, ● - negative potential sweep (no CO in bulk electrolyte), b) CH_3CN with 0.05x H_2O ■- positive potential sweep, ● - negative potential sweep (no CO in bulk electrolyte), ▲ - negative potential sweep (CO in bulk electrolyte).

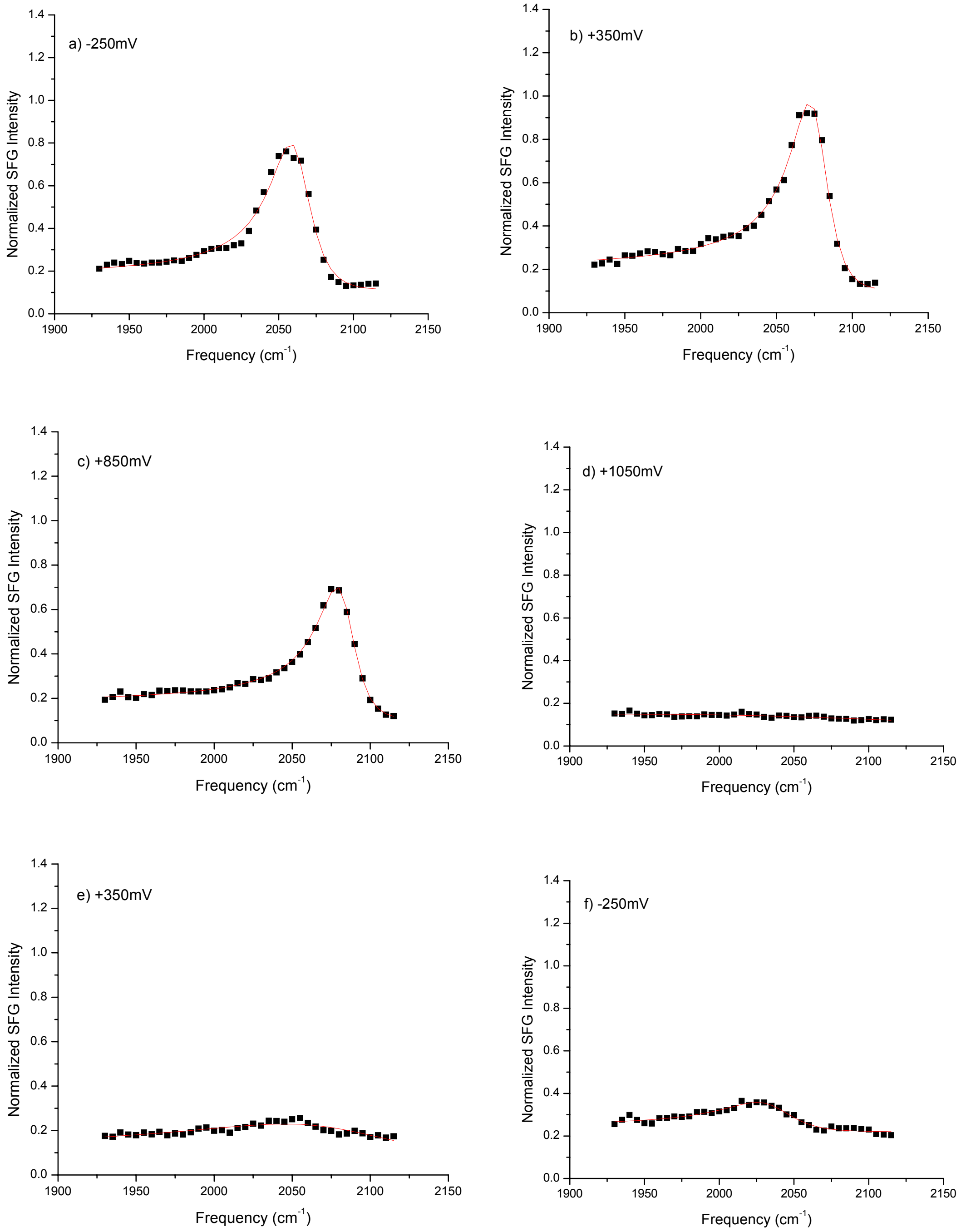

Figure 6.3. SFG spectra, ppp polarization combination, of CO on Pt in 0.05 mole percent Water In Acetonitrile with applied potential a)-250mV, b)+350mV, c)+850mV, d)+1050mV, and returning to e)+350mV , and f) -250mV (■ - data points, lines - fitted data using equation 1).

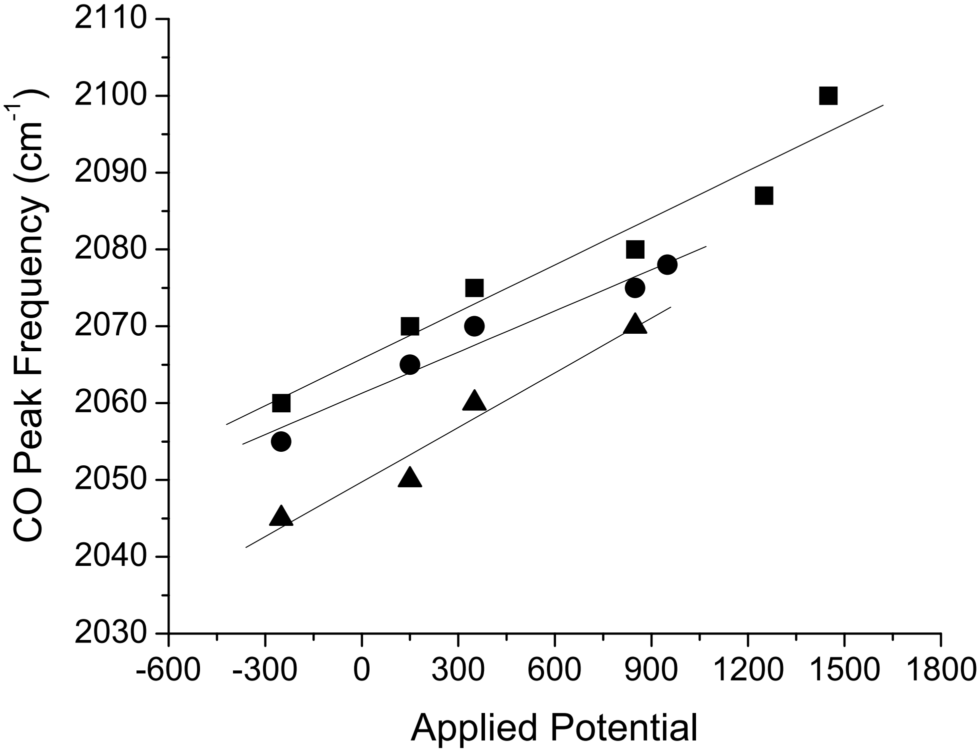

Figure 6.4. CO peak shift and intensity change with scanned potential. ■ - neat CH_3CN, ● - $0.05xH_2O$ in CH_3CN, and ▲ - $0.10xH_2O$ in CH_3CN.

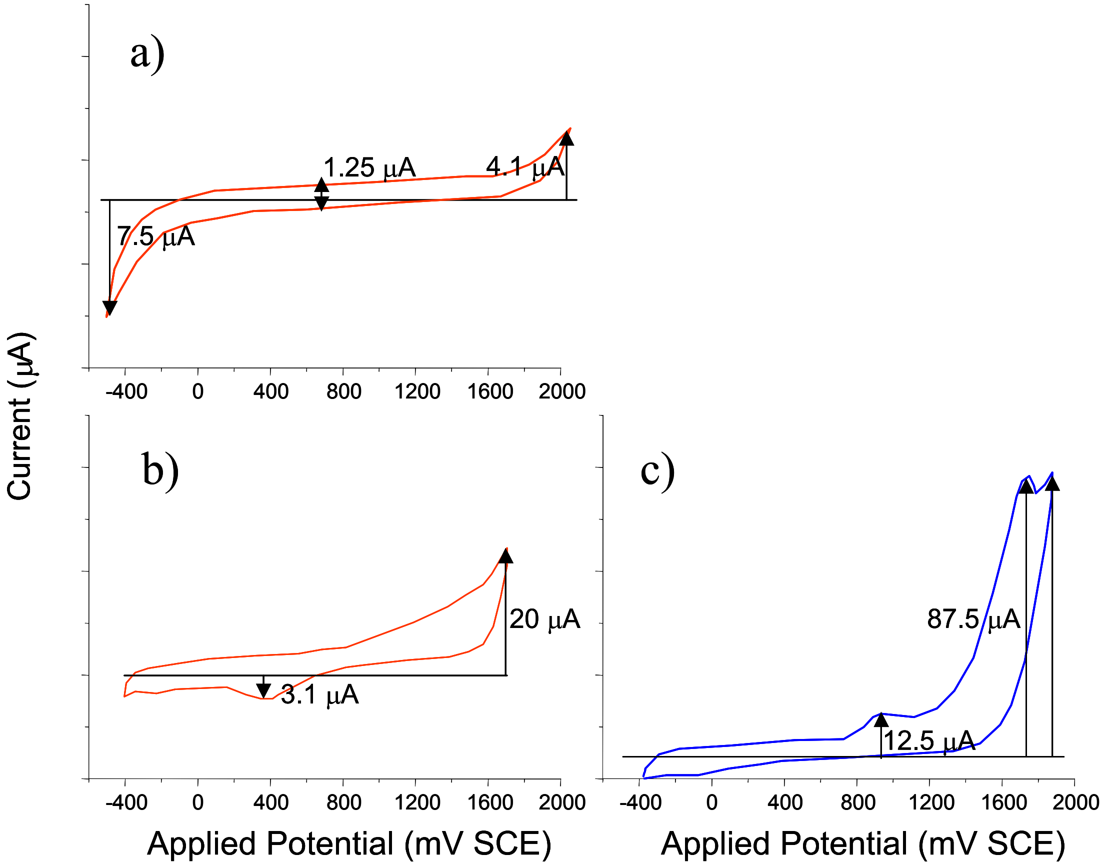

Figure 6.5. Voltammetry data obtained from CO monolayers adsorbed on Pt with no CO in solution a) Pt in CH_3CH CV; b) Pt in CH_3CN/0.10x H_2O; c) Pt in CH_3CN/0.10x H_2O with CO.

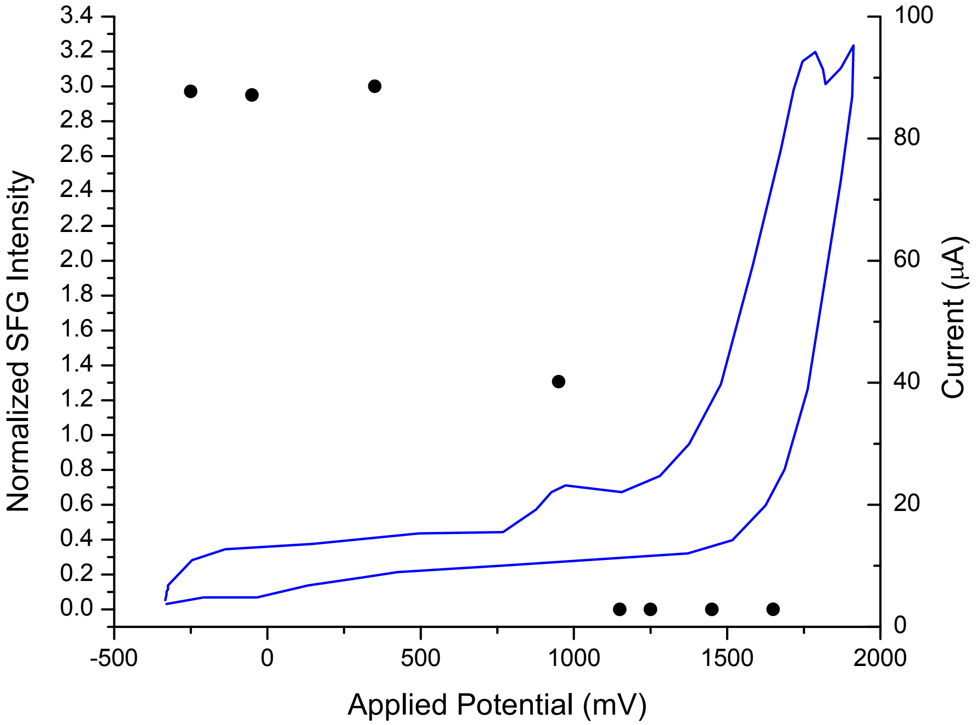

Figure 6.6. CO peak intensity from SFG experiments compared to CV from CO on Pt in CH_3CN/H_2O solutions.

Chapter 7

Electrode/Electrolyte Interactions Studied by Sum Frequency Generation and Cyclic Voltammetry

7.1 Introduction

In situ spectroscopy studies can provide valuable molecular level information about both ionic and neutral species at electrode surfaces [1]. These data can greatly improve the understanding of both chemical and physical processes that occur on a surface under the influence of an electric field. Sum frequency generation (SFG) vibrational spectroscopy in combination with cyclic voltammetry (CV) was used to investigate the effect of the electrode potential on electrolyte molecules. Results suggest that an ordering of the electrolyte molecules is caused by the applied electric field. CV data indicate no other chemical or physical processes were occurring at the potentials where spectroscopic changes were observed. To facilitate the analysis of the SFG and CV data it is suggested the point of zero charge (pzc) be measured for each individual electrode/electrolyte system. It is hypothesized that the spectroscopic changes are observed at or very near to the pzc for each system.

Data presented herein are from four electrode/electrolyte systems: Pt/acetonitrile (CH_3CN), Au/CH_3CN, Cu/CH_3CN, and Pt/dimethyl sulfoxide (DMSO).

7.2 Experimental Details

7.2.1 Sample Preparation

Clean polycrystalline Pt electrodes were prepared by flame annealing to 1300 °C in a H_2/air flame and cooling to room temperature in a flow of argon. The electrode cleaning preparation procedure was confirmed by cyclic voltammetry of Pt in 0.05 M H_2SO_4 and observing the characteristic hydrogen adsorption/desorption features [2]. Upon removal from the argon stream, Pt electrodes were immediately covered with a drop of pure electrolyte and then transferred into the spectroscopy cell.

Au electrodes were prepared by vapor deposition onto silicon wafers. Gold films of up to 500nm were rinsed with methanol and electrolyte, and then transferred to the cell. Spectroscopic features attributed to hydrocarbon contamination were not observed when performing SFG on the gold films. For CV studies, hand polished and lightly flame annealed, Au polycrystalline electrodes were used instead of the silicon supported Au films to ensure good electrical contact in the voltammetry cell.

Cu electrodes were prepared by potentially cycling clean polycrystalline electrodes in a 0.5M $CuSO_4$ solution for approximately 15 min. This procedure provided thick optically smooth, Cu films that were suitable for spectroscopy studies. A drop of electrolyte was placed on the Cu electrode before the immediate transfer of the electrode to the spectroscopy cell.

Once the electrode had been placed in the spectroscopy cell, the cell was then filled with Ar purged neat CH_3CN or DMSO solutions. Because CH_3CN and DMSO are aprotic solvents, 0.1 M $LiCF_3SO_3$ was added as a supporting electrolyte. Electrical contact for the working electrodes were made by either a thin Pt wire touching the side of the electrode or a thick Pt wire spot welded to the back of the electrode. Electrical contact was confirmed by the observation of a voltammogram.

7.2.2 Cyclic Voltammetry Studies

CV studies were performed in a separate electrochemical cell, specifically for non-aqueous electrolytes. CH_3CN or DMSO with 0.1 M $LiCF_3SO_3$ solutions were purged for at least 20 minutes to rid the system of excess O_2. Care was taken to minimize air exposure of the electrolyte to limit the amount of water present in the system.

CV studies were performed to determine the potential range of interest for each electrode/electrolyte combination. Voltammograms also provided data on oxidation/reduction (redox) reactions occurring at the electrode surface that might correspond to a particular change in the spectroscopy.

Electrolytes were made volumetrically using standard dilution procedures. The CH_3CN (ACS or HPLC grade,<0.001x, mole fraction water) and the $LiCF_3SO_3$ electrolyte were obtained from the Sigma-Aldrich Chemical Company. 99.5% DMSO

(<0.01% H_2O) was purchased from Fluka Chemicals. Ultra high purity Ar (99.9995%) used for electrolyte purging was obtained from Bay Airgas.

7.2.3 Sum Frequency Generation Studies

Spectroscopy was performed in a thin layer electrochemical cell, described elsewhere [3], with ~ 10 μm of electrolyte trapped between a CaF_2 or fused silica quartz window and the working electrode. The infrared was attenuated <20% in this geometry in the CH stretching region. The thin layer cell was equipped with the Pt, Au or Cu working electrode and a Pt wire counter electrode. Experiments were performed using standard calomel electrode (SCE) (0.241V vs. NHE [4]) as a reference electrode. All potentials are reported relative to the SCE.

Details of the optical setup for the SFG experiment have been described previously [3, 5]. Tunable mid-infrared light (2200-4000 cm^{-1}) was generated by difference frequency mixing tunable near-infrared light with the fundamental beam of the Nd:YAG pump laser in a $LiNbO_3$ crystal. The near-infrared light is produced through optical parametric generation and amplification of 532 nm light in angle tuned barium borate crystals. The infrared and visible beams are incident on the liquid/solid interface at 40° and 35° and have energy densities of 4 mJ/cm^2 and 15 mJ/cm^2, respectively. All experiments were done with the ppp-polarization combination (p-polarized SF, p-polarized visible, and p-polarized infrared). SFG spectra presented herein are an average of 3 to 5 scans. SFG signal was collected for 1 to 5 seconds (20 to 100 shots) at every 5 cm^{-1} interval.

7.3 Results and Discussion

7.3.1 Pt in Acetonitrile

Previous studies performed in this laboratory have shown that CH_3CN has a potential dependant orientation on an electrified Pt surface [6]. As shown in Figure 7.1, SFG data show that the CH_3CN molecule has a potential dependant orientation. An examination on the CV data for the same system reveals no features exist near 800mV, where the spectroscopic changes were observed. The strong orientational response of CH_3CN to the applied potential is attributed to the large dielectric constant of CH_3CN (37.5).

To further probe the effect of electrified surfaces on electrolytes, several different systems that are related to the work earlier published by this laboratory [6] are presented below.

7.3.1 Gold in Acetonitrile

As shown in Figure 7.3, the CV of Au in CH_3CN is very similar to that of Pt in CH_3CN. The voltammogram suggests no redox reactions or adsorption/desorption processes are occurring in the potential range of study. However, SFG results (Figure 7.4) indicate some type of change in the system as the potential is scanned from negative to positive. At open circuit a peak at 2935cm^{-1}attributed to the symmetric CH_3 stretch of CH_3CN was observed. Under potential control no vibrational features were observed for the Au/CH_3CN system until the potential was above 0.9V SCE. At this potential one vibrational feature was observed at 2920cm^{-1}, which is also attributed to the symmetric CH_3 vibration of the electrolyte molecules. As the potential is increased to even more positive the 2920cm^{-1} vibrational band grows in intensity. The 15cm^{-1} red shift of the CH_3 symmetric stretch under potential control, with respect to the open circuit peak frequency (2935cm^{-1}), is not fully understood, but most likely can be related to either: 1) the effect of the applied electric field on the vibrational levels of CH_3CN, 2) the number of CH_3CN molecules at the electrode surface creating dipole, dipole coupling interactions that can change the vibrational levels of CH_3CN, 3) the presence of water molecules in the electric double layer or on the electrode surface interacting with the CH_3CN molecules; or more likely a combination of the three.

As seen in Figure 7.5 no strong vibrational feature at 2877cm^{-1} is observed for the symmetric vibration of CH_3 into the metallic surface (ν_{soft}). This lack of data would suggest a disorder to order transition occurs around 1V SCE, rather than a complete “flipping” of the electrolyte molecules as seen in the Pt/CH_3CN study.

7.3.3 Cu in Acetonitrile

The CV shown in Figure 7.6 indicates many chemical and physical processes occur at the Cu/CH_3CN interface in the same region where Au and Pt CVs show no redox or adsorption/desorption processes. In both CV and SFG experiments, the Cu electrode was solvated over time at various potentials above 0V SCE. Upon further research it was determined that Cu forms a variety of complexes with CH_3CN, especially in the presence of any O_2 or CO contamination [7].

As seen in Figure 7.7, SFG data collected on the Cu/CH_3CN systems proved to be inconclusive, and at best showed the effect of the applied potential on the non-resonant term of the SFG signal. As shown in equation 7.1 the $\chi^{(2)}{}_{NR}$ term has two components: inter-band and intra-band transitions. One can express $\chi^{(2)}{}_{NR}$ as:

$$\chi^{(2)}{}_{NR} = \chi^{(2)inter}{}_{NR} + \chi^{(2)intra}{}_{NR} = \chi^{(2)inter}{}_{NR} + \alpha(V_{dc} - V_{pzc}) + \delta \qquad (7.1)$$

where α and δ are real material dependant constants, and V_{dc} and V_{pzc} are the applied potential and the point of zero charge, respectively. The inter-band term is real and potential dependant. This effect can be observed through the dramatic increase in the background, or non-resonant SFG signal as shown in Figure 7.8.

7.3.4 Pt in Dimethyl Sulfoxide

With the success of observing spectral changes in using CH_3CN, another electrolyte was chosen for comparison. Dimethyl sulfoxide (DMSO) has a dielectric constant similar to that of CH_3CN, 46.7 and 37.5, respectively [9, 10]. As in the Au/CH_3CN system, SFG spectra of the electrified Pt/DMSO interface showed either one or no vibrational bands depending on the applied potential. At 0.4V SCE and more positive potentials no vibrational bands for DMSO were observed (Figure 7.9a). However by lowering the applied potential to 0V SCE (Figure 7.9b) a vibrational band at 2950cm^{-1} attributed to the symmetric CH_3 stretch is observed.

Because of hydroscopic character of DMSO, water contamination from the air could not be kept low enough get a water free CV. CVs imagined for the Pt/DMSO system look like Pt in CH_3CN with H_2O (Figure 6.5b). Similar to the Pt/CH_3CN and Au/CH_3CN systems, Pt/DMSO CV studies showed no features at potentials where spectroscopic changes were observed in SFG studies.

7.4 Conclusions and Future Direction

While the author feels that the above system have provided some interesting results, the inability to connect the observed spectroscopic changes to physical or chemical processes, as seen in CV data, causes some concern. It is hypothesized that the observed spectroscopic changes seen in the Pt/CH_3CN, Au/CH_3CN and Pt/DMSO systems are directly related to the point of zero charge (pzc). With further resources and expertise, the pzc could be measured for each electrolyte/electrode system by doing capacitance measurements [11]. However, pzc measurements will only confirm and give some meaning to potentials at which spectroscopic changes are observed; pzc measurements will not elucidate why a “flipping” of the electrolyte molecule is observed in some systems while only a disordered to ordered transition of the electrolyte molecules for other systems.

7.5 References

1. T. Iwasita and F.C. Nart, *Progress in Surface Science*, **55** (4), Elsevier Scince Ltd, Great Britain, (1997), pp. 271-340.

2. Clavilier, J., *Interfacial Electrochemistry*, (1999), pp231-248.

3. Baldelli, S., Markovic, N., Ross, P.N., Shen, Y.R., Somorjai. G.A., *J. Phys. Chem. B*, **103**, (1999), p. 8920.

4. Ives, D.J.G., Janz, G.J., *Reference Electrodes*, Academic, New York, (1961).

5. Baldelli S., Mailhot, G., Ross, P.N., Shen, Y.R., Somorjai, G.A., *J. Phys. Chem. B,* **105**(3), (2001), pp. 654-662.

6. Baldelli, S; Mailhot, G; Ross, PN; Somorjai, GA., *J.A.C.S.*, **123**(31), (2001), pp. 7697-7702

7. J. Klunker and W. Schafer, *J. Electroanal. Chem*, **466**, (1999), pp. 107–116.

8. A. Tadjeddine and A. LeRille, *Interfacial Electrochemistry,* Marcel Dekker, Inc., New York, NY, (1999), pp. 317-343.

9. (http://www.asiinstr.com/dc1.html)

10. (http://www.cem.msu.edu/~reusch/OrgPage/solvent.htm)

11. Bard, A.J., Faulkner, L.R., *Electrochemical Methods*, Wiley & Sons, New York (2001).

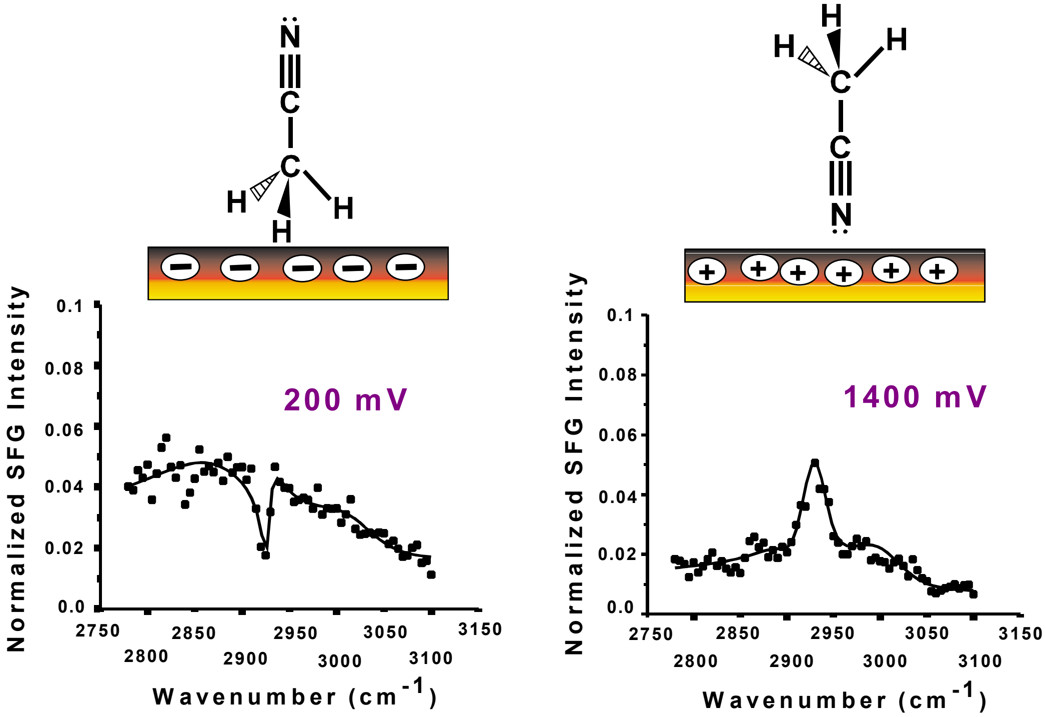

Figure 7.1 - Pt in CH_3CN at a) 200 mV and b) 1400 mV. Dip at 2925cm^{-1} corresponds to the vibrational mode of CH_3 stretching into the metal surface (shown in cartoon), while the peak at 2950cm^{-1} corresponds to the symmetric CH_3 vibrational band away from the metal surface. (Figure adapted from Baledlli *et al* [5])

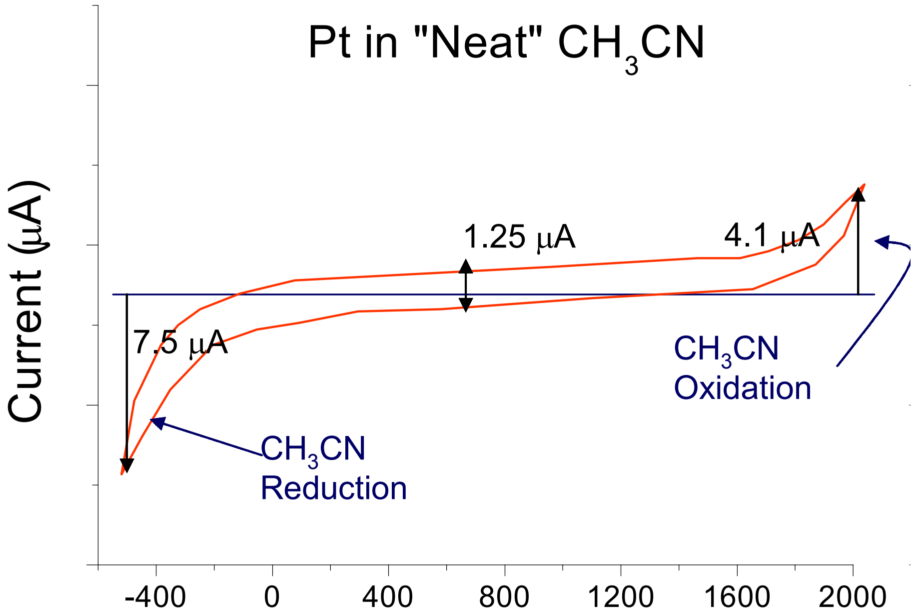

Figure 7.2 - CV of Pt in CH$_3$CN. Note no voltammetry features were seen at potentials where spectroscopic changes were observed (see Figure 7.1).

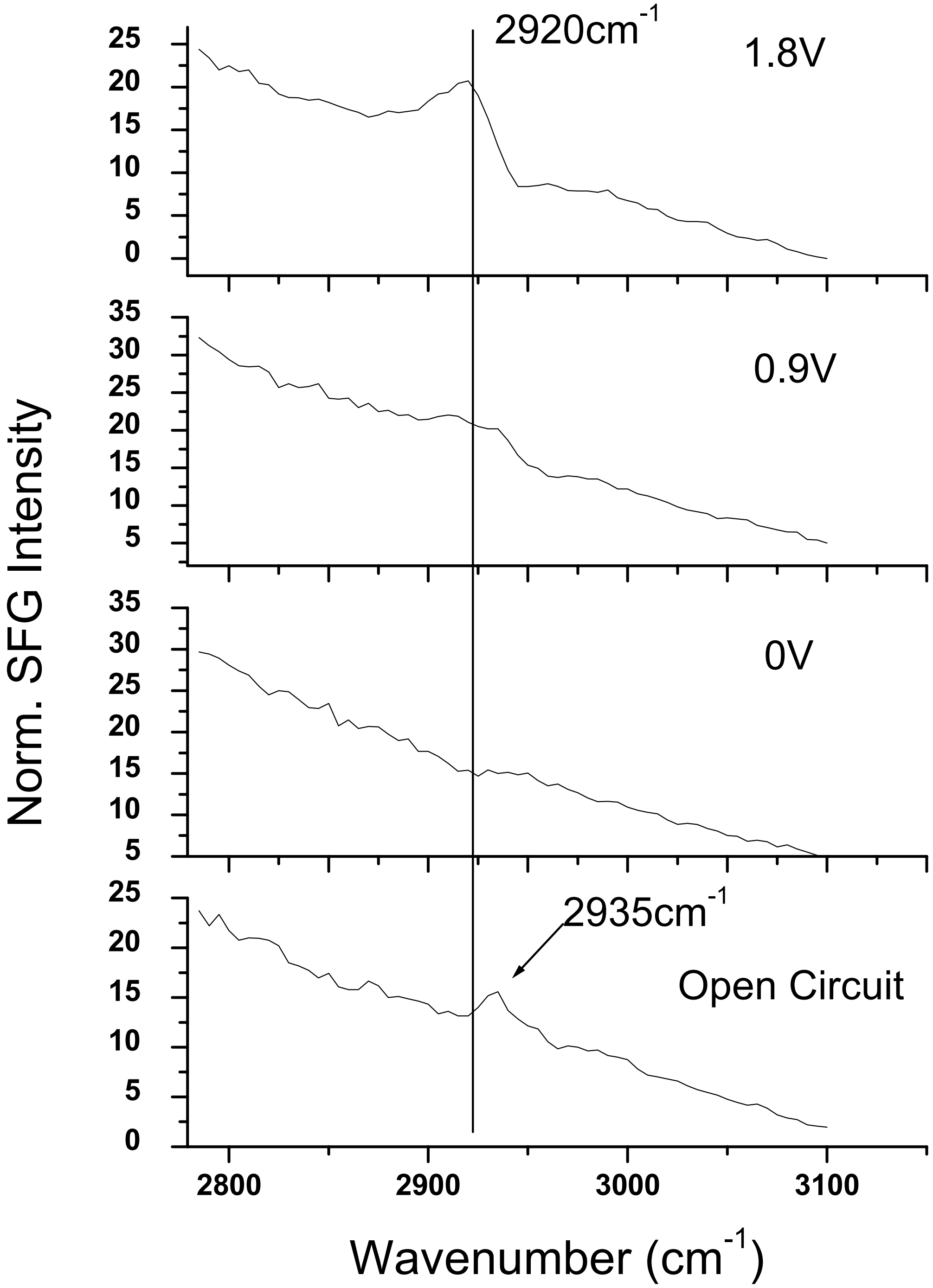

Figure 7.3 - SFG Spectra of Au in CH_3CN. Spectra show the growth and red-shift of the symmetric CH_3 vibrational band assigned to CH_3CN with the CN at the Pt surface.

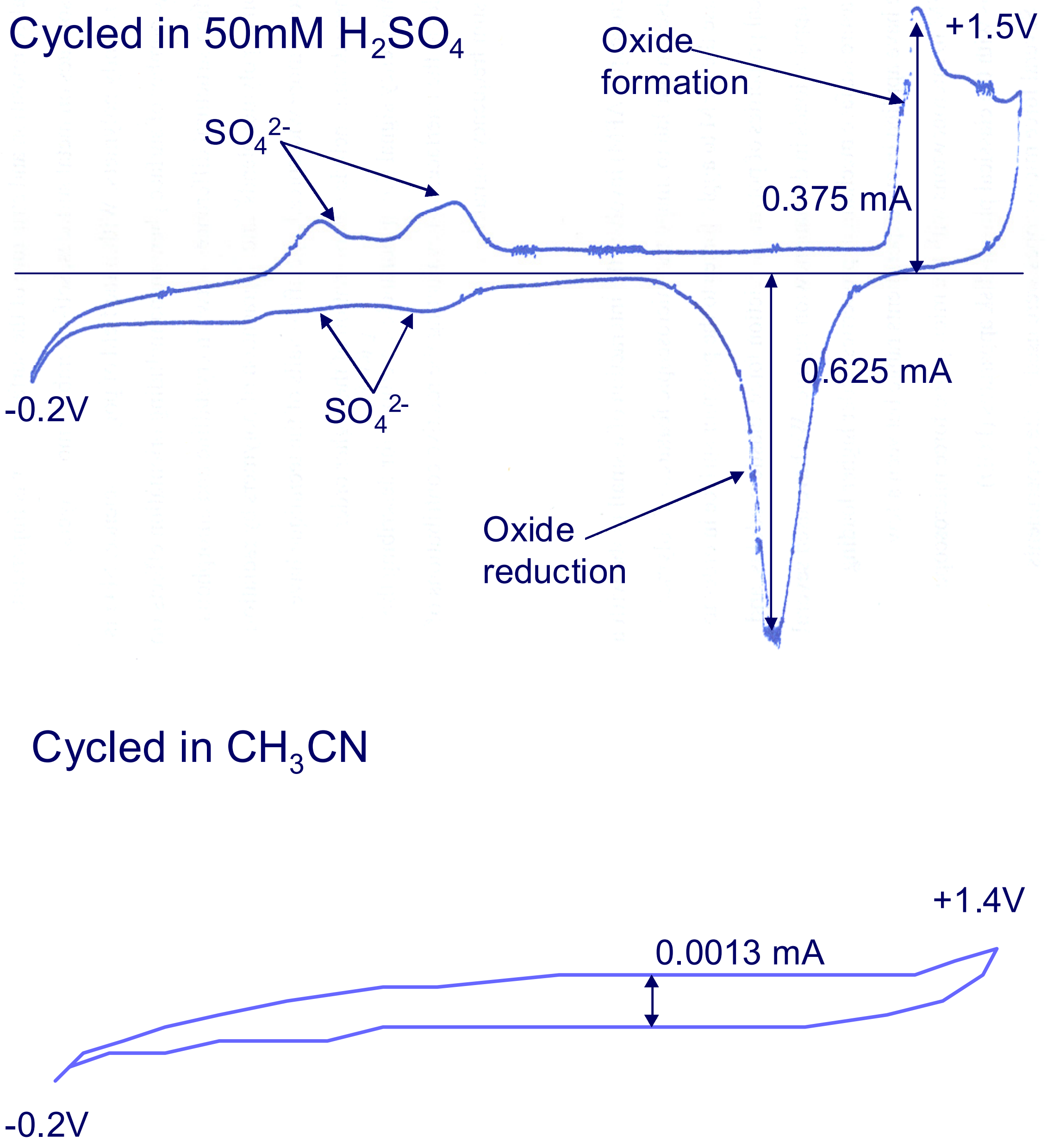

Figure 7.4 - CV of Au a) in 0.5mM H_2SO_4 and b) in CH_3CN. Voltammetry suggest no redox or adsorption/desorption processes occur in CH3CN around 1V where spectroscopic changes are observed in SFG experiments (Figure 7.3).

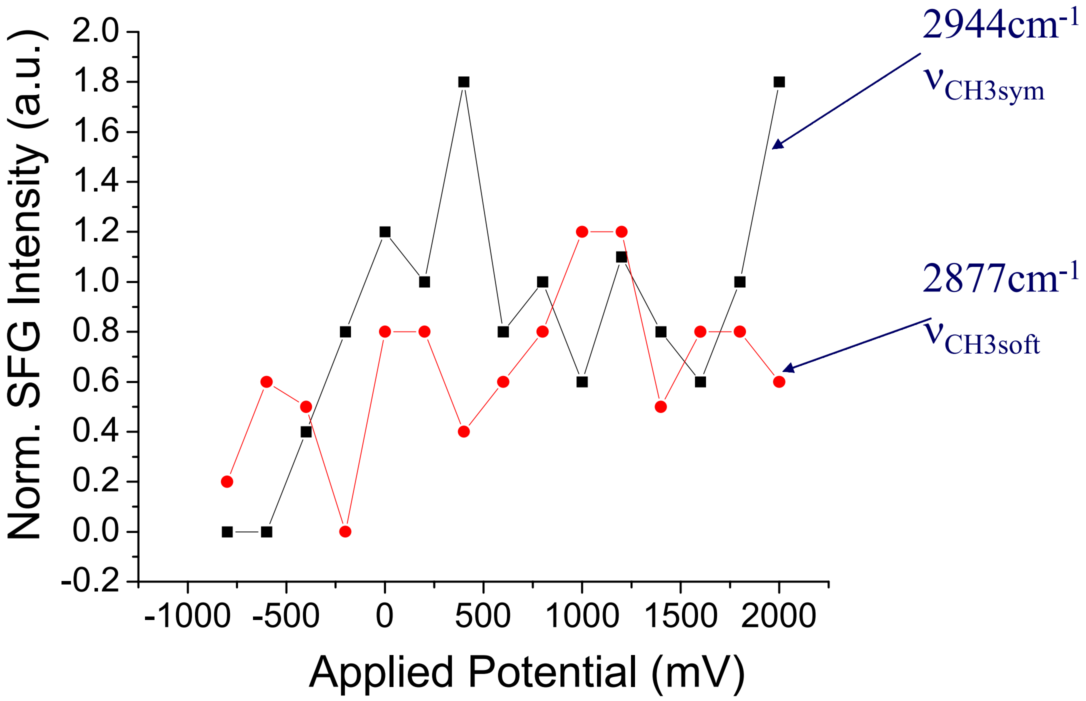

Figure 7.5 - SFG intensity of CH_3 stretching modes from CH_3CN on Au. Soft mode at 2877cm^{-1} is not above noise level in SFG experiment and this cannot be seen in Figure 7.3. Vibrational band at 2944cm^{-1}, as seen in Figure 7.3, has a stronger potential dependence than the 2877cm^{-1} mode.

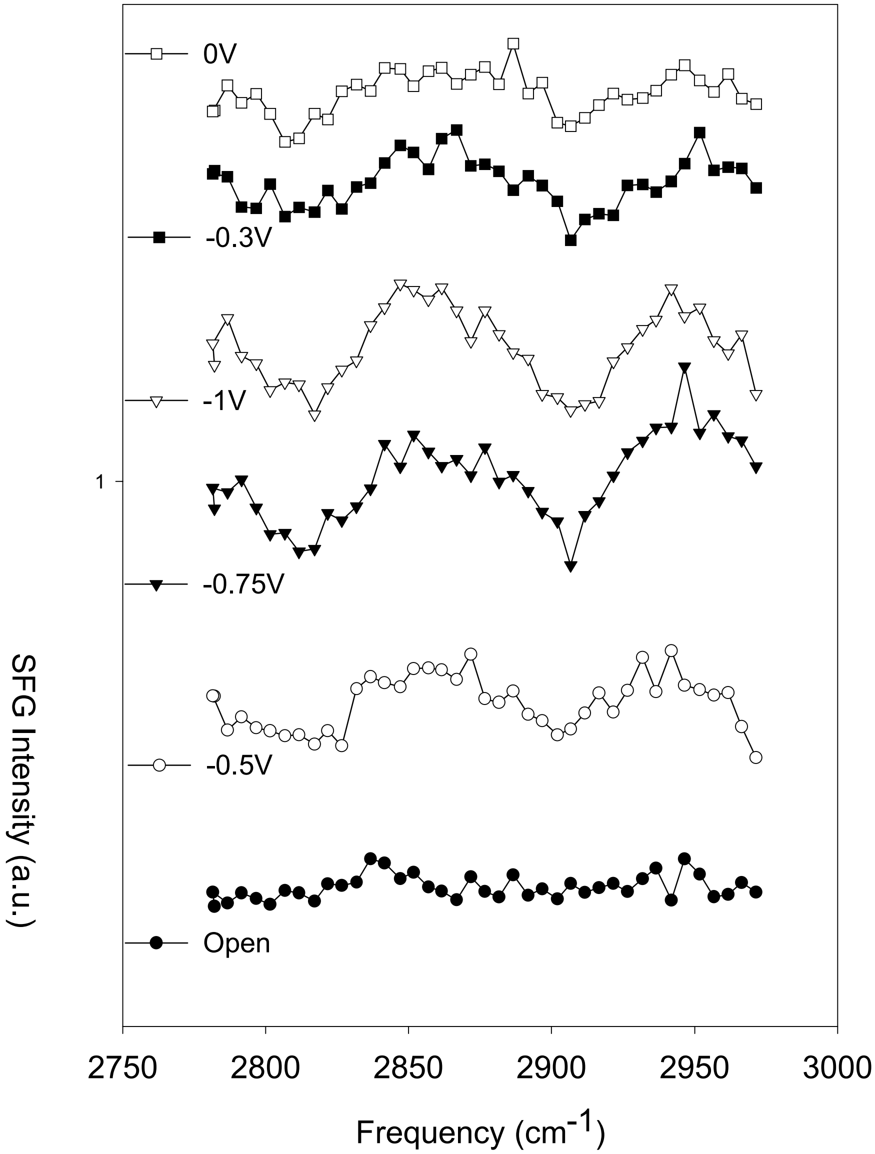

Figure 7.6 - Potential dependant SFG spectra of CH_3CN on Cu. Spectra have been offset from each other for comparison. No spectral assignments can be made for this system.

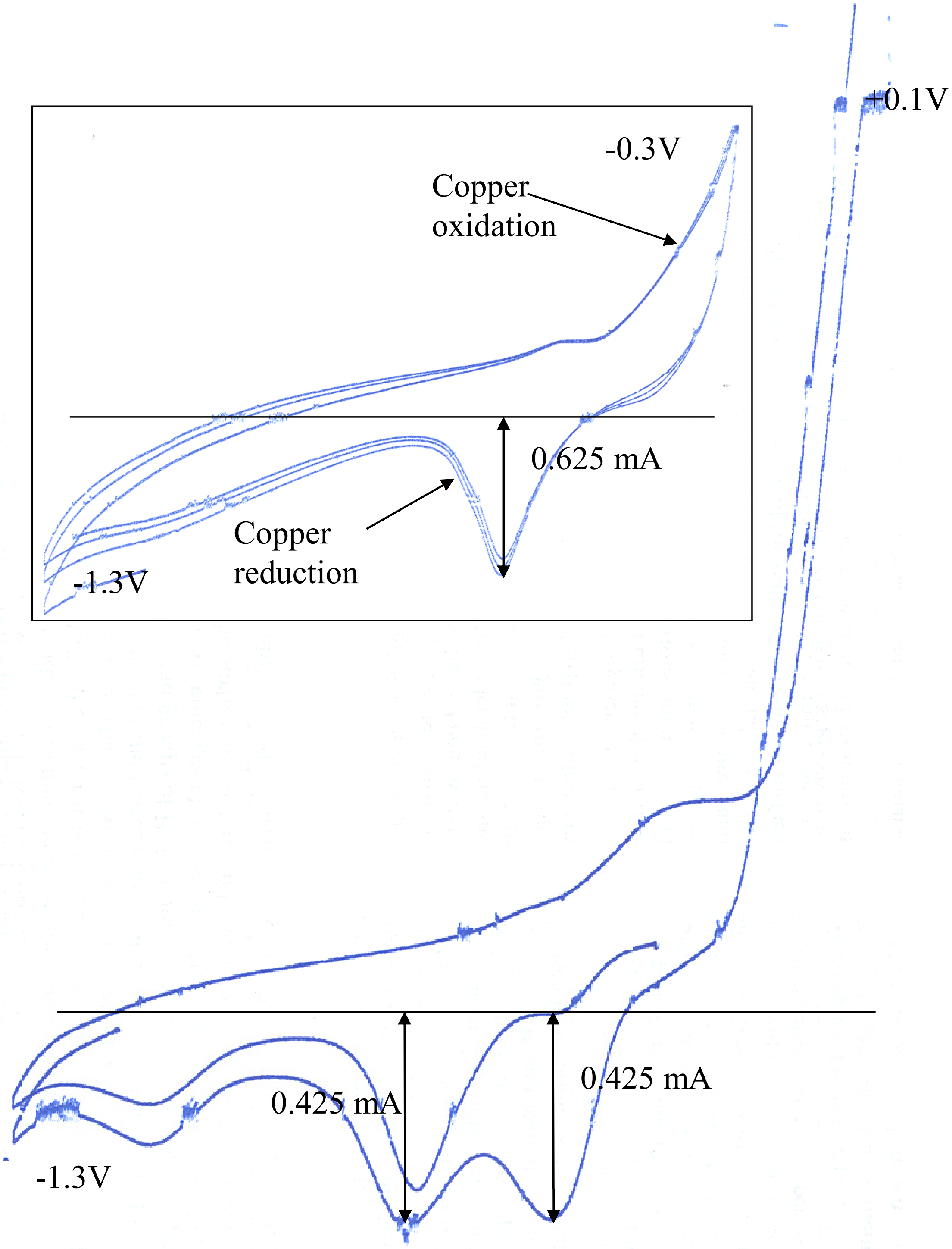

Figure 7.7 - CV of Cu in CH_3CN. CV features are attributed to the oxidation and reduction of different valenced Cu species.

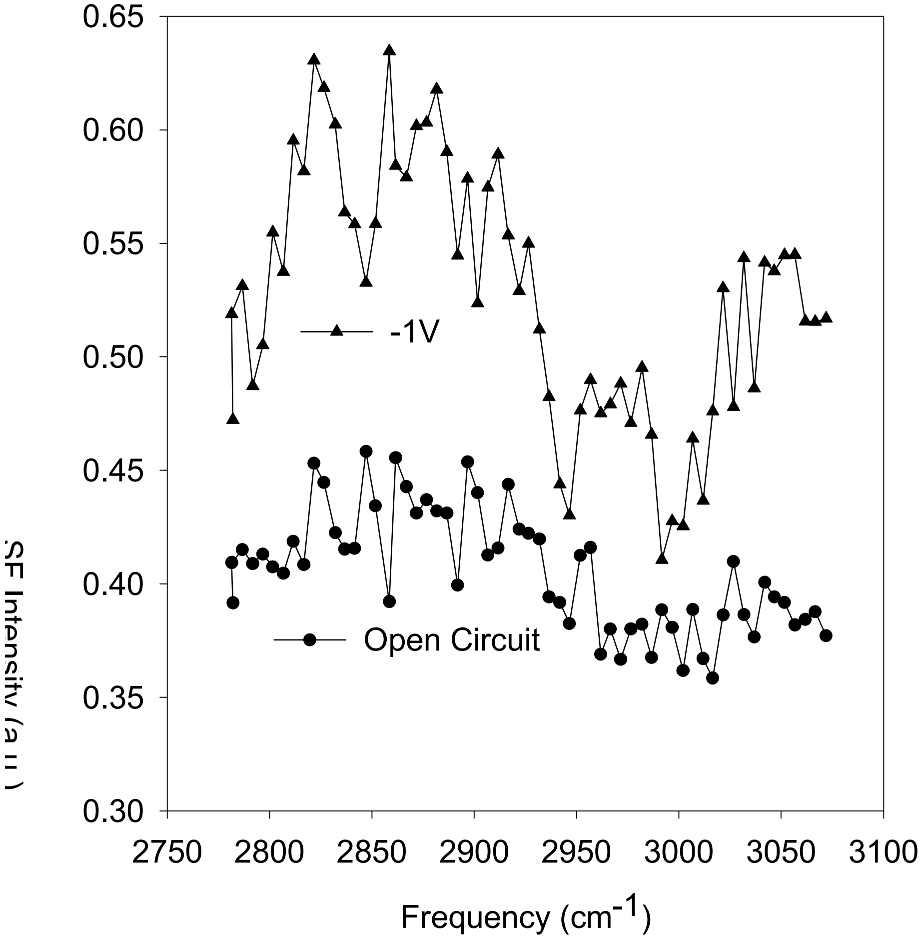

Figure 7.8 - SFG spectra of CH_3CN on Cu at open circuit and at -1V. Spectra displayed on the same scale show a dramatic increase in the non-resonant SFG signal when a potential is applied to the electrode.

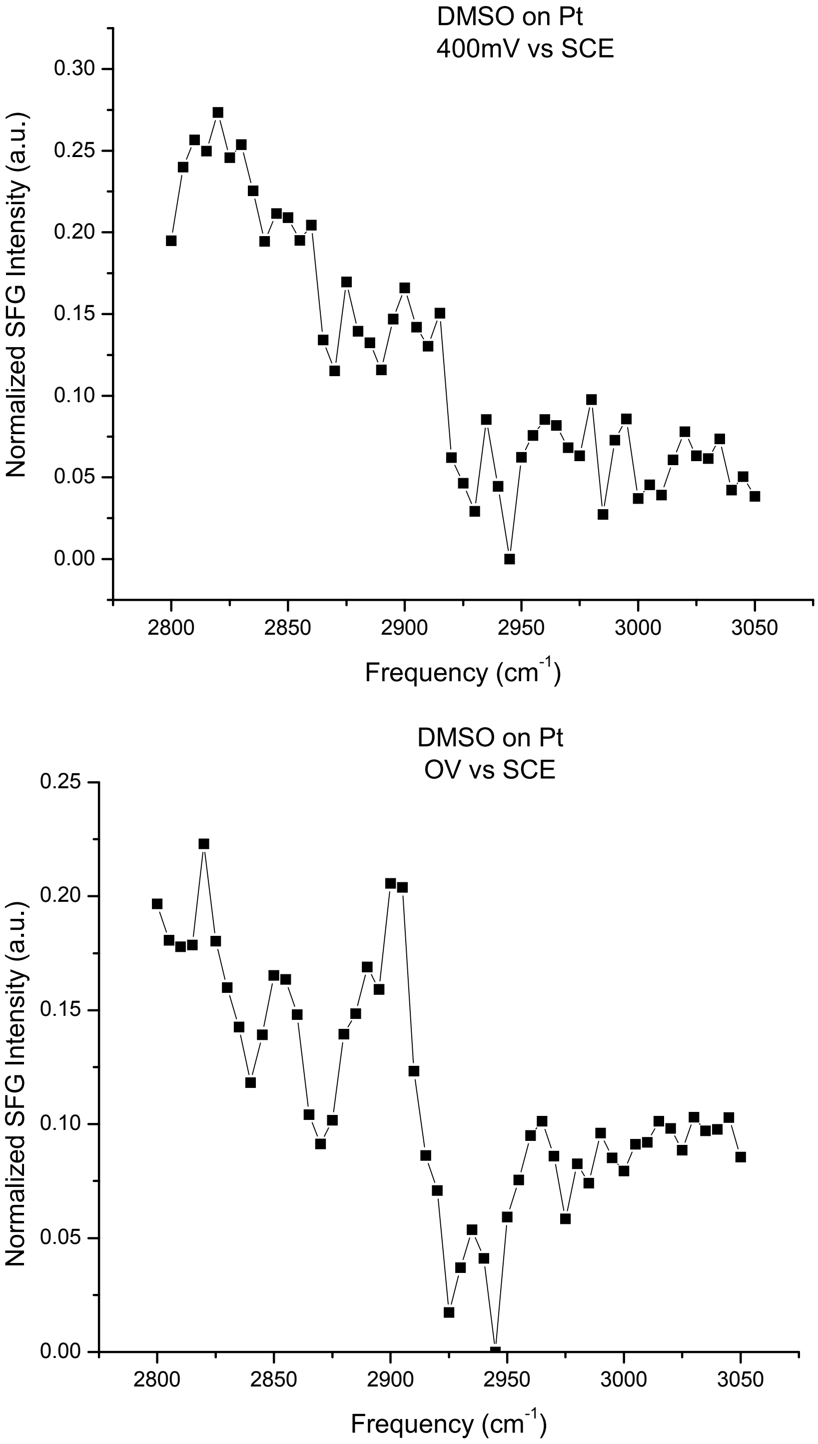

Figure 7.9 - SFG of Pt in DMSO a) at 400mV and b) at 0mV. Peak at 2900cm^{-1} is assigned to the symmetric CH_3 vibrational band of DMSO.